STATIC AND DYNAMIC PROPERTIES OF CN/Cu(001) SURFACES

AND

OXIDATION, DISSOCIATION AND BIMOLECULAR DECARBOXYLATION

OF ISOCYANATE SPECIES ADSORBED ON Cu(001)

by

ERKAN ZIYA CIFTLIKLI

A Dissertation submitted to the

Graduate School-New Brunswick

Rutgers, The State University of New Jersey

in partial fulfillment of the requirements

for the degree of

Doctor of Philosophy

Graduate Program in Chemistry & Chemical Biology

written under the direction of

Professor Jane Hinch

and approved by

‾‾‾‾‾‾‾‾‾‾‾‾‾‾‾‾‾‾‾‾‾‾‾‾

‾‾‾‾‾‾‾‾‾‾‾‾‾‾‾‾‾‾‾‾‾‾‾‾

‾‾‾‾‾‾‾‾‾‾‾‾‾‾‾‾‾‾‾‾‾‾‾‾

‾‾‾‾‾‾‾‾‾‾‾‾‾‾‾‾‾‾‾‾‾‾‾‾

New Brunswick, New Jersey

[October, 2012]

ABSTRACT OF THE DISSERTATION

STATIC AND DYNAMIC PROPERTIES OF CN/Cu(001) SURFACES

AND

OXIDATION, DISSOCIATION AND BIMOLECULAR DECARBOXYLATION

OF ISOCYANATE SPECIES ADSORBED ON Cu(001)

by Erkan Z. Ciftlikli

Dissertation Director:

Professor Jane Hinch

This dissertation presents an outlines my investigations of static and dynamic properties of adsorbed cyanide (CN) and isocyanate (-NCO) species as well as some of their chemistries. Surface bound CN-containing species have not previously been studied extensively, partially due to the inapplicability of fundamental e-beam based surface analysis techniques for investigations. I had the opportunity in my studies to employ multiple surface probing techniques, i.e. HAS, XPS, NEXAFS, TPD and RAIRS, to compile and cross-examine information from CN, –NCO, and derived species, adsorbed on the Cu(001) surface.

While angle resolved He atom scattering (HAS) was employed to identify and investigate the ordered superstructure of CN/Cu(001) surfaces, TOF-HAS was employed to investigate its dynamic properties. The CN/Cu(001) surface induced unprecedented

simultaneous coherent He diffraction with a large "classical" multiphonon backscattered He intensity. A superstructure is implied that contains both rigidly bound CN species, which maintain the long range c(10x6) translational symmetry, together with bound highly-dynamic CN species that exhibit large thermally induced displacements. The NEXAFS measurements suggest multiple spatial binding configurations for the adsorbed CN moieties. In addition, TPD spectra of C_2N_2 desorption from CN/Cu(001) surface were analyzed, using my newly developed method, to determine the activation energies for desorption as a function of CN coverage.

There are two reactions of NCO species examined in my studies. The first is the newly discovered mutual reaction between NCO species. This type of interaction had not been seen before, as it is essentially difficult to prepare pure NCO/metallic surfaces. Copper was chosen as a substrate as HNCO exposures of Cu(001) at RT, followed by spontaneous H_2 desorption, do produce NCO only surfaces. A thermal treatment of the surface, at 573K, leads to a bimolecular decarboxylation of NCO, leaving a carbodimide species (NCN) on the surface. The sp-hybridized linear NCN moieties, which are bound nearly parallel to the substrate, show high thermal stability. The second reaction of NCO, which I have studied, is its oxidation. In particular, the effect of CN coadsorbates on the oxidation of NCO was studied. It was found that the presence of CN catalyzes a dissociation reaction of NCO species on Cu(001).

ACKNOWLEDGMENTS

"*Life is a symphony of successive losses*" says *Asimov* in his novel *Nemesis*. The melody might change from happy to sad, and then return to happy tones. Yet, the harmony remains a constant reminder of the overall nature of the symphony. That must be why, while writing these lines, I feel happy for the successful completion of my Ph.D studies and yet, at the same time, I feel sad for the end of another chapter in my life. Nevertheless, this is not a proper place for philosophical monologs, but a place to express appreciation and gratitude. Thus, let's start: This relatively voluminous dissertation which reports the results of a part of my research activities during the duration of my "a little bit longer than usual" Ph.D studies would not come into existence without the guidance, collaboration, contribution, and support of many people.

Surely, the largest share of credit goes to my supervisor Prof. Jane Hinch who has given me the opportunity to work with her and has thoroughly supported me in all aspects of my studies. This support manifested itself sometimes in the form of articulate comments on the problems I suffer in the lab or in my analysis work, in the form of critical review of my manuscripts, and in the form of financial support. I have repeatedly bothered her with my questions, yet she has never made me feel unwelcome. I don't know whether the verse by Ottoman poet *Baki* "*What remains eternal under this sky is the memories of a kind soul*" is true. What I know is that I will continue to remember my Ph.D. supervisor with gratitude and with a smile on my face as long as I live.

Last but not least, I would like to thank my parents, who brought me into this world, gave me their unconditional love, did their best for me to receive an excellent formal education, and together with my sisters have stood by me in all my wise and unwise deeds in this life. Remembering them is a source of strength and relief to me whenever I find myself in a difficult situation. I have lost my mother recently in November 2011. *Arif Nihat Asya* in his poem on the daughter he lost writes "*Phrasing your name was a kiss on my lips, it still kisses, do you hear?*" I too do not know whether my mother hears

me. But be my family located nearby or beyond the oceans, be my Mom beyond this life or beyond the reach of my voice, I will continue to cherish her and my family as long as I live. Nobody deserves the dedication more than they.

DEDICATION

Canımdan çok sevdiğim babama, anneme ve kızkardeşlerime...

TABLE OF CONTENTS

LIST OF TABLES

LIST OF FIGURES

CHAPTER 1

General Introduction

1.1   Motivation

My initially planned Ph.D. research included investigations of a group of representative CN containing molecules and moieties (e.g. CN, NCO, CH_3CN, Pyridine, $(CH_3)_3CNC$, HCN and cyclopentadiene) adsorbed on a Cu(001) surfaces. While I have addressed all of these systems, barring HCN, in this dissertation I will report primarily on the major results from our investigations of CN/Cu(001) and NCO/Cu(001) samples. I have focused on the single adsorbate samples and their thermally activated reactions as well as of O+CN/Cu(001), NCO+O/Cu(001) and NCO+CN+O/Cu(001) surfaces. CN is a potent ligand and pseudohalogen with a strong affinity for forming ionic compounds or complexes with many transition metals. With this property, cyanides have a number of uses in a large number of industries, especially in mining and electroplating.[1] Similarly, a large number of NCO containing chemicals, especially alky and aryl isocyanates and diisocyanates are produced, globally on the scale of multiple million metric tons annually. NCO containing chemicals are utilized in a broad range of industrial activities including the production of cellular materials, elastomers, and adhesives, as well as in medical applications.[2]

In spite of the sheer importance of these molecules and moieties in industrial chemistry, we find only a relatively small number of published surface studies on these moieties. The simple reason behind this imbalance ought to be related to the inapplicability of

many e-beam-using experimental techniques (e.g. LEED, AES, etc.). I shall show explicitly that a LEED e-beam damages the long range ordering of CN adsorbed on Cu(001). More generally this is believed to be true also for many CN-containing adsorbates on single crystal metal surfaces, especially on low corrugation fcc (001) and fcc (111) surfaces. Therefore, one of our aims was to employ Helium Atom Scattering (HAS) in conjunction with other applicable surface probing techniques to study static and dynamic properties of these CN-containing adsorbed species. For example, angle resolved HAS [3], employing nearly monochromatic thermal helium atoms, which has no destructive effect on CN covered surfaces, will be used to detect ordered super structures of the surfaces where low energy electron diffraction (LEED) fails to do so. Or, energy resolved inelastic HAS [4-6] can be used to probe low energy vibrations like frustrated translational and frustrated rotational modes instead of electron energy loss spectroscopy (EELS).

We have two main goals in our studies on adsorbed CN moieties. The first goal is to understand the static and dynamic properties of CN species adsorbed on copper. CN^- is isoelectronic with CO. CO, which is arguably the most studied adsorbate molecule in the history of surface science, is bound to surfaces perpendicularly as a result of the geometrical impositions of the covalent bonding based on σ donation and π back donation interactions. On the other hand, bonding interactions between CN^-, or properly speaking, $CN^{\delta-}$, and metal substrates is predominantly ionic.[7] The forthcoming information, such as (i) the dimensions of an ordered super structure, (ii) the CN number density at saturation, (iii) the CN binding geometries, especially angles of inclination

with respect to the surface normal, and (iv) the apparent CN binding energies, can be not only utilized in comparative studies but also to supply highly valuable reference information for computational investigations of these surfaces. [8, 9]

Our second main goal with cyanides is to shed light on the role(s) played by CN on catalyst surfaces, especially during the reduction reactions of nitrogen oxides, NO_x. Indeed, there are a number of studies [10-17] reporting $CN_{(a)}$ species which manifests themselves with weak features in transmission IR spectra. Investigators have tended, perhaps erroneously, to ascribe the presence of CN to minor side reactions and to frame it as a minor byproduct. First of all, a relatively weak signature of CN species in an IR spectrum by no means should be associated with small CN quantities. It is known that $v(CN)$ intensities are inherently weak, e.g. for the gas phase [18, 19] or in a surface bound [20] HCN molecule. In the later case, the $v(HC)$ intensity in an IR spectrum appears to be almost three orders of magnitude stronger than the intensity of a $v(CN)$ mode. Secondly, during the catalytic reduction of NO_x, the complex nature of a real catalyst surface in conjunction with the many concurrent reactions happening thereon dramatically hinders any reliable ascription of the role(s) of CN, if any.

The latter problem for investigations of cyanide (CN) also holds true for the elucidation of the exact nature of isocyanate (NCO) species observed on real catalyst surfaces. NCO is widely recognized as a key reaction intermediate for the catalytic process of NO_x reduction. In addition, another serious obstacle is found in the limited number of experimental techniques available to study metals deposited on high-surface-area

powder-form support materials. Vibrational spectroscopies remain the principal investigation techniques. Established surface techniques offering powerful tools for quantization, like XPS, AES and TPD, either give indirect information or are largely useless for investigation of real catalysts.

These complications collectively often enforce the use of simpler planar surfaces when possible to enable a better atomic level understanding of reaction mechanisms. The successful application of this concept has, on many occasions, given in-depth understandings of complex reaction. [21, 22] In our research, our particular goals are to generate model NCO/Cu(001), NCO+O/Cu(001) and NCO+CN+O/Cu(001) surfaces and later to investigate thermally induced reactions of these surfaces. Studies of the thermal stability of a pure NCO/Cu(001) surface also enable the study of possible NCO-NCO reactive interactions without the interference of any coadsorbates. A comparative investigation of the thermal treatments of NCO+O/Cu(001) and NCO+CN+O/Cu(001) surfaces will reveal the predominant influence of CN species on the oxidation reaction of adsorbed NCO.

1.2. Overview

In chapter 2, both theoretical and operational principles of all experimental techniques employed in our investigations will be briefly outlined. Later in the chapter, the experimental setup located in WR-187 and its operational details will be described.

In Chapter 3, we will prepare a saturated pure CN/Cu(001) at 263 K and determine its coverage by comparing the intensity of its N 1s photoemission peak with an N 1s peak intensity from a 0.5ML saturated N/Cu(001) face. Angle resolved HAS will be employed to determine the identity of the ordered super structure. Later Near Edge X-ray Absorption Fine Structure (NEXAFS) spectroscopy will be used to discriminate CN moieties based on their spatial orientation as well as to characterize the spatial orientations of each CN type. Apart from obtaining the structural information, we will also employ TOF-HAS measurements to investigate the dynamic character of CN species adsorbed on Cu(001).

In Chapter 4, recombinative desorption of CN species adsorbed on Cu(001) evolving molecular cyanogen (C_2N_2) will be studied by using temperature programmed desorption (TPD) measurements. Since the adsorbed $CN^{\delta-}$ species are charged, mutually repulsive dipolar interactions lead to a marked desorption energy reduction with increasing CN coverages. Established methods in the literature for analysis of TPD, which enforce a constant E_d value for all coverages for a given desorption system fail to model desorption spectra of the CN/Cu(001) surfaces. Other analysis techniques, which were designed to deal with the desorption spectra of surfaces with coverage dependent E_d cannot be implemented successfully to model our desorption spectra since our data does not exhibit adequate signal-to-noise ratios. In this chapter we will therefore be reporting on two new analysis approaches that we have developed to determine the functional form of a coverage dependent component of E_d. These approaches are more robust in that they are able to utilize comparatively poor signal to noise data sets such used here. The first approach involves an analysis of the variations of desorption peak asymmetry with initial

CN coverages. The second quantitative approach utilizes only temperatures and intensities of TPD peaks, together with deduced surface coverages at the peak maxima, to determine the derivative of the functional form of the CN coverage dependence of E_d.

In Chapter 5, an impurity free NCO/Cu(001) surface is prepared by the dissociative adsorption of HNCO at room temperature followed by H_2 desorption. Coverage calibrations of NCO/Cu(001) surfaces will be performed by comparing N 1s and O 1s photoemission peak intensities to the N 1s peak intensity from a 0.5ML saturated N/Cu(001) and the O 1s peak intensity from a 0.5 ML saturated O/Cu(001) surface. This impurity free NCO/Cu(001) surface then will be annealed to observe thermally induced reactions of NCO species. A quantitative analysis of the change observed between pre and post annealed XPS spectra will be used to deduce the empirical stoichiometry of a bound post-anneal product as well as the identity of desorbed gas molecules. Finally, FT-RAIR spectra of this post-annealed surface will be employed to shed more light onto the identity of the product.

In Chapter 6, the effect of CN species on thermally induced reactions of NCO co-adsorbed with O will be reviewed. Along this aim, we will first prepare a NCO+O/Cu(001) surface by HNCO exposures on Cu(001) at room temperature followed by O_2 exposure of submonolayer NCO/Cu(001). Secondly, we will prepare a CN+NCO+O/Cu(001) surface by exposure of Cu(001) to cyanogen (C_2N_2) and O_2. These two surfaces will be annealed at 473K and thermally induced reactions from these two surfaces will again be identified by employing careful stoichiometric analysis of the

change between pre- and post- annealed surface probed by XPS. Finally, TPRD will be used to indentify the two gaseous products from these two surfaces.

In Appendix A, we will review the mathematical formulations for the processing and normalization of NEXAFS data. This is primarily in order to determine the spatial orientation of surface moieties.

In Appendix B, the effects of coverage dependent activation energies of desorption on the form of "Arrhenius" curves will be mathematically modeled. A simulated curve will be compared to an Arrhenius curve obtained from an individual desorption spectrum.

In Appendix C, a review will be given of the experimental setup used for isocyanic acid (HNCO) synthesis, via thermal decomposition of cyanuric acid, as well as for HNCO purification.

1.3.   References

[1]   L. Guzman, M. Segarra, J.M. Chimenos, P.L. Cabot, and F. Espiell, Electrochimica Acta 44 (1999) 2625.
[2]   H. Ulrich, Chemistry and Technology of Isocyanates, John Wiley & Sons Ltd., West Sussex, 1996.
[3]   D. Farias and K. H. Rieder, Reports on Progress in Physics 61 (1998) 1575.
[4]   R. B. Doak, ed., Single Phonon Ineleastic Helium Scattering, Atomic and Molecular Beam Methods, Vol. Volume 2, Oxford University Press, Inc., New York, 1992.
[5]   B. Gumhalter, Physics Reports 351 (2001) 1.
[6]   F. Hofmann and J. P. Toennies, Chemical Reviews 96 (1996) 1307.
[7]   J. C. W. Bauschlicher, Surface Science 154 (1985) 70.

[8]   F. Ample, D. Curulla, F. Fuster, A. Clotet, and J. M. Ricart, Surface Science 497 (2002) 139.

[9]   M. J. Harrison, D. P. Woodruff, and J. Robinson, Surface Science 600 (2006) 340.

[10]   N. Bion, J. Saussey, M. Haneda, and M. Daturi, Journal of Catalysis 217 (2003) 47.

[11]   X. Chen, X. Yang, A. Zhu, C. T. Au, and C. Shi, Journal of Molecular Catalysis A: Chemical 312 (2009) 31.

[12]   F. Lónyi, J. Valyon, L. Gutierrez, M. A. Ulla, and E. A. Lombardo, Applied Catalysis B: Environmental 73 (2007) 1.

[13]   V. Matsouka, M. Konsolakis, R. M. Lambert, and I. V. Yentekakis, Applied Catalysis B: Environmental 84 (2008) 715.

[14]   F. Poignant, J. L. Freysz, M. Daturi, and J. Saussey, Catalysis Today 70 (2001) 197.

[15]   A. Shichi, T. Hattori, and A. Satsuma, Applied Catalysis B: Environmental 77 (2007) 92.

[16]   S. Tamm, H. H. Ingelsten, and A. E. C. Palmqvist, Journal of Catalysis 255 (2008) 304.

[17]   T. Venkov, M. Dimitrov, and K. Hadjiivanov, Journal of Molecular Catalysis A: Chemical 243 (2006) 8.

[18]   H. B. Friedrich and P. F. Krause, The Journal of Chemical Physics 59 (1973) 4942.

[19]   K. Kim and W. T. King, The Journal of Chemical Physics 71 (1979) 1967.

[20]   H. Celio and M. Trenary, Physical Review Letters 84 (2000) 4902.

[21]   D. W. Goodman, Journal of Catalysis 216 (2003) 213.

[22]   P. L. J. Gunter, J. W. Niemantsverdriet, F. H. Ribeiro, and G. A. Somorjai, Catalysis Reviews: Science and Engineering 39 (1997) 77

CHAPTER 2

Experimental Methods

2.1.   The Theory of Experimental Methods:

2.1.1   Helium Atom Scattering (HAS)

The helium atom scattering (HAS) technique is a powerful surface investigation tool to probe surface phonons [1-6] and low energy adsorbate vibrations[7-13], to generate diffraction patterns from ordered surfaces [6, 14-17] as well as to monitor the kinetics of coverage dependent adsorption events through uptake curves.[18, 19] These technique applications were made possible with the development of supersonic expansion jet nozzles, which produce highly monochromatic helium atom beams with a velocity distribution as low as $\Delta V/V \approx 1\%$.[20] The translational energy of the thermal helium atoms ranges from a few meVs to ~100 meV. The helium atoms interact weakly and are back scattered from the repulsive potential arising from electron overlap with the uppermost surface atoms only.. Therefore HAS manifests itself with a unique and unparalleled property of absolute surface sensitivity without inducing any detrimental effects on the surface under investigation.

When a helium beam illuminates a surface, while some of the helium atoms are scattered elastically (ΔE=0), the rest of the helium atoms are scattered inelastically (ΔE $\neq$ 0) Inelastically scattered a helium atoms can be classified into two groups depending on

whether they interact with a single phonon (or a single vibrational mode of an adorbate) or multiple phonons. While single phonon processes show themselves as discrete peaks in energy-resolved HAS spectra, multiphonon processes yield a broad background-like feature which can extend across a wide spectral range. The relative proportions of the elastically scattered helium atoms, inelastically scattered helium atoms with single phonon processes and inelastically scattered helium atoms with multiphonon processes can be estimated by the determination of the Debye-Waller factor, 2W. If 2W < 1 for a scattering event, it suggests the majority of the helium atoms are scattered elastically. A minority, in the fully quantum mechanical regime, are scattered from single substrate phonons and/or from adsorbate single vibrational modes. On the other hand, if 2W>6, then the vast majority of the helium atoms scattered from the surface involve multiphonon-type inelastic interactions.

The Debye-Waller factor formalizes how the intensity of elastically scattered helium atoms at a given momentum transfer vector is attenuated as a function of surface temperature and/or beam energy.

$$I = I_0 \cdot e^{-2W} \quad \text{where } 2W = \frac{3 \cdot \hbar^2 \cdot \left(\overrightarrow{\Delta k_z}\right)^2 \cdot T_x}{M_s \cdot k_b \cdot \Theta_D^2} \tag{2.1}$$

$\overrightarrow{\Delta k_z}$ is the momentum change perpendicular to the surface plane experienced by the scattered helium atoms, T_x is the sample temperature, M_s is the mass of the surface moiety from which helium atoms scatter, k_b is the Boltzmann constant and Θ_D is the surface Debye temperature. If the measurements are being carried out at a specular direction, (2.1) is reduced to:

$$2W = \frac{24 \cdot m \cdot (E_i \cdot \cos^2 \theta_i + D) \cdot T_x}{M_s \cdot k_b \cdot \Theta_D^2} \tag{2.2}$$

where E_i is the energy of the monochromatic incident helium atoms, m is the mass of the helium atom, θ_i is the angle between the direction of the incident helium beam and the surface normal, and D is the depth of the potential energy as a result of attractive interactions between helium atoms and the surface. Inclusion of the of the parameter D in (2.2) is known as the "Beeby" correction [21], registering the acceleration of thermal helium atoms in front of the surface as a result of the attractive potential. Taking D into consideration does not change the value of the Debye-Waller factor 2W, but it does affect the value deduced for the surface Debye temperature, Θ_D.

In this dissertation, three fundamental types of HAS measurements will presented in various occasions. These are: (i) Uptake measurements, (ii) Angle resolved HAS measurements and (iii) Time of flight (TOF) measurements.

(i) In the uptake measurements, the sample is brought to the specular position, at which $\theta_i = \theta_f$, and the helium reflectivity from the surface is monitored in the course of an adsorption process. This measurement is a valuable tool as shifts observed in the shape of the decay curve of helium reflectivity are associated with the onset of differing absorption regimes, depending on the adsorbate coverage level and possibly on the adsorption rates. The sensitivity of the measurement is superb at low coverage levels, i.e. the total helium reflectivity can be attenuated by as much as 50% at $\theta \sim 0.02$ ML, with scattering cross sections of individual adsorbed molecule of order ~ 100 Å^2. Several

aspects of utilization of the uptake curves were meticulously detailed by Poelsema and Comsa.[19]

(ii) Angular Resolved HAS is another powerful application of the technique.[22, 23] As the De Broglie wavelength of thermal energy helium atoms are of the order of ~1 Å, they are good candidates for wide–angle surface diffraction studies. As incident helium atoms are, in fact, reflected at ~3 Å above the core of the topmost layer atoms of a densely packed surface, the technique has an extreme surface sensitivity. We use two degrees of angular freedom, i.e. polar and tilt angles, to scan 2-D sections of reciprocal space. A sharp energy resolution of the incident beam is required for strong, and well-resolved, peaks in a diffraction pattern. Incremental reciprocal space steps are taken during scanning at a rate ~0.01-0.02 Å^{-1}/sec. For a HAS instruments with a fixed total scattering angle ($\theta_{total} = \theta_i + \theta_f$), the parallel momentum change experienced by elastically scattered helium atoms detected at the mass analyzer, ΔK, is derived from the polar angle positions of the crystal;

$$\Delta K = \frac{\sqrt{2mE_i}}{\hbar}\left(\sin\left(\theta_{total} - \theta_i\right) - \sin\theta_i\right) \tag{2.3}$$

where m and E_i are the mass and energy of the incident helium atoms, respectively. θ_i is the angle between the direction of incident helium beam and the surface normal, $\left(\theta_{total} - \theta_i\right)$ or θ_f is the angle between surface normal and direction of the helium atoms targeted towards the detector.

(iii) The ability to probe surface phonons as well as to measure frustrated translational (T) and frustrated rotational (R) vibrations of an adsorbate is another powerful application of HAS. Unlike many other adsorbate related vibrations, the T and R modes are can be polarized parallel to the surface plane. Thus, measurement of these modes can reveal key information about the lateral variation of the adsorbate potential energy surface. The excitation of T modes is often considered as a first step of towards the lateral hopping of an adsorbed molecule, contributing to surface diffusion of the adsorbate. In addition to these factors, T (and R) modes can contribute >99% of the total entropy of an adsorbate system.[12] Therefore, characteristics of the T and R vibrational modes might often elucidate processes that are governed by entropy-driven mechanisms on a surface. For this type of measurements, generally called time of flight (TOF)-HAS, a rotating disc with four narrow slit(s) is placed between the helium source and sample to chop the beam to give temporally sharp helium pulses. For example, the chopper disc rotating at a 400 Hz slit frequency, produces 400 helium pulses a second, each separated from the next by 2500 μsec. Typically, the helium detector is set to measure for synchronized 2ms periods with a time resolution set by 2 μsec long channels.

The data recorded at the end of the experiments are composed of I vs t_{cd} data points, where t_{cd} is the time passed between chopping of a helium pulse and the detection of the signal which is equal to sum of the time of flight between chopper to target (sample), t_{ct}, and the time of flight between target to detector, t_{td}. Once t_{cd}^{e}, time of flight for the elastically scattered helium atoms is determined, it can be used convert all t_{cd} values in the raw data to t_{td} values since the distances between chopper to target and target to

detector are known. Subsequently, t_{td} values can be used to determine ΔE and ΔK

equivalents of the each t_{cd} value in the raw data file by using

$$\Delta E = E_i \left[\left(\frac{t_{td}^e}{t_{td}} \right)^2 - 1 \right] \tag{2.4}$$

$$\Delta K = \frac{\sqrt{2mE_i}}{\hbar} \left[\frac{t_{td}^e \sin\left(\theta_{total} - \theta_i\right)}{t_{td}} - \sin\theta_i \right] \tag{2.5}$$

Combining (2.4) and (2.5) leads to

$$\frac{\Delta E}{E_i} = \left(\frac{\sin\theta_i + \dfrac{\Delta K}{\sqrt{2mE_i}}\hbar}{\sin(\theta_{total} - \theta_i)} \right)^2 - 1 \tag{2.6}$$

Equation (2.6) relates all possible ΔE and ΔK values for a given combination of θ_i and

E_i, and it is called a "scan curve equation".

At this point it is must be recalled that as the "time of flight" to "energy exchange"

conversion leads to a data set with variable data point separation, the conversion into the

energy domain is <u>not</u> complete until we normalize the intensities.

$$I(E) = \frac{m}{4} \left(\frac{t_{td}^3}{x_{td}^2} \right) I(t) \tag{2.7}$$

In that way we maintain a constant integral intensity; i.e. $\int I(E)dE = \int I(t)dt$.

2.1.2. X-Ray Photoelectron Spectroscopy (XPS):

X-ray photoelectron spectroscopy (XPS) (or Electron spectroscopy for Chemical analysis, ESCA) is a surface sensitive technique, which involves employing X-Ray photons to illuminate a surface and subsequently detecting the intensity of the electrons ejected from the sample as function of their kinetic energies. [24] Photoelectric event is a photon in - electron out process, i.e. Einstein's photoelectric equation formalizes how the energy of the incident photon is transferred to the core electron to be ejected into vacuum, i.e.

$$E_k = h\nu - E_b - \phi_S \tag{2.8}$$

where, E_k is the kinetic energy if the electron ejected from the sample into vacuum, $h\nu$ is the energy of the incident photon, E_b is the binding energy of the electron ejected from the sample. ϕ_S, is the sample work function. These photo electrons are yet to be detected by a analyzer, whose work function, ϕ_A, is smaller than ϕ_S. If the sample and the detector are grounded, which equalizes their Fermi levels, then the kinetic energies of the electrons upon arrival at the detector have increased by $(\phi_S - \phi_A)$;

$$E_k = h\nu - E_b - \phi_S + (\phi_S - \phi_A) = h\nu - E_b - \phi_A \tag{2.9}$$

where ϕ_A is hopefully a constant that is unaffected by the sample history.

The most convenient way of X-ray generation is by using X-Ray tubes, in which electrons emitted from a filament are accelerated to ~15 keV before colliding at an anode. Once the collision occurs, a core electron from the anode atom is ejected and

subsequently a photon is created through the collapse of an electron from outer orbits to the vacancy created. This process generates multiple X-ray lines with discrete energies as well as an energy continuum of photons called Bremssthrahlung Radiation. The output radiation from the X-ray tube, thus, must be treated with a monochromator to remove all Bremssthrahlung radiation as well all X-ray lines except the one intended for studies. The intensity, energy, and the energy width of an X-ray line generated from the tube are all prime concerns when it comes to choosing an anode material. Aluminum and magnesium appears to be the "optimum" choices for anode materials, i.e Al K_α and Mg K_α X-Ray emissions with energies at 1486.6 eV and 1253.6 eV, respectively, [24] are two X-ray sources used in almost all XPS systems around the globe.

Using X-Ray beams generated by synchrotron light sources for the XPS has two main advantages over the use of X-Ray tubes: Firstly, although the X-Ray beam supplied by a synchrotron light source to a beamline is polychromatic to an extent (e.g 240-770 eV for U12A beamline in NSLS,) it is required to pass through a monochromator before it's utilization. The monochromitized beam, illuminating the sample surface, is still considerably brighter than the beam generated by any X-Ray tubes. This leads to a considerable reduction of the time-cost of each measurement and makes possible the realization of fair signal-to-noise ratios in minutes even for the probing of surface atoms in the submonolayer regime. Secondly, the polychromatic beam supplied to a beamline means we have the power of tuning the beam energy. As the photoelectric cross sections vary with incident photon energy, $h\nu$ tunability often provides an extra edge to further shorten data acquisition times.

Surface incident photons illuminate a great deal of depth into the sample, up to a micron below the top-most layer of the surface, and eject electrons from core levels. However, these ejected electrons should penetrate through the solid sample material before reaching the vacuum and then the detector. The intensity of the ejected core electrons reaching the detector without a kinetic energy lost is thus attenuated exponentially with distance between the atom where electron is ejected and the surface of the sample, i.e.

$$ I/I_0 = \exp\left(-d/\lambda(E_k) \right) \tag{2.10} $$

Where I/I_0 is the fraction of ejected electrons emitted towards the XPS detector reaching their destination without any energy lost, d is a distance between the atom where an electron is ejected and the position at the surface of the sample where the electron is emitted. $\lambda(E_k)$ is the inelastic mean free path of the electrons in the substrate, as a function their final kinetic energies. The λ variation, as a function of E_k, for different materials resemble each other to such an extent that the superimposed curve of λ vs E_k for different materials is called the "universal curve". This curve implies that λ is ~5-30 Å for typical X-ray beam energies used. This, in other words, means that 95% of the electrons ejected from an atom at a depth of $d = 3\lambda$, interacts with atoms on its path before leaving the sample, creating secondary electrons. The closer the electron ejecting atom is to the surface, the higher the probability of detecting those electrons before energy loss. Thus the technique, which analyzes only the electrons with as emitted energies, exhibits a surface sensitivity of 5-30 Å.

Detection of the photoelectrons in XPS systems is generally done by Concentric Hemispherical Analyzers (CHA). A CHA [25] consists of two stainless steel hemispheres with different radii (R_1(outer hemisphere) and R_2(inner hemisphere)), placed concentrically on a support which electrically isolates them from each other. A CHA will possess two slits located at $R_{av} = (R_1+R_2)/2$, one for the entrance of the photoelectrons coming from the sample, another at a point of leaving for counting. Negative biases, with different magnitudes, are applied to these two hemispheres, V_1 and V_2 ($V_1>V_2$), and only the electrons with a specific kinetic energy , E'_k, entering to the hemispherical analyzer will be able to leave the analyzer through the exit slit to be counted, i.e.

$$E'_k = \left[\left(V_1 R_1 + V_2 R_2 \right) \Big/ 2R_{av} \right] e \qquad (2.11)$$

Thus, in principle by varying V_1 and V_2 (R_1, R_2 and R_{av} are all fixed for a given detector), one can separate electrons based on their kinetic energies. However, one doesn't as the absolute energy resolution in a CHA, ΔE, is linearly proportional to the kinetic energy of the electrons detected, i.e.

$$\Delta E \propto \frac{E'_k w}{R_{av}} \qquad (2.12)$$

where w is the average with of the entrance and exit slits.[26] Optimally the energy resolution for each feature should be identical. A better and near constant energy resolution throughout the spectral range is achieved instead by electron retardation (of E_{ret}) through a cascade of electrostatic lenses before entrance to the hemispherical capacitor. The instrument is then run at a constant and preset V_1 and V_2 values, which allow only the electrons with certain (low) kinetic energy (pass energy, PE) to reach the exit slit, i.e.

$$E_k = E_{ret} + \text{PE} \qquad\qquad (2.13)$$

Thus, at a constant PE regime, by scanning the extent of electron retardation, we can scan all E_k values during the data acquisition. This mode of data acquisition is named as the "Fixed Analyzer Transmission Mode" (FAT Mode). It is worth mentioning that there is a the trade-off between resolution and intensity parameters, i.e. the smaller slit sizes and lower PE values are preferred when better resolution of the peaks are demanded, but this is at the expense of increased data acquisition times. Typical PE values are 50-200 eV for survey scans, 10-20 eV for the detailed scans.

Binding energies of the core level electrons are slightly affected by the local environment (bond making, ionization, etc.) experienced by the valence electrons of the atom because a change in the valence electron density of an atom slightly changes the effective nuclear charge felt by the core electrons; the extent of nuclear shielding is slightly modified. This effect, although being minute compared to average binding energies of the core electrons, is still well above the resolution limits of the XPS. Thus, we have the ability to distinguish the same atoms with different chemical environments. This makes XPS a valuable surface probe technique.

In addition, XPS manifest itself as a powerful quantitative technique as peak intensities observed in spectra can be easily converted to the absolute coverages with the help of beam flux monitoring and using standard samples with known surface concentrations. However, in order to achieve this quantification, one first must remove the background signal from each XPS peak. In raw XPS data, the peaks appear on a continuously

increasing background from higher to lower kinetic energies which increases in an approximately stepwise fashion. The location of the sharpest sloped step "edges" coincides with the location of XPS intensity peaks. This background, beneath the XPS peaks, is called the Shirley background [27], and arises from inelastic electron loses. Once the background is subtracted from the data, the true intensity associated with the photoelectric event happening on a surface is accessible. An XPS intensity, I, within a monolayer or submonolayer regime, follows:

$$I \propto F \cdot \theta \cdot \sigma \cdot A \cdot T \tag{2.14}$$

where F is the flux of the X-Ray beam (as monitored by a fine gold mesh placed between the monochromatized beam and the sample), θ is the surface concentration of the atoms producing photoelectrons, σ is the photoelectron cross section, i.e. probability of X-ray absorption by the atom, A is the X-ray illuminated area of the surface, and T is the conglomeration of all instrumental transmission factors involving pass energy, slit sizes for the analyzer, and properties of the electrostatic lenses before the hemispherical lenses, etc.

Explicitly speaking, four measurements are required for the coverage calibration in four time spans, e.g. t_1, t_2, t_3, t_4. The first and the second measurements are successive, probing the XPS line intensities originating from one of the atoms from the adsorbate layer of <u>unknown</u> coverage, I_x, and of the atoms from the substrate underneath the adsorbed layer, $I_{substrate}$, respectively, each measured with identical sample placement. The pair of third and the fourth measurements, if need be, can be made with another identical sample placement. They are associated with XPS line intensities originating

from the atoms from the adsorbate layer of at a <u>known</u> coverage, $I_x^{standard}$, and of the

atoms from the substrate under the same known adsorbate layer. Recall also that the flux

intensities during these four measurements ($F(t_1)$, $F(t_2)$, $F(t_3)$, $F(t_4)$) are monitored

concurrently during the data acquisition. When we combine the results of these four

measurements;

$$\frac{\left(\dfrac{I_x}{I_{substrate}}\right)}{\left(\dfrac{I_z^{standard}}{I_{subtrate}^{standard}}\right)} = \frac{\dfrac{F(t_1)\cdot\theta\cdot\sigma(E_x)\cdot A_I \cdot T_I}{F(t_2)\cdot\theta_{bulk}\cdot\sigma(E_{substrate})\cdot A_I \cdot T_I}}{\dfrac{F(t_3)\cdot\theta\cdot\sigma(E_x)\cdot A_{II} \cdot T_{II}}{F(t_4)\cdot\theta_{bulk}\cdot\sigma(E_{substrate})\cdot A_{II} \cdot T_{II}}} \qquad (2.15)$$

A and T parameters are identical for in-situ measurements, i.e. A_I and T_I for the first and

second measurements, A_{II} and T_{II} for the third and fourth measurements. σ is identical

for the first and the third, $\sigma(E_x)$, and for the second and fourth, $\sigma(E_{substate})$,

measurements. Thus by simplifying (2.15), we obtain;

$$\theta = \left(\frac{I_x}{I_{subst}}\frac{I_{subst}^{stdrd}}{I_x^{stdrd}}\right)\left(\frac{F(t_3)}{F(t_4)}\frac{F(t_2)}{F(t_1)}\right)\theta_{stdrd} \qquad (2.16)$$

which is the formulation of converting XPS line intensities into the absolute coverage

values.

2.1.3. Near Edge X-Ray Absorption Fine Structure (*NEXAFS*)

NEXAFS is one of the X-ray absorption techniques based on monitoring the excitation of

core level electrons of an atom into unoccupied antibonding molecular orbitals. This

excitation occurs only when the energy of the photons employed in the beam

approximates to the energy difference between core level electron and unoccupied

orbitals. Therefore, unlike in XPS, a portable X-Ray tube cannot be used as a source in NEXAFS. A synchrotron light source, where we have some control over the beam energy, must be used.

Occurrence of this excitation, leaving an empty core level orbital might trigger a number of relaxation processes, including an Auger process, i.e. an electron collapse to the vacant orbital coupled with the kick of another electron from the outer shells. In other words, monitoring the total electron emission, which is proportional to the number X-ray absorption events occurring as a function of incident X-Ray beam energy, would be enough to construct a NEXAFS spectrum. This mode of data acquisition is named the total energy yield (TEY) mode.

However, as in the case with XPS, the incident photons do not interact only with the adsorbate layer, but also a substantial depth of the substrate, generating a large number of secondary electrons through various processes. In addition, for the grounded samples the binding energy of "core" level electrons can be lower than the energy required for the intended X-ray absorption of study; i.e. other core level electrons can be ejected from the sample with relatively small kinetic energies. All these electron generating processes will form a featureless intense background signal in the spectral proximity of the relatively small X-Ray absorption peak. As a result, the inherent statistical noise due to the intense background, which must be subtracted from the total spectrum, suppresses the quality of the signal associated with X-Ray absorption. Therefore, a negatively-biased, highly-transparent, retarding grid is placed in front of the detector, as a high pass energy filter.

This mode of detection is called the partial energy yield (PEY) mode and is employed in most of the NEXAFS detection systems. As the variation of the Auger electron intensity, as a function of incident photon energy, is the best representation of the actual X-Ray absorption spectroscopy, the magnitude of the cut-off energies determined by the biased grid is chosen to be at levels somewhat below the kinetic energy of those Auger electrons. E.g. typically 180-230 eV for the carbon, 290-340 eV for the nitrogen, 430-480 eV for oxygen. [28]

Just as in inverse photoemission spectroscopy, NEXAFS results can be utilized to determine the energy levels of unoccupied molecular orbitals of adsorbed moieties. As the antibonding orbital energies are considerably more sensitive to the bonding site and the spatial geometry of adsorbed molecules than the binding energies of the core electrons, NEXAFS holds an edge over XPS in differentiating the same adsorbate molecules on different adsorption sites and/or spatial orientations.

However, the real power of NEXAFS lies at its use in determining the spatial orientation of the adsorbates on the surface. A synchrotron beam must be used to excite core electrons to unoccupied antibonding orbitals and the synchrotron-produced beam is highly polarized, i.e. the direction of the electric field component of the light is fixed in the plane of the ring. Adsorbate molecules on the surface too have a fixed (yet unknown) spatial position with respect to the substrate surface. Therefore, by simply varying the polar angle of the sample manipulator, we can probe the intensity variation of X-ray absorption spectral feature(s) as a function of an angular relationship between the E-field

vector of the incident X-ray beam and a nodal-vector of an antibonding orbital into which the excited core electrons are promoted.

Theoretical model for relating NEXAFS peak intensities and spatial orientation of the antibonding orbitals is extensively covered elsewhere. [28] Spatial orientation of an orbital is defined by the direction of maximum orbital amplitude and it can be vector (e.g. for a π^* orbital of a diatomic moiety with a double bond, or for a σ^* orbital of a diatomic moiety with a double bond, etc.) or a plane (for a π^* orbital of a diatomic moiety with a triple bond, or for a σ^* orbital of an aromatic ring, etc.) Limiting ourselves to adsorbed species on substrates with threefold or higher symmetry alone, X-ray absorption peak intensities $I_v = \left(I_v^{//} + I_v^{\perp} \right)$ (when the spatial orientation of the antibonding orbital is defined by a vector) or $I_p = \left(I_p^{//} + I_p^{\perp} \right)$ (when the spatial orientation of the antibonding orbital is defined by a plane)} vary as a function of θ (the angle between the X-ray beam and the plane defined by the substrate surface). This variation is described by;

$$I_v = \left(I_v^{//} + I_v^{\perp} \right) = C^{//} \left\{ \frac{1}{3} \left[1 + \frac{1}{2} \left(3\cos^2 \theta - 1 \right) \left(3\cos^2 \alpha - 1 \right) \right] \right\} + C^{\perp} \left\{ \frac{1}{2} \sin^2 \alpha \right\} \quad (2.17)$$

$$I_p = \left(I_p^{//} + I_p^{\perp} \right) = C^{//} \left\{ \frac{2}{3} \left[1 - \frac{1}{4} \left(3\cos^2 \theta - 1 \right) \left(3\cos^2 \gamma - 1 \right) \right] \right\} + C^{\perp} \left\{ \frac{1}{2} \left(1 + \cos^2 \gamma \right) \right\} \quad (2.18)$$

where α is the angle between the vector defining the spatial orientation of the antibonding orbital (σ^* or π^*) and the surface normal. γ is defined as the angle between the vector and the surface normal. The coefficients $C^{//}$ and $C^{\perp}$ are related to the degree of polarization of the X-ray beam. If the beam is 100% polarized, i.e. the E-vector of all

photons in the beam is parallel to the plane defined by the Synchrotron ring, then $C^{//}=1$ and $C^{\perp}=0$. For the U12A beamline in NSLS facility Brookhaven National Labs, where we undertook our NEXAFS measurements, the tabulated $C^{//}$ and $C^{\perp}$ values are 0.95 and 0.05, respectively.

Equations (2.17) and (2.18) above clearly imply that we can determine α or γ by using a best fitting process of the corresponding X-ray absorption peak intensities as a function of the known θ. α or γ reveals the spatial orientation of the anti-bonding orbitals and hence the spatial orientation of the molecules. In order to this, though, one needs to process the raw NEXAFS data by taking the X-ray intensity variation as a function of beam energy into account, eliminating background signal arising from the substrate and eventual step-edge normalization. Typical normalization routines are extensively covered elsewhere. For the NEXAFS data presented here, the normalizations routines used are detailed in APPENDIX A.

2.1.4. Temperature Programmed Desorption (TPD)

TPD is a commonly used technique employing a mass spectrometer for the evaluation of desorbing yields and the kinetics of gas-evolving surface reactions. TPD spectra are taken during a thermal ramp of the surface temperature. Before the data acquisition, the head of the mass spectrometer must be brought into close proximity of the sample surface. Frequently, a conical skimmer with an opening smaller than the size of the sample face is employed as a barrier between the edges (and surrounds) of the sample, and the

ionization region of the mass spectrometer. Bringing the skimmer close to the sample surface therefore significantly reduces the detection of stray gas molecules desorbed from the sample holder and surrounds.

Only a small fraction of the gas molecules passing through the ionization region of the mass spectrometer ($\sim 1/10^4$) is ionized. In order to keep the direct proportionality between the number of desorbing moieties from the surface at a given time and the corresponding intensity of the MS signal, neutral gas molecules, once passed through the ionization region, should be removed irreversibly from the ionization volume. Therefore, it's a general practice to keep the mass spectrometers differentially pumped.

Gas molecules ionized in the ionizations regions are accelerated to a certain kinetic energy before they enter the mass filtering unit. The accelerated ions have the same kinetic energy regardless of their mass as long as they have the same charge, but have differing velocities. Most of contemporary mass spectroscopy devices are using quadruple mass analyzer for mass filtering. A quadruple analyzer consists of four rods running parallel to each other. In cross section each rod is placed at the corners of a square. Diametrically positioned rod pairs have a positive DC bias while the other pair have a negative bias. Strictly, the bias applied to the rods has DC and AC components ($U+V\cos(\omega t)$), and by variation of the bias ratio U/V applied, the ions with different m/z ratios are discriminated. Only the ions with a certain m/z have stable trajectories, can pass through the quadrupole region, and reach the detector.

Results from TPD are then usually interpreted in terms of the Arrhenius equation which, in this application, is also known as the Polanyi-Wigner equation:

$$I(\theta,T) = -\frac{d\theta}{dT} = -\frac{1}{\beta}\frac{d\theta}{dt} = \frac{\nu\theta^n}{\beta}\exp\left[-E_d\big/RT\right]$$

(2.19)

The desorption rate, I, can be defined in terms of the instantaneous surface temperature, T, and the fractional adsorbate coverage (normalized to that of saturation coverage), θ. ν is the pre-exponential factor of desorption, n the order of desorption, E_d the activation energy of desorption, β the temperature ramp rate (in Ks^{-1}), and R the gas constant. Given the use of the normalized coverage, θ, $0<\theta\leq1$, I is expressed in units of inverse temperature (K^{-1}), or strictly in fractional coverage per unit temperature, and ν in inverse time (s^{-1}).

Only if E_d and ν are independent of coverage, and a constant temperature ramp rate, β, is maintained during the sample heating, then E_d can easily be determined by using Redhead's Peak Maximum Method employing a number of TPD spectra from the samples with changing initial surface coverages or by simply determining the slope of an Arrhenius plot for a given single spectrum, i.e.

$$\frac{\partial\left[\ln\left(I\big/\theta^n\right)\right]}{\partial\left(1\big/T\right)} = -\frac{E_d}{R}$$

(2.20)

However, if E_d and/or ν are coverage dependent, and/or the constant temperature ramp rate, β, is not maintained, then the slope of the Arrhenius Plot is no longer equal to the $-E_d/R$, but:

$$\frac{\partial \ln\left(I/\theta^n\right)}{\partial\left(1/T\right)} = -\frac{E_d\left(\theta\right)}{R} + \left[\frac{\partial \ln \nu\left(\theta\right)}{\partial\theta} + \frac{1}{RT}\frac{\partial f\left(\theta\right)}{\partial\theta}\right]T^2 I - \left(\frac{\partial \ln\beta}{\partial\left(1/T\right)}\right) \qquad (2.21)$$

where $E_d\left(\theta\right) = E_d^0 + f\left(\theta\right)$. Evidently, even if ν and β are constant (i.e. coverage independent), the activation energy of desorption cannot be determined without foreknowledge of $f(\theta)$.

Two analysis techniques, named as Complete/Constant Coverage Analysis [29] and Leading Edge Analysis [30-32] have been developed to overcome the complications arising from the coverage dependence of the activation energy of desorption. However, application of either technique requires superior signal to noise ratios. We have developed a new analysis technique to figure out the activation energy of desorption in the limit of zero coverage, E_d^0, and its coverage dependent component, $f\left(\theta\right)$, for second order desorption kinetics without requiring superior TPD signal qualities.[33] In chapter 4, the details of this new approach will be reviewed extensively.

2.1.5. Reflection-Absorption Infrared Spectroscopy (RAIRS)

RAIRS is a specific vibrational spectroscopy utilizing infra-red beams to probe adsorbed moieties on thick, highly-reflective substrate surfaces, like single-crystal metal surfaces. [24, 34] The thickness of the substrate is an obstacle to the utilization of transmission IR. Therefore, the IR beam is projected to the surface at a grazing incidence. θ_{bn}, (the angle between the direction of the incident IR beam and the surface normal), which is slightly

less than 90°, and the a detector is located in the mirror position θ_{nd}, (the angle between the surface normal and the direction of the reflected IR beam, $\theta_{bn} = \theta_{nd}$.)

In a RAIRS investigation of a metallic surface, only the vibrational modes having dynamic dipole moments perpendicular to the surface plane can be detected by IR absorption. For example, a $\nu(X-Y)$, stretching vibration of a diatomic, polar, XY molecule is IR-visible (IR-active) if the molecular axis of the XY is perpendicular to the substrate surface and is IR-invisible (IR-inactive) if the XY molecular axis is parallel to the substrate surface. (Tilted XY molecules are still visible, yet their visibility reduces as their tilt configurations approach the parallel configuration). The reason behind this phenomenon is the image charges in the substrate induced by the dipole moment of the adsorbed moieties. For a polar molecule lying parallel to the surface, an image dipole of reverse direction is induced in the substrate. Since the total dipole of the system would be zero, the XY molecule in this spatial configuration on the surface is invisible in RAIR spectroscopy.

The range of vibrational frequencies observable in a specific measurement depends on several factors, including the IR source, optical components as well as the type of detector used. The IR source is an electrically heated chemically-inert solid material (e.g. SiC ceramic at ~1500 K) producing blackbody type polychromatic radiation in the IR range. The polychromatic source is then processed with a dynamic Michelson interferometer. The processing involves the splitting the beam in a half-silvered mirror into two (near equal intensity) beams, reflecting one beam from a fixed-position mirror

while the second beam reflects from a moving mirror, and recombining the two beams where they had originally split. The frequency components of the newly recombined beam are thus modulated at a rate which depends on the velocity of the moving mirror and, importantly, at a rate that is IR frequency dependent. An interferogram is recorded at the detector; the intensity vs time data is then to converted to intensity vs IR frequency data with Fourier transformation. The HgCdTe detector, utilized in our measurements, is capable the probing of vibrations within the 400-12500 cm^{-1} range. Note also that the number of moieties illuminated by an RAIR beam is significantly less than the number of moieties illuminated in transmission IR spectroscopy. Therefore, detectors used for RAIRS measurements are liquid nitrogen cooled to increase the signal-to-noise and sensitivity by reducing thermally induced noise levels. lN_2 cooling also improves the response time of the detector.

2.2.   Experimental Setups:

The data presented in this dissertation were collected in chambers in different locations. HAS, LEED and TPRD data were collected by using the experimental setup located in Wright-Rieman, Room 187, Rutgers.[35] TPD measurements presented in Chapter 4 were performed in the chamber specialized for TPD measurements located at Serin, Room 135, Rutgers.[36] XPS and NEXAFS measurements were made in U12a beamline of NSLS facility in Brookhaven National Labs.[37] RAIRS data is collected in NPL, Room 115, Rutgers.[38] In this chapter, the components and operational principles of the chamber located in Wright-Rieman, Room 187 will be briefly reviewed.

The helium beam is generated in the source chamber (Ch#1, of Fig 2.1) by expansion of UHP helium (99.999% purity) gas through a 20 μm orifice in a platinum nozzle disc. The helium is first passed through a liquid nitrogen cooled trap in order to eliminate any condensable impurities before reaching the nozzle. The helium pressure behind the nozzle depends on the nozzle temperature as well as the type of experiment, e.g. a good energy resolution of the He beam is a necessity for diffraction and TOF measurements, but not for uptake curve measurements. The following table gives some of the example nozzle temperatures and corresponding optimal helium pressure values.
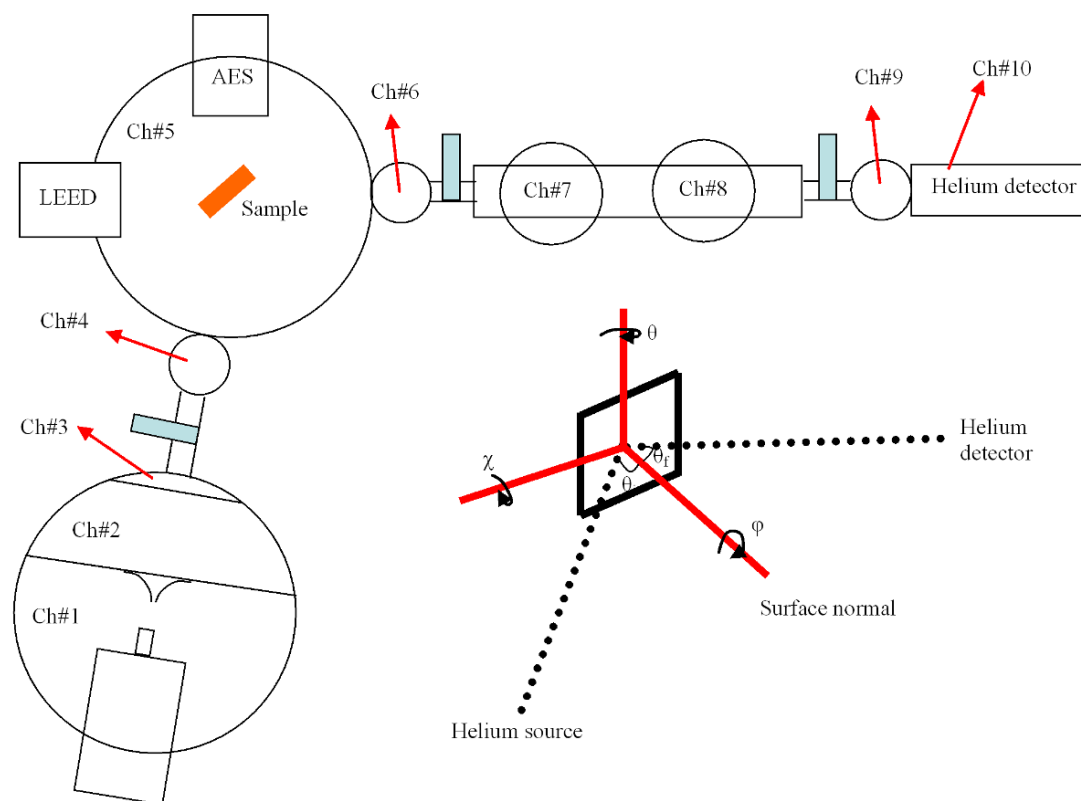
Figure 2.1   Systematic of the HAS experimental setup located in WR#187.

Nozzle Temperature ^{o}C (K)	Beam energy (meV)	Optimal Nozzle Pressure (psi)	$\Delta v/v$
-210 (63)	9-10	50-100	~0.9
-180 (93)	18-19	200-250	~1.2
-120 (153)	31-32	300-400	~1.3
-60 (213)	46-47	400-500	~1.5
0 (273)	56-57	~600	~1.7

Table 2.1.   Example nozzle temperatures and corresponding beam energies, optimal nozzle pressures and velocity distribution spreads.

As seen in the table, the nozzle pressure should be increased with increasing nozzle temperature in order to achieve optimum beam resolution in our experiments. The disparity between the beam energy implied by the nozzle temperature ($E_b = (5/2)kT$) and the actual beam energy is due to the limited accuracy of the temperature measurement, i.e. the nozzle temperature is measured with a thermocouple junction that is only in proximity to the nozzle support.

The expansion of helium from high pressures into vacuum, through a 20 μm nozzle, implies a large gas input into the chamber. Only a small fraction of the expanded helium passes through the 0.5 mm skimmer to enter chamber #2. The rest is pumped from the chamber #1 as quickly as possible before it can disrupt the tranquility of the jet stream. Thus, a large diffusion pump with 17,500 l/s pumping speed is used to achieve this goal. A vacuum booster is connected between the mentioned diffusion pump and the backing rotary pump in order to increase pumping throughput for high nozzle pressures (>300 psi)

The central portion of the jet stream, which passes through the skimmer, enters the second chamber. The helium beam is chopped into pulses by using a mechanical chopper, which is a 203 mm in diameter disc with four slits uniformly distributed on it. Each slit has an opening ~1mm. Assuming that the beam cross section is at ~1mm when it reaches the chopper and that the chopper rotates with a slit frequency of ~500 Hz, then each slit stays "illuminated" ~37 μsec. The FWHM of the approximately triangular response function is at about 18 μsec.

Once the beam is generated in chamber #1 and if necessary chopped in chamber #2, it passes through ch#3 and #4 to enter ch#5, which is our main scattering chamber. Both chambers 3 and 4 add differentially pumping. There is a gate valve separating one from another, so the beam source can be isolated from the sample chamber vacuum, if required. Chamber #4 hosts a special type of ion gauge to properly monitor the helium flux into chamber #5. There is an 8mm wide aperture separating Chamber 4 from chamber 5.

Our main chamber (ch#5) hosts the sample manipulator, which has three degrees of translation and three degrees of rotation as displayed in the inlet of Fig. 2.1. The background pressure of ch#5 can be as low as 5×10^{-11} Torr with the help of cryo- and titanium sublimation pumps in conjunction with a powerful turbo pump (Leybold TMP1000 with 1000 l/s pumping speed) backed in turn by a diffusion pump. In this background pressure range, Cu(001) surface can be kept clean for extended periods of

time (sample poisoning rate of <0.01 ML per day). Ch#5 is connected to four leak valves to administer gases into the chamber.

Ch#7 and Ch#8 are generally called TOF chambers. Their purpose is to extend the physical distance between the sample where scattering events happen and the mass analyzer in Ch#10 where scattered helium atoms are detected. With this extended distance provided by Ch#7 and Ch#8, the energy resolution between elastically and inelastically scattered helium atoms is enhanced. Finally, scattered helium atoms are detected by the mass spectrometer located in chamber 10. A relatively powerful turbo pump (Leybold TMP 360, 340 l/s,) backed by a diffusion pump, is connected to ch#10 to pump out the background helium atoms as quickly as possible.

2.3.   References

[1]   G. Benedek and J. P. Toennies, Surface Science 299-300 (1994) 587.
[2]   F. Hofmann, J. P. Toennies, and J. R. Manson, The Journal of Chemical Physics 101 (1994) 10155.
[3]   F. Hofmann, J. P. Toennies, and J. R. Manson, Surface Science 349 (1996) L184.
[4]   F. Hofmann, J. P. Toennies, and J. R. Manson, The Journal of Chemical Physics 106 (1997) 1234.
[5]   G. Lange and J. P. Toennies, Physical Review B 53 (1996) 9614.
[6]   G. Witte, P. Senet, and J. P. Toennies, Physical Review B 58 (1998) 13264.
[7]   J. Braun, G. G. Bishop, A. V. Ermakov, L. V. Goncharova, and B. J. Hinch, The Journal of Chemical Physics 110 (1999) 5337.
[8]   J. Braun, A. P. Graham, F. Hofmann, W. Silvestri, J. P. Toennies, and G. Witte, The Journal of Chemical Physics 105 (1996) 3258.
[9]   J. Ellis, J. P. Toennies, and G. Witte, The Journal of Chemical Physics 102 (1995) 5059.
[10]   A. P. Graham, Surface Science Reports 49 (2003) 115.
[11]   A. P. Graham, F. Hofmann, J. P. Toennies, G. P. Williams, C. J. Hirschmugl, and J. Ellis, The Journal of Chemical Physics 108 (1998) 7825.
[12]   F. Hofmann and J. P. Toennies, Chemical Reviews 96 (1996) 1307.
[13]   G. Witte, Surface Science 502-503 (2002) 405.

[14]   C. E. D. Chidsey, G. Y. Liu, G. Scoles, and J. Wang, Langmuir 6 (1990) 1804.

[15]   A. Glebov, A. P. Graham, A. Menzel, J. P. Toennies, and P. Senet, The Journal of Chemical Physics 112 (2000) 11011.

[16]   M. Patting, D. FarÃas, and K. H. Rieder, Physical Review B 62 (2000) 2108.

[17]   F. Schautz and H. J. Flad, The Journal of Chemical Physics 112 (2000) 4421.

[18]   G. Comsa and B. Poelsema, Applied Physics A: Materials Science & Processing 38 (1985) 153.

[19]   B. Poelsema and G. Comsa, Scattering of Thermal Energy Atoms from Disordered Surfaces, Springer-Verlag, 1989.

[20]   R. B. Doak, U. Harten, and J. P. Toennies, Physical Review Letters 51 (1983) 578.

[21]   J. L. Beeby, J. Phys. C: Solid State Phys. 4 (1971) L359.

[22]   R. B. Doak, ed., Single Phonon Ineleastic Helium Scattering, Atomic and Molecular Beam Methods, Vol. Volume 2, Oxford University Press, Inc., New York, 1992.

[23]   B. Gumhalter, Physics Reports 351 (2001) 1.

[24]   D. P. Woodruff and T. A. Delchar, Modern Techniques of Surface Science, Cambridge University Press, Cambridge, 1986.

[25]   M. H. Kibel, ed., X-Ray Photoelectron Spectroscopy, Surface Analysis Methods in Material Science, Vol. 23, Springer-Verlag, 1991.

[26]   J. C. Riviere, Surface Analytical Techniques, Oxford University Press, New York, 1990.

[27]   D. A. Shirley, Physical Review B 5 (1972) 4709.

[28]   J. Stohr, ed., NEXAFS Spectroscopy, Springer Series in Surface Science, Springer-Verlag, 1992.

[29]   D. A. King, Surface Science 47 (1975) 384.

[30]   A. M. Jong and J. W. Niemantsverdriet, Surface Science 233 (1990) 355.

[31]   D. L. S. Nieskens, A. P. Van Bavel, and J. W. Niemantsverdriet, (2003)

[32]   E. HabenSchaden and J. Kuppers, Surface Science 138 (1984) L147.

[33]   E. Z. Ciftlikli, E. Y. M. Lee, J. Lallo, S. Rangan, S. D. Senanayake, and B. J. Hinch, Langmuir 26 (2010) 18742.

[34]   Y. J. Chabal, Surface Science Reports 8 (1988) 211.

[35]   L. V. Goncharova, J. Braun, A. V. Ermakov, G. Bishop, D.-M. Smilgies, and B. J. Hinch, Journal of Chemical Physics Vol. 115 No 16 (2001) 7713.

[36]   J. Lallo, E. V. Lee, R. Lefkowitz, and B. J. Hinch, Surface Science 606 (2012) 320.

[37]   http://beamlines.ps.bnl.gov/beamline.aspx?blid=U12A.

[38]   L. Tskipuri and R. A. Bartynski, Surface Science 603 (2009) 802.

CHAPTER 3

Helium Atom Scattering investigation of static and dynamic properties of the CN/Cu(001) surface

3.1. Motivation:

Cyanide containing chemical moieties are important for both scientific studies and in commercial applications of heterogeneous catalysis; they can be found as reactants, products and reaction intermediates. The simplest of the cyanide containing moieties is the cyanide ion (CN^-). Its isoelectronic character with CO and NO^+ groups draws additional interest in investigations of the adsorption properties of the CN^- anion on surfaces. Although CN adsorption has been extensively studied on a number of $fcc(110)$ surfaces, the extent of studies on CN adsorption on $fcc(001)$ and $fcc(111)$ surfaces is quite limited. This scarcity is linked with the e-beam damage of CN species adsorbed on (001) and (111) surfaces, which limits the interpretation of some of the basic surface experimental technique results such as those of low-energy electron diffraction (LEED) and Auger electrons spectroscopy (AES). Indeed, there is no published LEED study of CN/$fcc(001)$ or CN/$fcc(111)$ in the literature.

HAS, employing thermal helium atoms, does not have the destructive effects of e-beams. Therefore, the identification of ordered superstructures of CN/Cu(001) by using angle resolved HAS is one of the main objectives of this study. Such He diffraction studies will be used in conjunction with XPS based coverage calibrations, and Near Edge X-Ray

Absorption Fine Structure (NEXAFS) studies (which give information on the orientation of differing CN moieties on the surface), to realize important structural information in the CN/Cu(001) surface. In addition, TOF-HAS measurements, which discriminate the back-scattered helium atom energies, would shed additional light on both the static and dynamical character of the CN species. Such information cannot be probed by other conventional surface techniques. Overall, we shall demonstrate that HAS is a powerful spectroscopic tool to elucidate surface properties of many comparatively complex adsorbates on single crystal metal surfaces.

3.2. Introduction

Cyanide is a potent ligand and pseudohalogen with a strong affinity for forming ionic compounds or complexes with many transition metals. Cyanides have a number of uses in a large number of industries, notably in mining and electroplating [4]. Also, as cyanide is isoelectronic with NO^+ and CO, it is often used in comparative studies. There has therefore been much interest in the properties of cyanide-surface binding on metallic faces [5, 6].

The nature of CN^- bonding to the surface is a long considered question. Early expectations were that CN^- bonding is quite similar to the CO, since they are isoelectronic and the sequence of molecular orbital energy levels for both species is also identical. CO coordination to transition metal surfaces is considered highly covalent in character, involving σ electron donation from CO to the metal and π-back donation from

the metal to the low-lying $2\pi^*$ molecular orbital of CO.[7] However, computational studies for adsorbed CO and CN$^-$ species on various transition metal surfaces, using cluster model approaches and density functional theory, indicate that there are major differences between CO and CN$^-$ species.[5, 8] While the net charge transfer to the CO is quite small because of the σ donation and π back donation balance, a 0.2 to 0.4 e$^-$ charge transfer upon adsorption from the 5σ orbital of a CN$^-$ moiety to metal surfaces occurs without π back donation from a substrate to the CN$^-$ moiety. The lack of the π back donation process for the CN$^-$ adsorption is attributed to the inhibitory effect of substrate polarization due to the negatively charged CN$^-$ adsorbate. Therefore, the covalent contribution to the M_x-CN bonding is basically of single sigma bonding character, involving the coupling between the 5σ valence orbital (HOMO) of CN$^-$ and the 4sp band of the copper atoms. However, the main contribution to the total bonding is ionic; i.e. M-CN$^{\delta-}$ bonding is largely due to the electrostatic attraction of CN$^{\delta-}$ to the image charge in the polarizable metal surface. High work function changes upon saturation, (e.g. 0.5 eV for adsorption on Pt(001) [9], or 0.95 eV for adsorption on Pd(110) [10]) is consistent with significantly negatively charged CN$^{\delta-}$ adsorbed species. While T_{des} of the CO species adsorbed on Cu(111) is as low as 170 K [11], the first desorption from a CN$^{\delta-}$/Cu(111) sample is seen at a temperature as high as ~700 K [12]. Similarly for the Cu(001) substrate, the desorption temperature is 190 K for CO [13] while we have measured a temperature of 700±25 K in our laboratory for desorption of C_2N_2 originating from the CN$^{\delta-}$ species [14]. Any large difference in T_{des} must be attributed essentially to the difference in the ionic interaction strengths between CN$^{\delta-}$ moieties and the surfaces.

CO is bonded to most metallic surfaces with a perpendicular orientation. Highly directional and symmetry constrained π back donation interactions between orbitals of the substrate atoms and $(2\pi_x^*, 2\pi_y^*)$ orbitals of the adsorbed CO moiety must be the reason behind this phenomenon. As $CN^{\delta-}_{(ads)}$ species do not have such significant π back donation, they could show molecular orientations on surfaces which are different from those exhibited by adsorbed CO. However, the existing literature shows that the systems are not easily elucidated. As an illustrative example, there are numerous experimental studies on CN adsorption on Pt(111) surfaces [15-19], which yield divergent structural interpretations. Yet, the commonly held belief is that $CN^{\delta-}$ species have horizontal orientations above close packed metal surfaces. The absence of v(CN) in vibrational spectroscopy results throughout the literature is assumed to be principal proof for the horizontal orientation of CN species on various (100) and (111) metal surfaces. However FTIR spectra of both gas phase HCN [20, 21] and HCN/Cu(001) surfaces [22], at which HCN species are physisorbed perpendicularly to the copper surface, shows inherently very weak v(CN) intensities. Therefore, it is difficult to assume horizontal spatial orientation for the adsorbed CN moieties based on the absence of a v(CN) mode in corresponding IR spectra. That said, there are other experimental studies employing ARUPS [10] and N K-edge NEXAFS [23] techniques which have predicted horizontal alignments for CN species adsorbed on various metal surfaces.

A computational study of $CN^{\delta-}$ coordination, on a Ni(001) surface [24], returns interesting structural information; a horizontal alignment with a $CN^{\delta-}$ moiety located above a hollow site was determined to be the most stable configuration. Yet, other

configurations (e.g. with perpendicular alignment with N close to the surface or C close to the surface, or several tilted configurations, and on various bonding sites, i.e. hollow, bridge, on-top) return very comparable binding energies, separated by <1.5 kcal/mol. And the activation barriers for consecutive side-on/tilted/end-on transitions were predicted to be <1.5 kcal/mol also. If we compare a thermal energy at ambient temperatures, which is kT~26 meV ~ 0.3 kcal/mol, with the activation barrier figures presented above, we may conclude that a $CN^{\delta-}$ moiety can rotate "frequently" at ambient sample temperatures. These calculations are implying that CN moieties are able to diffuse, tumble, and helicopter over a close-packed metallic face.

Most of the structural studies for CN on surfaces were performed for fcc(110) surfaces [10, 25] where a c(2x2) geometry is observed. For C_2N_2 adsorbed on Cu(111), no ordered surface phase was observed with LEED studies. However, the CN saturation coverage on Cu(111) was measured as 0.2 ML using TPD [12]. The only structural indication, related to CN on (001) surfaces dates back to 1976, reported by F.P Netzer [26] , for cyanogen adsorbed on a Pt(001) surface. According to this article, a coverage dependent structural analysis by LEED for CN^-/Pt(001) system shows a (5x1) pattern at moderate coverage. The (5x1) pattern disappears with increasing coverage and eventually results in a (1x1) diffuse pattern at saturation. This behavior was attributed to a densely packed adsorbate layer (out of registry with substrate) and the conversion to 1x1 was attributed to the appearance of a para-cyanogen polymer, extending along the <110> azimuth. However this hypothesis is in contradiction with most TPD studies, which see that C_2N_2 desorption is mostly second order in character.

In the first part of this chapter, we aim to identify the ordered superstructure of C_2N_2 saturated Cu(001) surface employing monochromatic helium beams. Thermal helium atoms, with de Broglie wavelengths in the order of 1 Å, are suitable probes for crystalline surface diffraction experiments. Helium atoms with kinetic energies of 10-50 meV exhibit Lennard Jones like interactions with the top-most monolayer of a surface and are scattered without inducing any changes in intra surface chemical interactions or surface destructive effects. Thus, angle resolved HAS results are expected to be able to succeed where LEED studies fail, e.g. in identification of an ordered superstructure of a saturated CN/Cu(001) surface. This structural information will be augmented by coverage calibrations using XPS which will reveal the number density of the CN species on the substrate. NEXAFS measurements will be used to contrast CN species based on their spatial orientations. And finally, dynamic features of CN/Cu(001) will be probed by employing TOF-HAS.

3.3.   Experimental

The experimental apparatus for Helium atom scattering (HAS) is described in the literature in detail.[27] A highly monochromatic helium beam ($\Delta V/V \sim 1\%$) is produced by a supersonic jet expansion of high pressure UHP (99.999%) helium gas into vacuum through a 20 μm nozzle. The beam passes through 0.5 mm skimmer into chamber #2, which only lets the central part of the beam pass, producing a highly directional and near monochromatic He beam. We have the power of varying the kinetic energy of the helium atoms in the 10-70 meV range with the help of a helium compressor unit which is in

thermal contact with nozzle. Depending on the intended experiment, a chopper, placed in chamber #3, can be moved into the beam between the source and the (sample) target, and can produce up to 500 He pulses per second with the gating fraction of ~1%.) The sample manipulator in Chamber #5 gives us three degrees of angular freedom, i.e. we can use stepper motors to change the polar, tilt and azimuthal positioning of the substrate with respect to the incident helium beam and scattering plane. Certain reflected He atoms, after passing through the chambers #6,#7,#8 and #9, can reach the quadrupole mass analyzer situated in chamber #10. The base pressures of chambers #5 and #10 are low, $\sim 5 \times 10^{-11}$ Torr and $\sim 1 \times 10^{-10}$ Torr, respectively.

XPS and NEXAFS measurements were performed at the Brookhaven National Laboratory NSLS facility on beamline U12A.(supported by the U.S. Department of Energy, Office of Science, Office of Basic Energy Sciences, under Contract No. DE-AC02-98CH10886.) The experimental setup is equipped with a 125 mm hemispherical Omicron VSW EAC2000 electron analyzer for XPS measurements. A monochromatic photon beam energy of 650 eV was used to probe surfaces. Using a fixed analyzer transmission mode with a pass energy of 10 eV, and 100x100 slits, an energy resolution of ~ 0.2-0.3 eV is achievable. All binding energies cited here are referenced with respect to substrate bulk copper Cu $3p_{1/2}$ and Cu $3p_{3/2}$ binding energies at 78.0 and 75.2 eV, respectively. Photons fluxes were normalized for all spectra by referencing to the monitored emission signal from a gold mesh. Resultant XPS spectra were then normalized with respect to the Cu 3p peak intensity. For this purpose, in-situ measurement of Cu 3p peak intensities followed every sequence of C 1s, N 1s and/or O

1s peak measurements. For the NEXAFS measurements, a separate detector running in partial electron yield (PEY) mode is employed. As the number of Auger electrons emitted from the surface is directly proportional to the number of X-ray absorption events, a biased grid at -300V is positioned between the sample and the detector in order to eliminate a large fraction of concurrent secondary electron and photoelectron emission signals.

Cu(001) surface is prepared for the experiments with cycles of 1keV (>10 μA) Ar^+ or Ne^+ sputtering for 15 minutes, and annealing to 673K for 10 minutes. The initial cleanliness of the sample surfaces was probed either by XPS or with He atom reflectivity. For the clean, room temperature, Cu(001) surface the specular helium reflectivity is typically as large as 20%.

In the HAS system, the Cu(001) surface was exposed to C_2N_2 through backfilling of the chamber. Exposures reported for the HAS experiments are thus based on time integrated readings of an ion gauge within the UHV chamber. In U12a beamline experiments, on the other hand, a directional doser was employed to introduce C_2N_2 to the surface. In both cases the cyanogen (C_2N_2, 99% purity) was supplied by Linde gas.

3.4. Results and Discussion

3.4.1. Formation and characterization of an ordered superstructure formed with CN/Cu(001) surfaces

C_2N_2 adsorption on transition metal surfaces is believed to be predominantly dissociative at ambient sample temperatures. TPD studies on the desorption of C_2N_2 from Cu(111)[12] and Rh(111) [28] show the coexistence of α and β desorption states, where T^{α}_{des} is independent of the coverage level (i.e. exhibiting first order kinetics) while T^{β}_{des} shifts to lower temperatures with increasing coverage (i.e. indicative of second order kinetics). However, the fractional population of the α adsorbate state, which may come from a molecularly adsorbed C_2N_2 species, is less than 5% of the total population of desorbed C_2N_2 species [28]; i.e. the majority of the adsorbate population is presumed to be adsorbed as $CN^{\delta-}$ species, which can associatively desorb from the surface only at temperatures higher than that for direct molecular desorption.

C 1s and N 1s lines probed by XPS are presented (Figs. 3.1(a) and 3.1(b), respectively) from the surfaces prepared with C_2N_2 exposures on Cu(001) at 173 K and 263K. While the C 1s and N 1s spectral features associated with surface species deposited on the surface at 263 K are indicative of a single type of surface moiety, C_2N_2 exposures at 173K produces complex XPS lines, which is indicative of multiple surface species. We believe that the complex nature of the spectra upon 173K exposures indicates the

coexistence of CN and C_2N_2 species on the surface. On the other hand a surface prepared

at 263K, a nearly ambient temperature, leads to a CN-only surface.
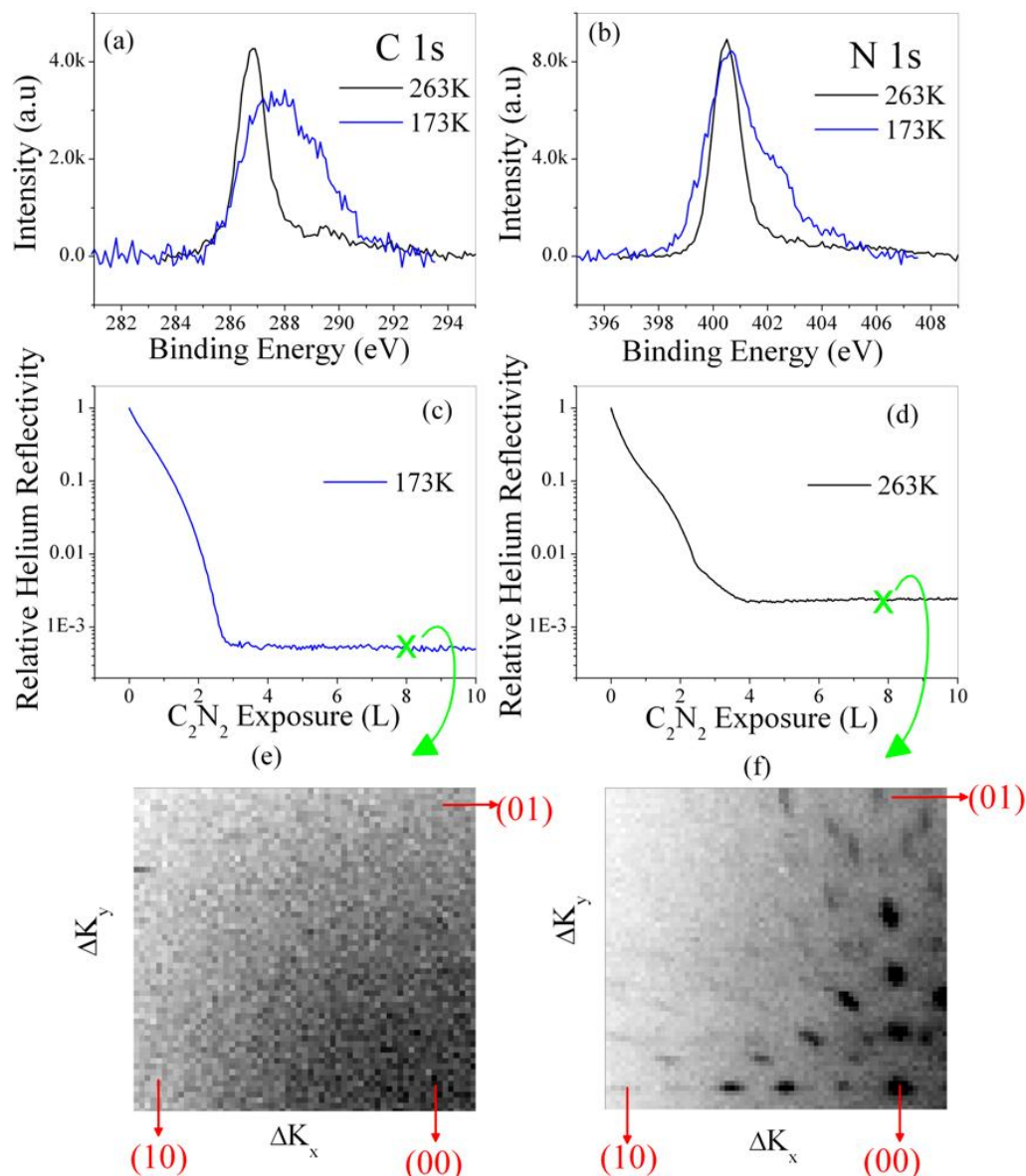
Figure 3.1.   (a) and (b) XPS scans of saturation exposures of cyanogen. (a) C 1s and (b) N 1s spectral features.   The blue curves indicate the results of exposures and measurements made at 173K, whereas the black curves, indicating narrower peaks, are for exposures and measurements at 263K. (c) and (d) Helium reflectivity decreases as a function of cyanogen exposures on Cu(001) at two sample temperatures: 173K and 263K in (c) and (d), respectively. (e) and (f) Angular resolved intensity in HAS from saturated surfaces prepared and measured at 173K and at 263K, respectively. Monochromatic helium beams with E_i = 31.2 meV and $\Delta v/v$~ 1.2% were used.

In contrast to the Cu(111) surface (at which C_2N_2 exposures at ambient temperatures leads to a surface accommodating C_2N_2 (~6%) and CN (~94%) moieties together [12]), C_2N_2 exposures on Cu(001) at ambient temperatures do not yield any physisorbed C_2N_2 moiety.

Monitoring the decay of helium reflectivity during the C_2N_2 exposures at 173K and 263K (Figs. 3.1(c) and 3.1(d), respectively) show some differences between adsorption kinetics at these two adsorption temperatures. Though, surface saturation does occur at very similar total exposures, differences in the shapes of the uptake curves suggest ordering phenomena of different natures. The lowest temperature curve, Fig. 3.1(c), is an archetypal curve showing strongly repulsive mutual interactions between adsorbed species, such as would be anticipated for CN^- - CN^- dipolar interactions. The higher temperature curve, Fig. 3.1(d) indicates an ordering process that can occur with mobile species. Later in this chapter we will show that an ordered phase starts to develop, at the exposure level where the curvature of relative helium reflectivity first turns from positive to negative. The eventual helium reflectivity at saturation is at only 5×10^{-4} for a sample prepared at 173K while it is 3×10^{-3} for one prepared at 263K. The higher reflectivity at saturation, for the latter, tentatively results from coherent diffraction from an ordered surface structure.

Verification of this hypothesis was possible through angle resolved HAS spectra taken from the saturated surfaces prepared through C_2N_2 exposures at 173K and 263K, as presented in Figs. 3.1(e) and 3.1(f), respectively. While the 173K adsorption returns no

resolvable diffractive features, but only a broad diffuse background peaking at around the specular (00), the sample prepared at 263K leads to the appearance of a rich diffractive pattern shown in Fig. 5.1(f). At 263 K the diffraction pattern is not sufficiently well formed to securely identify the ordered phase, though it is clear that an ordered superstructure with a square unit cell is not formed.

At this point let us underline the fact that the observation of the ordered surface structures upon C_2N_2 exposures depend on the temperature at which adsorption occurs. For example, the subsequent annealing at 263K and 323K of the surface prepared at 173K does not lead to a discernable diffraction pattern. Cooling of the sample, which was prepared at 263K, helps to intensify the diffraction peaks. We also examined the sample prepared through C_2N_2 exposures at 323K. This "high temperature" surface preparation still yields an ordered phase quite similar to the one presented in Fig. 5.1(f). However, the clearest diffraction patterns with strongest peak intensities are always achieved when the CN moieties are deposited on the Cu(001) surface at around 263K.

In order to identify clearly the ordered phase observed in Fig. 3.1(f), we chose to reduce the nozzle temperature from -120 ^{o}C to -180 ^{o}C; the beam energy is reduced from 31.2 meV to 17.6 meV. This has the effect of reducing a Debye Waller factor and increasing the observed diffraction feature intensities. The sample is prepared at 263K and kept at that temperature during the data acquisition. The detailed angle resolved HAS scan along the <110> azimuth is presented in Fig 2(a), indicating the superposition of 5th order and 3rd order diffraction features along the same azimuth. We conclude that the CN species

deposited on Cu(001) at 263K are forming a c(10x6) ordered superstructure. The superposition of 5th order and 3rd order diffractive features results from the cumulative probing of two domains; one is a 90° rotated version of the other.
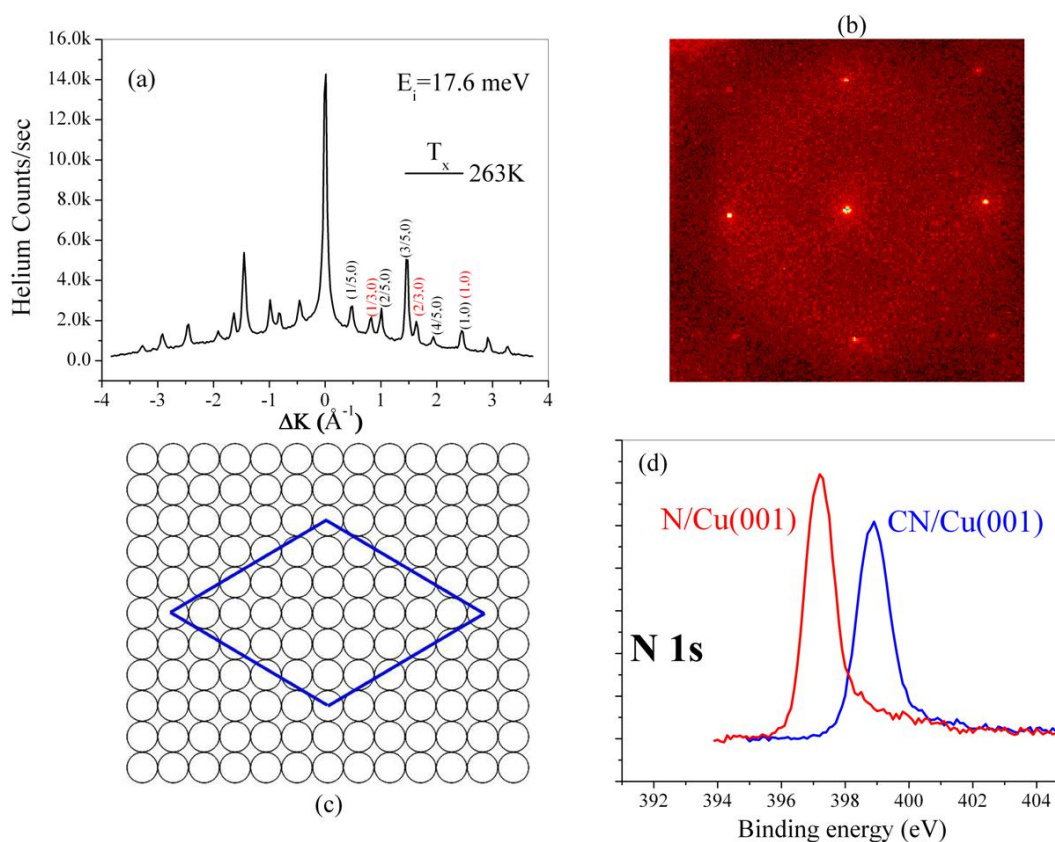
Figure 3.2.   The saturated CN/Cu(001) prepared at 263K probed by angle resolved HAS, (a), taken along the <110> scattering azimuth displays diffraction features from an ordered superstructure of CN moieties having a c(10x6) translational symmetry. $E_i =$ 17.6 meV. The same surface probed by LEED, with 240 eV electrons, returns a (1x1) and diffuse pattern, (b). The mesh of a primitive unit cell of an ordered c(10x6) superstructure is portrayed in (c). The CN coverage at saturation is determined by comparing the N 1s line intensity associated with the saturated CN/Cu(001) and that of a 0.5 ML N/Cu(001) surface, (d).

The LEED pattern of the same sample shows only a (1x1) pattern, which does not convey the same information as do the angle resolved HAS results. This contrast together with

the lack of any published LEED pattern from CN species adsorbed on *fcc*(001) surfaces implies that an electron beam as employed in LEED disrupts overlayer ordering of a CN species. Our He beam illuminates the majority of a 1 cm^2 surface. The same is not true of the incident LEED beam. Although we have tried to illuminate the surface with another e-beam gun, which has the potential of producing an e-beam as broad as the diameter of the sample, we were not able to demonstrate conclusively that a high current 250eV e-beam inflicts irreversible damage to a CN/Cu(001) surface.

Regardless of the nature of e-beam damage, the undisturbed saturated surface has a c(10x6) ordered overlayer of CN moieties, suggesting a basic unit cell as shown in Fig. 3.2(c). The primitive unit cell covers the area of 30 copper atoms on the (001) surface. In order to determine the number density of CN, we have performed the coverage calibrations using XPS. Our calibration standard, a saturated N/Cu(001) surface, prepared by N$^+$ sputtering ($E_i = $ 1keV, >5000μC) followed by a brief annealing at 600K, shows a single N 1s XPS line at 397.2 eV (Fig. 3.2(d)). STM and Rutherford backscattering studies [29-31] have confirmed that this procedure produces an N saturated surface with a c(2x2) superstructure extending fully across the surface with an absolute coverage of 0.5ML. The N 1s XPS line associated with the saturated CN species adsorbed on Cu(001) through C$_2$N$_2$ exposures at 263K is shown in Fig. 3.2(d) also. Comparison of the two spectra displayed in Fig. 3.2(d) suggests a saturation coverage of the CN species on Cu(001) at ~0.41 ML. This result implies that there should be 12-13 CN moieties placed in the unit cell shown in Fig. 3.2(d), if the ordered super structure extends over the entire surface.
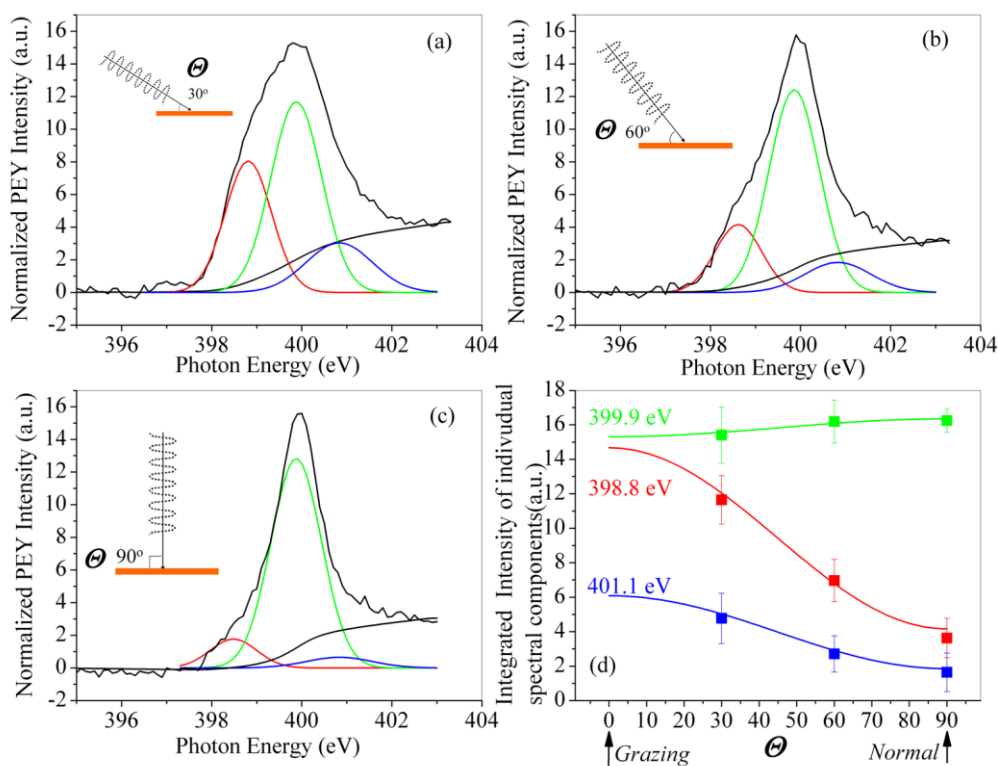
Figure 3.3.   Normalized nitrogen K-edge NEXAFS intensities in 1s-π^* spectral region as a function of photon energy from a saturated CN/Cu(001) surface at 263K. Measurements were performed at three different angle of incidence, (a) 30°, (b) 60° and (c) 90°. The NEXAFS detector was operated in PEY mode with a biased grid at -300V positioned between the sample and the entrance of detector. Intensity variations of the NEXAFS components at 399.2 eV, 398.78 eV and 401.10 eV are analyzed, as proposed elsewhere [32], to determine the spatial orientations of the CN moieties giving rise to the three NEXAFS components. Analysis results are summarized in (d). Further discussion of the curves is found in the text below.

Our NEXAFS investigation of the saturated CN/Cu(001) surface, as prepared at 263K, concentrates on the X-Ray absorption event causing the excitation of N 1s core electrons into unoccupied π^* molecular orbitals. 1s-π^* absorption produces sharper and more intense spectral features in NEXAFS compared to 1s-σ^*; i.e. a quantitative analysis of the former is considerably easier than that of the later. Figs. 3.3(a), 3.3(b) and 3.3(c) are

displaying three NEXAFS spectra of the identical CN/Cu(001) surface probed with changing angle of incidence of the photon beam with respect to the plane defining the substrate surface. The stark contrast between the simple and single-featured XPS spectrum of N 1s line (Fig. 3.1(b), black curve) and topographically complex 1s-π^* X-Ray absorption features observed in NEXAFS results (Figs. 3.3(a), 3.3(b) and 3.3(c)) is due to the sensitivity of the π^* energy levels to the adsorption site and spatial orientation of the adsorbed moieties. Core electron energies do not reflect similar sensitivity.

Deconstructed NEXAFS results for 1s-π^* absorption are suggesting at least 3 different types of CN moieties on Cu(001) distinguished from each other based on their binding site and/or spatial orientation. The reason for the observation of 3 NEXAFS features from a surface, which produces only a single resolvable XPS feature, must be related to the higher sensitivity of anti bonding orbital energies to factors including binding sites and/or spatial orientations. Variation of the integrated intensity of each spectral component (at 398.8 eV, 399.9 eV and 401.1 eV) as a function of the angle of incidence of the polarized synchrotron light beam to the surface plane reveals information on the spatial orientation of the associated CN moieties.[32] Note: the three NEXAFS features are at fixed peak positions and are taken to have respectively constant FWHM energy widths of 1.03 eV, 1.12 eV and 1.39 eV. The dependences of fitted intensities with incident light angles, and their tentative evaluations, are described below.

As the intensity of the 399.9 eV component is nearly constant with varying beam incidence angle, Θ, (as shown by the green curve of Fig. 3.3(d)), Eq. (2.18) suggests it

can be associated with triple bonded CN moieties with molecular axes being close to the magic angle (54.74^o) away from the surface normal. (Our best estimate is at 53°±3°.) Alternatively the same signal could arise from double bonded CN moieties whose molecular axes are on average 37° away from the surface normal. For this intensity component, with little to no intensity variation, it is impossible to say whether the π^* orbitals are plane-polarized (indicative of a triple bond between C and N atoms) or vector-polarized (indicative of a double bond between C and N atoms). Equally, this component at 399.9 eV can be associated with cartwheeling CN moieties. Indeed, a computational study on CN$^-$ coordination on a Ni(001) [24], which were previously noted in Section 3.2, predicts activation barriers for consecutive side-on/tilted/end-on transitions to be as small as <1.5 kcal/mol.

For the NEXAFS components located at 398.8 and 401.1 eV, the intensity of the feature at normal incidence is discernibly smaller than 50% of the intensity of the same component at grazing incidence.(Fig. 3.3(d)). This observation dictates that these NEXAFS components *cannot* be associated with plane-polarized π^* orbitals, i.e. associated CN moieties cannot have triple bonds. Fitting the intensity variations of these two features at 398.8 and 401.1 eV suggest that they are associated with vector-polarized CN moieties (double bonded) whose molecular axes are both ~50° off the surface normal. For clarification, the polarization vector of the anti bonding π^* orbitals in these cases are making an approximately 40° angle to the surface normal. One could speculate that the two types of double bonded CN moieties, having nearly identical spatial orientations while yielding two different X-Ray absorption energies (398.8 and 401.1 eV), can have

two different binding sites. However, a more plausible attribution would be that these two NEXAFS components are associated with two types of CN moiety, which are bound on near identical adsorption sites. The key N 1s difference would arises from which, C-atom or N-Atom end is "down" (closer to the substrate plane). The following scheme visually outlines all possible CN configurations, deduced by the application of Eqs. (2.17) and (2.18), attributable to the NEXAFS features observed at 399.9, 398.8 and 401.1 eV.
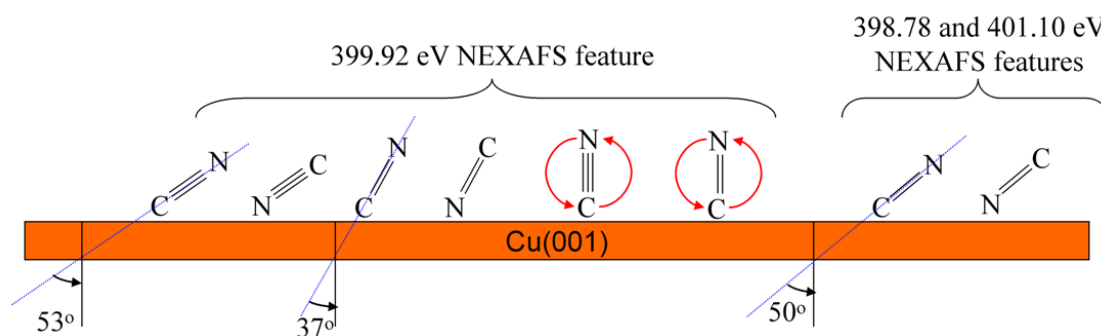
3.4.2. HAS investigations of sub-saturation CN/Cu(001) surfaces

We examined the change of the angle resolved HAS patterns along the <110> scattering azimuth as a function of increasing CN exposures at 263K to gain some insight into the sequence of events happening with a gradual uptake of the CN concentration on the surface. 17 exposure levels were examined and corresponding diffraction patterns are presented in Fig. 3.4(a). Uptake curves constructed from data of 17 angular scans show the decay of specular reflection, I_{00}, (Fig. 3.4(b)) which is very similar to the uptake curve presented in Fig. 3.1(d), i.e. it is possible to relate the visible topographical features of the uptake curve with the angle resolved HAS spectra. The intensity of the 1st order diffraction peak, I_{10}, located at ~2.45 Å^{-1}, grows very quickly with the first aliquots of

C_2N_2 exposures and reaches its maximum at the exposure level of ~1L before it starts losing intensity in an equally quick manner with further increasing exposure levels. This abrupt up and down variation of the I_{10} peak before the 2L exposure level does not require the development of an ordered surface structure.
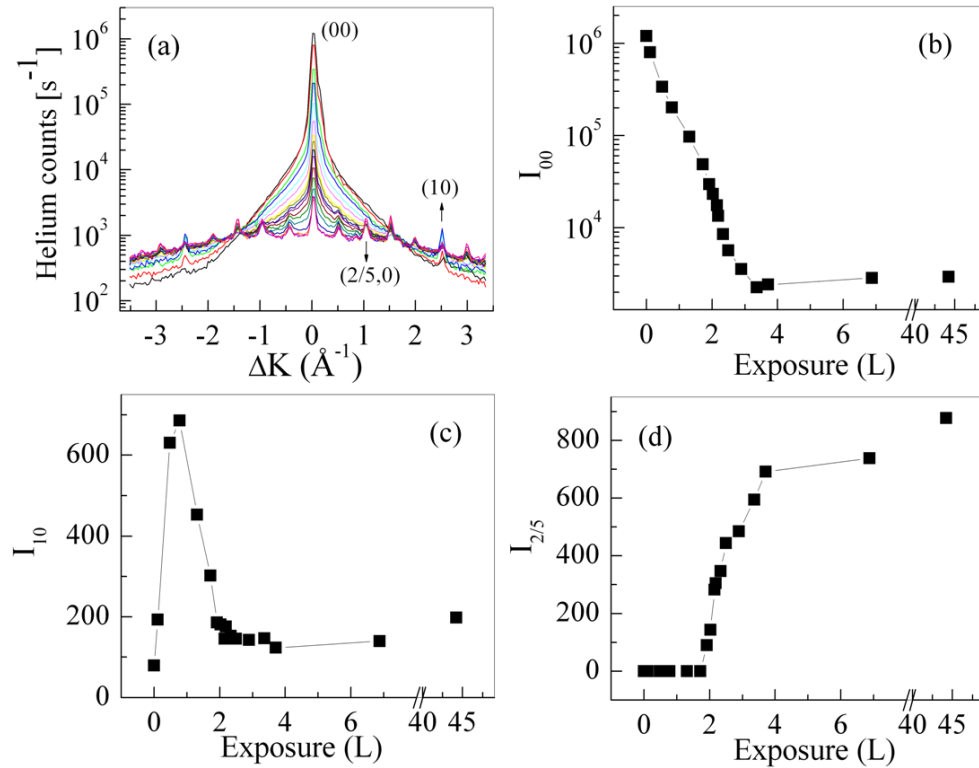
Figure 3.4.   (a) Development of the angle resolved HAS at 17 exposure levels in the process of forming saturated CN/Cu(001) surface at 263K. Intensity variations of I_{00}, I_{10} and $I_{2/5}$ diffraction features, after background subtractions, with increasing exposures are presented in (b), (c) and (d) respectively. $E_i = 31.2$ meV.

The scattering cross section of CN moieties could easily be as high as 100 Å^2. i.e. the mirror-like character of the Cu(001) surface is obliterated over an area of ~10-12 Å diameter for each CN moiety on the surface.   The He amplitude lost from the (00) direction is spread widely over angular space. Coherent addition of that amplitude is to be expected at non-(0,0) substrate diffraction conditions only when the gas species are arranged as a lattice gas. A set of identical CN bumps (as seen by a He wave front), on

equivalent sites gives rise to a (10) intensity when other potential superlattice intensities see no intensity increases. The sudden drop in the (10) intensity arises from an inequivalence of CN scatterers, as seen by the He atoms. The "inequivalence" can result from inequivalent adsorption sites, but at these low coverages it is more likely due to the onset of overlap between the bumped regions. The rapid drop in the (10) intensity is indicative of a clustering process, the onset of which is found at ~ 1L of C_2N_2 exposure.

Fig. 3.4(d) displaying intensity variation of 2/5th diffraction peak intensity indicates that it is not until an ~2L exposure level that a superstructure with long range order can start to develop on the surface. In the uptake curve (of specular intensity) at ~2L exposure the helium reflectivity curvature turns from positive to negative. From 2L to 4L, we see the quick development of an ordered superstructure. The change of the $I_{2/5}$ growth rate as a function of C_2N_2 exposure observed at ~2.5L coincides with the feature observed at the same exposure level in Fig. 3.1(d). Further exposures of C_2N_2 up to the 45L level leads only to slow increases in the peaks associated with the ordered phase.

3.4.3. TOF-HAS investigation of CN/Cu(001) surfaces

Another interesting feature observed in the helium diffraction intensity scans is the development of a broad background, which grows as the $CN^{\delta-}$ coverage increases. The tails of the specular peak for the clear Cu(001) and for low coverage CN/Cu(001) surfaces forms a triangular shaped feature extending from -2 Å^{-1} to 2 Å^{-1} in the logarithmic plot of the angle resolved HAS pattern (Fig. 3.4(a)) This feature is due to the

largely single-phonon inelastic scattering from the exposed copper surface.[44] As the surface coverage of CN species increases, the single phonon component from the bare copper surfaces diminishes as less and less copper surface remain uncovered by CN moieties. Simultaneously, we observe the development of another broad background, which extends through the whole range of reciprocal space. Fig. 3.5(a) illustrates the development of this background by monitoring its intensity at 3.4 Å^{-1}, i.e. at a ΔK point where no diffraction peak appears. It is apparent that the newly forming background starts to develop with the first aliquots of C_2N_2 exposures and continues to grow up to the 4L exposure level.
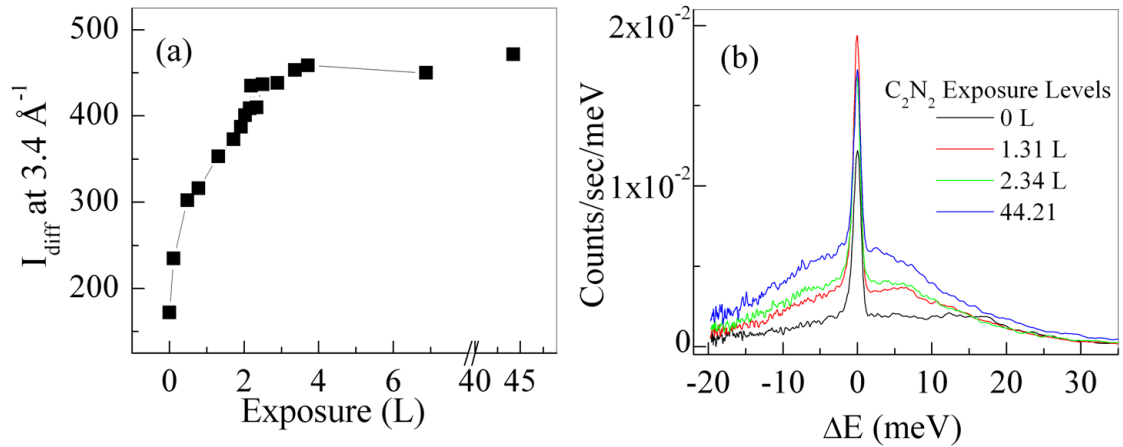
Figure 3.5. Development and intensification of the broad background seen in Fig. 3.4(a) is gauged by monitoring the intensity variation at $\Delta K = \sim 3.4$ Å^{-1}, (a). Finally, a set of TOF measurements, (b), were performed at $\Delta K = 2.25$ Å^{-1} (at an angular position located between the 4/5th and the first order diffraction peaks) by employing a helium beam at an energy $E_i = 31.2$ meV.

The nature of scattering event(s) which yields this background development across all reciprocal space is investigated with TOF-HAS measurements as well. For this purpose, the polar angle of the sample is fixed at 62.1° which coincides with $\Delta K = 2.25$ Å^{-1}. It is a particular position located between the 4/5th and the first order diffraction peaks. And we

take 4 TOF measurements with increasing CN coverages. The resulting TOF spectra, presented in Fig. 3.5(b), indicates that the main contribution to the developing background of angle resolved HAS patterns is due to the increase of the inelastic multiphonon scattering of helium atoms from the surface. In addition, a diffuse elastic peak sits on top of the broad multiphonon distribution.
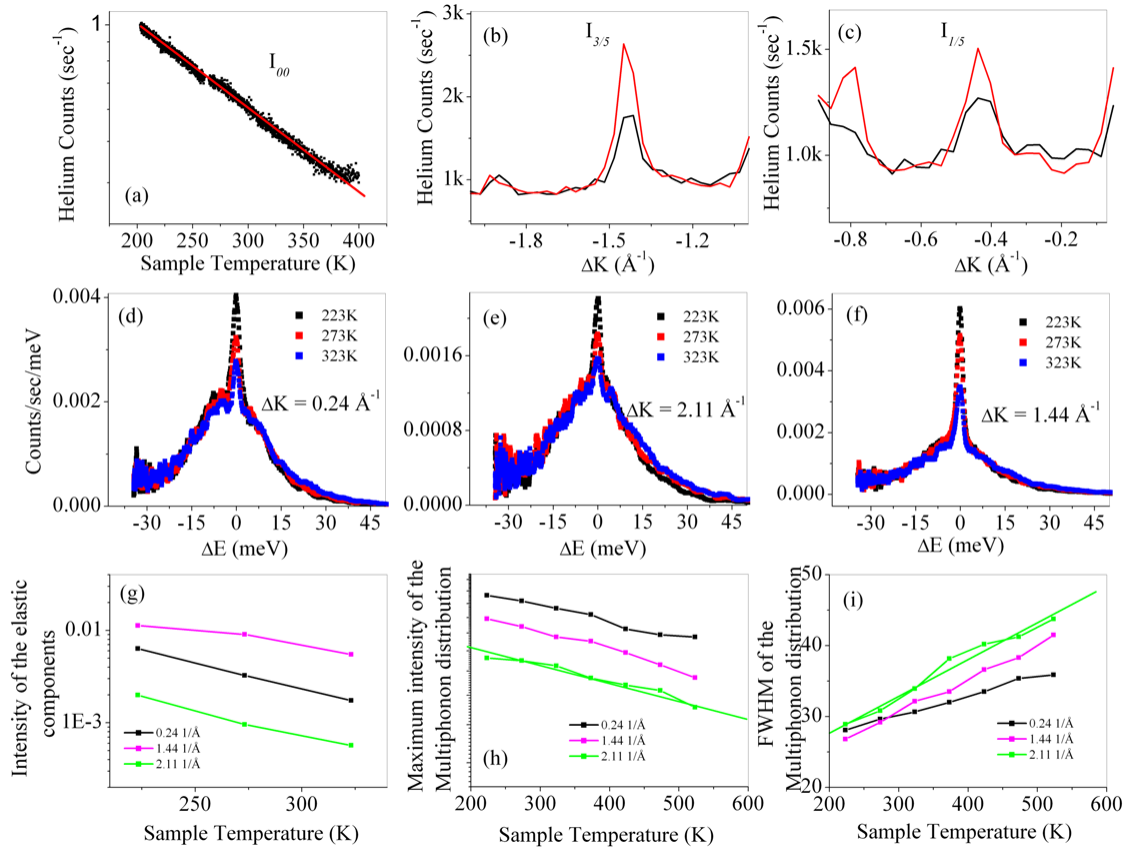
Figure 3.6. Attenuation of the specularly reflected intensity from a saturated CN/Cu(001) surface as a function of increasing sample temperature (a); the temperature effect on the intensities of the 3/5th and of the 1/5th diffraction peaks are also displayed in (b) and (c) respectively. E_i =31.3 meV for the measurements displaced (a)-(c). In addition, TOF measurements (using 47.2 meV helium atoms) were performed at various temperatures while the polar position of the sample is kept at $\Delta K = 0.24$ Å^{-1} (d), at $\Delta K = 2.11$ Å^{-1} (e), and at $\Delta K = 1.44$ Å^{-1} (f) in order to calculate Debye-Waller factors by using the elastic component's intensity attenuation, (g). Finally, variations of the multiphonon distributions' maximum height (h) and the FWHM (i) are presented.

The Debye-Waller factors of He scattering from the saturated CN/Cu(001) surface were calculated by using the sample temperature dependent decays of the specular intensity, I_{00}, (as shown in Fig. 3.6(a)), of the intensity of the $3/5^{th}$ diffraction peak, $I_{3/5}$ (Fig. 3.6(b)) and of the intensity of the $1/5^{th}$ diffraction peak, $I_{1/5}$ (Fig. 3.6(c)). Recalling from Chapter 2, the Debye-Waller factor, 2W, is often assumed to be related to the elastically scattered intensity of helium atoms according to the following relationship:

$$I = I_0 \cdot e^{-2W} \quad \text{where} \quad 2W = \frac{3 \cdot \hbar^2 \cdot \left(\overrightarrow{\Delta k_z}\right)^2 \cdot T_x}{M_s \cdot k_B \cdot \Theta_D^2} \tag{3.1}$$

where $\overrightarrow{\Delta k_z}$ is the momentum change perpendicular to the surface plane experienced by the scattered helium atoms, T_x is the sample temperature, M_s is the mass of a surface moiety from which helium atoms scatter, k_B is the Boltzmann constant and Θ_D is the Debye temperature. The Debye-Waller factors at 263K, found from the data presented in Figs. 3.6(a)-(c), are calculated to be 1.54 for I_{00}, 1.83 for $I_{1/5}$, and 2.1 for $I_{3/5}$, all after background subtractions. The observed increase in 2W with increasing ΔK is tentatively attributed to a finite probability of the helium atom interacting with the longitudinal motion of the surface. This probability is expected to increase with increasing surface roughness, such as results from the addition of a submonolayer density of an adsorbate on a close packed metal face. Using only Eq. (3.1), the Debye temperatures at 263K are found to be 384 K, 351 K and 326 K, respectively.

The following the graphs, Figs. 3.6(d)-(f) display temperature variations of the TOF spectra from saturated CN/Cu(001) surfaces along <110> scattering vector taken when the polar angle of the sample are fixed such that the parallel momentum exchange of detected elastically scattered He atoms are at $\Delta K_e = 0.24$ Å^{-1} (Fig. 3.6(d)), $\Delta K_e = 2.11$ Å^{-1} (Fig. 3.6(e)), and $\Delta K_e = 1.44$ Å^{-1} (Fig. 3.6(f)). The first two ΔK_e positions are located between the diffraction peaks (intentionally avoiding the diffraction peaks), so the elastic component observed in corresponding TOF spectra are only diffuse elastic in nature. On the other hand, the last one, at $\Delta K_e = 1.44$ Å^{-1}, is located exactly where the 3/5th diffraction peak manifests itself in angle resolve HAS patterns. TOFs taken at three temperatures, 223K, 273K and 323K are displayed for the three angular positions. The temperature dependent attenuations of the elastic components' intensities are outlined in Fig. 3.6(g). The Debye-Waller factor at 263K determined from the elastic component's decay at $\Delta K = 1.44$ Å^{-1} (magenta colored curve Fig. 3.6(g)) is 1.89. This number is, as anticipated, close to the 2W(263K) = 2.10 determined by using the $I_{3/5}$ decay in Fig. 3.6(b). The Debye-Waller factors at 263K determined from the diffuse elastic component's decays at $\Delta K = 0.24$ Å^{-1} (black colored curve Fig. 3.6(g)) and at $\Delta K = 2.11$ Å^{-1} (green colored curve Fig. 3.6(g)) are determined to be 3.40 and 3.28, respectively.

The magnitude of the Debye-Waller factor, 2W, is taken as an indication of the average number of phonons interacting with individual scattered particles. [45] As the elastic components of the TOF spectra taken at $\Delta K = 0.24$ Å^{-1} and $\Delta K = 2.11$ Å^{-1} are diffuse in character, this intensity is believed to originate from defects within the ordered c(10x6) superstructure.

The TOF spectra in Fig. 3.5(b) and Figs. 3.6(d)-(f) also clearly demonstrate a continua of backscattered intensities which are often ascribed to multiphonon distributions. There are a number of studies reported [2, 3, 33-41] on how to theoretically address the multi-phonon scattering of helium atoms. Basically, three approximation regimes have been investigated: quantum mechanical, semi classical and classical. The applicability of these regimes is determined by the magnitude of the Debye-Waller factor, 2W. While 2W ≤1 is indicative of a fully quantum mechanical regime (essentially dominated by elastic and single phonon scattering), the classical approach is applicable to systems having 2W >6 [36], and is describes only the characteristics of multiphonon scattering. For our system, CN/Cu(001) at 263 K, the calculated Debye-Waller factors mentioned in previous paragraphs do not approach 6, so the classical modeling would seems inappropriate for our observed multi-phonon distribution. However, when we examine the variations of multiphonon distributions' maximum height and FWHM (presented in Figs. 3.6(h) and 3.6(i), respectively), we shall see that the variations do appear to be in close agreement to predictions of the "discrete model" formulations for the multiphonon distributions in the classical limit.

A "discrete model"'s mathematical representation for the anticipated multi-phonon distribution in classical limit, is expressed as follows: [38, 42]

$$\frac{dR}{d\Omega_f dE_f} \alpha |\tau_{fi}|^2 \left(\frac{\hbar^2 \pi}{\Delta E_0 k_B T_S}\right)^{1/2} \exp\left(-\frac{(\Delta E + \Delta E_0)^2}{4 k_B T_S \Delta E_0}\right) \qquad (3.2)$$

where

$$\left|\tau_{fi}\right|^2 = \exp\left(\frac{\Delta K^2}{Q_c^2}\right)\left(\frac{\hbar^2\beta^2}{4\pi m}\right)^2 pq\sinh(p)\sinh(q)\left(\frac{p^2-q^2}{(\cosh(p)-\cosh(q))^2}\right)^2 \qquad (3.3)$$

$$\text{where} \quad p = 2\pi k'_{iz}/\beta \quad \text{and} \quad q = 2\pi k'_{fz}/\beta \qquad (3.4)$$

$$\text{where} \quad k'_{fz} = \sqrt{k_{fz}^2 + \frac{2m}{\hbar^2}D} \quad \text{and} \quad k'_{iz} = \sqrt{k_{iz}^2 + \frac{2m}{\hbar^2}D} \qquad (3.5)$$

The mathematical formulation of the form factor, $\left|\tau_{fi}\right|^2$ which we use was suggested by Bertino et. al. [3] In these equations, the only free parameters for data fitting are Q_c, β, D and a proportionality constant. ΔE_o represents a recoil energy. Q_c, is known as the "cutoff wave vector", is the inverse of a surface correlation length for inelastic scattering, and carries information about the corrugation of the surface potential along the particular scattering wave vector direction. β is the potential decay factor, where the repulsive potential of the surface–helium atom interaction is given approximately by, $V(z)= exp(-\beta.z)$. D represents the depth of an attractive potential well originating from the attractive Van der Waals interaction between surface and incident helium atoms. k'_{iz} and k'_{fz} are the perpendicular wave vectors of incident and final state helium atoms, respectively, i.e. including a correction for the well depth, D, of the attractive potential. The required proportionality constant carries only instrumental information.

By investigations of these functional forms I have found that each of the fitting parameters, Q_c, β, and D, has distinguishable effects on the anticipated multi phonon distribution. The cutoff parameter, Q_c, dominates positioning of the multiphonon background intensity maximum positions, β affects the broadening of the multiphonon

energy distribution alone, and D introduces asymmetry in the multi-phonon distribution. Except for cases with very small Q_c, the multiphonon distribution has a very weak dispersion throughout the Brillion zone [2]. This conclusion agrees with our experimental observations, i.e. the multi phonon distribution is little affected by changing the polar angle θ, from 35° to 63.5^o (or equivalently changing $-2.5 \text{ Å}^{-1} \leq \Delta K_e \leq +2.5 \text{ Å}^{-1}$). This insensitivity is drastically different from the observations on bare metal surfaces [3, 36], which indicate that the magnitude of Q_c for clean metal surfaces is much smaller than that which will be determined for the CN/Cu(001) surface.

The best fit results for the theoretical form to the TOF measurements performed at two different polar angles, with respect to the saturated CN/Cu(001) sample, are displayed in Fig. 3.7. Theoretically, the magnitudes of $Q_c, \beta,$ and D, as well as the instrumental constant, should have little or no dependence on changing polar angle. The first two rows of Table 3.1 list the optimized $Q_c, \beta,$ and D values for each curve. That fact that very similar results of fitting parameters for the TOF experiments performed at various θ_i values is an excellent indication of the accuracy of our results.
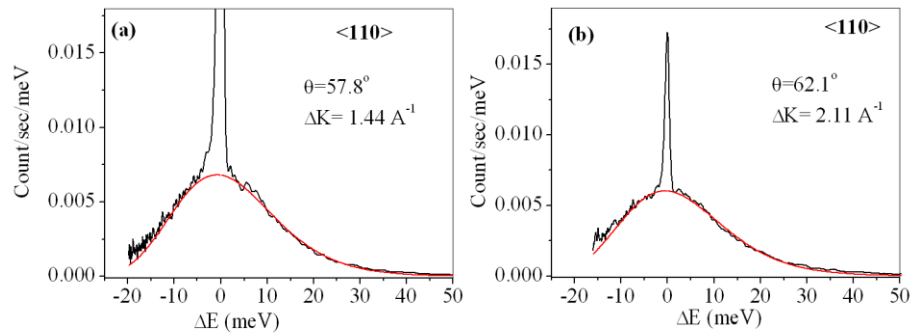
Figure 3.7. Best fit simulation results (red curves) to experimental (black) curves of the multiphonon excitation distributions from saturated CN/Cu(001). (a) at $\theta_i = 57.8^o$ and (b) at $\theta_i = 62.1^o$. $E_i = 31.2$ meV.

Table 3.1					
Sample	Θ_i	Q_c	β	D	Constant
CN/Cu(001)	57.8°	6.08 Å^{-1}	4.49 Å^{-1}	7.72 meV	1.023x10^{-6}
CN/Cu(001)	62.1°	6.14 Å^{-1}	4.47 Å^{-1}	7.66 meV	1.018x10^{-6}
Cu(001) [3]	-	1.0 Å^{-1}	3.0 Å^{-1}	-	-
KCN [2]	-	7.5 Å^{-1}	5.5 Å^{-1}	-	-
Cu(001) [1]	-	-	-	5.7 meV	-

Table 3.1.   Fitting parameters of multiphonon excitation distributions to the discrete model in classical limit and comparisons to some reference surfaces.

The fitting parameters show that the CN/Cu(001) <110> surface has a much higher value of Q_c as well as significant increases in the magnitudes of β and D with respect to the bare Cu(001) surface. The large value of Q_c is the reason behind the small attenuation of multi phonon excitation intensity with increasing parallel momentum transfer; this is indicative of a surface that exhibits a large corrugation amplitude, enabling wide angle helium scattering away from the specular direction. The larger magnitude of β implies that the repulsive surface potential is stiffer, and repulsive interactions are experienced over a shorter range. The increase in magnitude of D for a CN covered surface can be thought as due to a higher polarizability of CN compared to a Cu face. Higher polarizability and higher β values are perhaps at odds with the idea of He scattering from a bound CN$^-$ species with a filled π–like HOMO orbital. Clearly the gas phase picture of the adsorbate species is noticeably modified by the CN's surface interactions.

The quality of the match between the multiphonon distribution and the fitted curves seen in Fig. 3.7 appear, at least visually, better than those given in the literature for the various surfaces with typically 2W>6 regimes [33, 35, 36, 41]. However, the Debye Waller factors we have deduced from coherent elastic intensities are only in the range of 1.39-2.10 for the ordered CN/Cu(001) surface. Those deduced from the incoherent (diffuse) elastic intensities presumed to be largely from defects, are in the range of 3.28-3.40. These Debye-Waller magnitudes are consistently much smaller than 6. This is at first glance totally inconsistent with my successful application of the classical model to describe multiphonon inelastic intensities. A back-scattered HAS intensity distribution showing both measurable coherent diffraction and simultaneously a large "classical" multiphonon intensity component is unprecedented.

To explain this apparent inconsistency we must first consider more fully the nature of substrates that have been investigated in the past and what is fundamentally different in our superstructure. The classical model assumes a scattering center of a certain effective mass. For a copper face that is taken to be the mass of a single Cu atom. In a Sibener group study [43] of neon scattering from 1-decanothiol covered Au(111) surface, the effective mass is found to approach the mass of a methyl group that is exposed on a flexible alkyl chain. In the case of highly dynamic KCN surface [2] the scattering mass used was that of the outer most (largest) anionic CN^- species. Likewise in our simulation we have taken the mass, 26 amu of the molecular anion. The one difference with our surface is that the environments of each CN within the c(6x10) unit cell cannot all be anticipated to be equivalent. In contrast to a c(2x2) superstructure at 0.5 ML for

example, the large unit cell with ~ 0.41ML cannot have each CN adsorbed in the same local environment. The NEXAFS suggested the presence of at least three species within a CN saturated surface.

Hence one can now envisage a CN/Cu(001) surface with differing CN species each exhibiting a range of vibrational characteristics. One "part" of the surface could be vibrationally active. One could consider phase segregation, such as would be observed between phases undergoing a first order transition. Such systems on surfaces can exhibit a lattice gas phase coexisting with an ordered condensed phase. The surface we are investigating is at saturation. Thus the fractional area of 2-D lattice gas would have to be very small if present at all. We can then assume that the c(6x10) phase covers the large majority of the surface.

The vibrationally active "part" of the surface must therefore be found within the c(6x10) phase. And yet the coherent elastic diffraction demonstrates that at least a part of the surface maintains long range order. A possible explanation is to be found in the fact that some of the 13 atoms per unit cell are to be locked in to the long range periodicity. Between an interlocking rigid CN c(6x10) network there can be more frustrated motion of other CN species. If there are many degenerate CN binding positions within a local environment, one can conceive of a highly dynamic CN species with low frequency frustrated vibrational modes. Given the calculational results of CN on Ni(001) [24] differing binding orientations are to be anticipated with low activation barriers, and any frustrated rotational motion can exhibit large amplitudes. In classical terms we are then

describing a certain component of CN's, which are within the overall structure, which would exhibit a high Debye Waller factor. The remaining "part" or component CN's which are required to lock in the locally ordered network would exhibit a lower Debye Waller factor. The more rigid structural component contributes most to the elastic scattering intensity. The more vibrationally active component would contribute most to the multiphonon scattered intensities. In that way we have a surface which appears to exhibits widely varying Debye Waller factors.

In the past, HAS from large superstructures has rarely been considered, nor investigated experimentally. Hence in former studies each and every scattering center was assumed to sit in locally identical environments. Inequivalent sites within large superstructures are of course well appreciated in X-ray diffraction: With careful analysis of coherent diffraction intensities the thermal amplitudes of motion of inequivalent species within a unit cell can be determined. Given the very different nature of the probe- sample interaction, X-ray scattering remains very much in the quantum regime.

3.5.   Conclusion

While C_2N_2 exposures on Cu(001) surface at 173K leads to the deposition of CN and C_2N_2 species simultaneously and yielding a disordered surface, exposures at 263K results in a CN-only surface yielding a ordered superstructure of c(10x6). The superstructure was observed with angle resolved HAS while LEED probing of the same surface shows only a (1x1) pattern. A destructive e-beam effect on adsorbed CN structures would also

explain the lack of reported LEED studies on ordered superstructures formed by CN moieties on any metallic *fcc* (001) or (111) surfaces. Coverage calibrations for CN/Cu(001) suggests that the CN coverage at saturation is about 0.41±0.01 ML, implying 12-13 CN species accommodated within each 30-copper-atom large unit cell. NEXAFS probing of the same surface returns a complicated N 1s-π^* spectrum, implying CN moieties with a number of different binding sites and/or bonding orientations coexisting on the Cu(001) surface. The breakdown of the π^* spectral feature indicates there should be at least three different types of CN moieties on the saturated CN/Cu(001) surface.

This excellent agreement between our data and the classical discrete model of multiphonon scattering implies that some of the CN species in an ordered superstructure have high vibrational amplitudes. The diffuse inelastic intensity is dominated by the most dynamic component of the surface. That fact that sharp superstructure diffraction peaks are observed simultaneously implies that long range order is maintained despite the highly dynamic component. The component that exhibits elastic diffraction moves with comparatively low vibrational amplitudes. The elastically scattered intensity is dominated by the least dynamic CN species of the surface. A set of rigidly placed CN species are expected to build the long range network. The prevailing near static component gives rise to the sharp diffraction peaks. Disorder, or imperfections in the CN network, gives rise to a diffuse elastic intensity fraction.

The above proposal relies on an inhomogeneous set of CN adsorbates. This idea is supported by the fractional saturation coverage in a large unit cell structure. Likewise the NEXAFS results imply the existence of multiple CN species types. Those species are also inclined with respect to the surface normal as might be found for a thermal excitation of large amplitude frustrated rotational modes. In addition, reported low energy barriers for translational and rotational motion of CN moieties on another (001) surface [24] are supportive of low restoring force potential energy surfaces, enabling ready vibrational excitation of frustrated CN translational or rotational modes. A remaining fraction of CN moieties are required to maintain an extensive ordered network. That network serves to induce the observed coherent diffraction peaks.

3.6.   References

[1]   A. Chizmeshya and E. Zaremba, Surface Science 268 (1992) 432.
[2]   S. M. Weera, J. R. Manson, J. Baker, E. S. Gillman, J. J. Hernández, G. G. Bishop, S. A. Safron, and J. G. Skofronick, Physical Review B 52 (1995) 14185.
[3]   M. F. Bertino, J. R. Manson, and W. Silvestri, The Journal of Chemical Physics 108 (1998) 10239.
[4]   L. Guzman, M. Segarra, J.M. Chimenos, P.L. Cabot, and F. Espiell, Electrochimica Acta 44 (1999) 2625.
[5]   F. Ample, D. Curulla, F. Fuster, A. Clotet, and J. M. Ricart, Surface Science 497 (2002) 139.
[6]   M. J. Harrison, D. P. Woodruff, and J. Robinson, Surface Science 600 (2006) 340.
[7]   G. Blyholder, The Journal of Physical Chemistry 68 (1964) 2772.
[8]   C. W. Bauschlicher Jr, Surface Science 154 (1985) 70.
[9]   R. A. Wille, P. P. Netzer, and J. A. D. Matthew, Surface Science 68 (1977) 259.
[10]   M. G. Ramsey, G. Rosina, F. P. Netzer, H. B. Saalfeld, and D. R. Lloyd, Surface Science 218 (1989) 317.
[11]   W. Kirstein, B. Krüger, and F. Thieme, Surface Science 176 (1986) 505.
[12]   F. Solymosi and J. Kiss, Surface Science 108 (1981) 368.
[13]   R. Tero, T. Sasaki, and Y. Iwasawa, Surface Science 448 (2000) 250.
[14]   E. Z. Ciftlikli, E. Y. M. Lee, J. Lallo, S. Rangan, S. D. Senanayake, and B. J. Hinch, Langmuir 26 (2010) 18742.

[15]   H. Conrad, J. Küppers, F. Nitschke, and F. P. Netzer, Chemical Physics Letters 46 (1977) 571.

[16]   W. Daum, F. Dederichs, and J. E. Müller, Physical Review Letters 85 (2000) 2655.

[17]   C. S. Kim and C. Korzeniewski, The Journal of Physical Chemistry 97 (1993) 9784.

[18]   B. Ren, X.-Q. Li, D.-Y. Wu, J.-L. Yao, Y. Xie, and Z.-Q. Tian, Chemical Physics Letters 322 (2000) 561.

[19]   J. Somers, M. E. Kordesch, T. Lindner, H. Conrad, A. M. Bradshaw, and G. P. Williams, Surface Science 188 (1987) L693.

[20]   H. B. Friedrich and P. F. Krause, The Journal of Chemical Physics 59 (1973) 4942.

[21]   K. Kim and W. T. King, The Journal of Chemical Physics 71 (1979) 1967.

[22]   H. Celio and M. Trenary, Physical Review Letters 84 (2000) 4902.

[23]   N. A. Booth, R. Davis, D. P. Woodruff, D. Chrysostomou, T. McCabe, D. R. Lloyd, O. Schaff, V. Fernandez, S. Bau, K. M. Schindler, R. Lindsay, J. T. Hoeft, R. Terborg, P. Baumgärtel, and A. M. Bradshaw, Surface Science 416 (1998) 448.

[24]   H. Yang and J. L. Whitten, Journal of molecular Structure 458 (1999) 131.

[25]   C. Bittencourt, E. A. Soares, and D. P. Woodruff, Surface Science 526 (2003) 33.

[26]   F. P. Netzer, Surface Science 61 (1976) 343.

[27]   L. V. Goncharova, J. Braun, A. V. Ermakov, G. Bishop, D.-M. Smilgies, and B. J. Hinch, Journal of Chemical Physics Vol. 115 No 16 (2001) 7713.

[28]   F. Solymosi and L. Bugyi, Surface Science 147 (1984) 685.

[29]   X. Chen, X. Yang, A. Zhu, C. T. Au, and C. Shi, Journal of Molecular Catalysis A: Chemical 312 (2009) 31.

[30]   S. M. Driver and D. P. Woodruff, Surface Science 492 (2001) 11.

[31]   F. M. Leibsle, S. S. Dhesi, S. D. Barrett, and A. W. Robinson, Surface Science 317 (1994) 309.

[32]   J. Stöhr, ed., NEXAFS Spectroscopy, Springer Series in Surface Sciences, Vol. Vol. 25, Heidelberg, 1992.

[33]   A. Bilic and B. Gumhalter, Physical Review B 52 (1995) 12307.

[34]   B. Gumhalter, Physics Reports 351 (2001) 1.

[35]   B. Gumhalter and A. BiliÄ‡, Surface Science 370 (1997) 47.

[36]   F. Hofmann, J. P. Toennies, and J. R. Manson, Surface Science 349 (1996) L184.

[37]   H. Legge, J. R. Manson, and J. P. Toennies, The Journal of Chemical Physics 110 (1999) 8767.

[38]   J. R. Manson, Physical Review B 43 (1991) 6924.

[39]   J. R. Manson, A. P. Graham, and M. Li, Journal of Physics: Condensed Matter 14 (2002) 6233.

[40]   A. Siber and B. Gumhalter, Surface Science 385 (1997) 270.

[41]   S. M. Weera and J. R. Manson, Nuclear Instruments and Methods in Physics Research Section B: Beam Interactions with Materials and Atoms 96 (1995) 508.

[42]   D. J. Gaspar, A. T. Hanbicki, and S. J. Sibener, The Journal of Chemical Physics 109 (1998) 6947.

[43]   N. Isa, K. D. Gibson, T. Yan, W. Hase, and S. J. Sibener, The Journal of Chemical Physics 120 (2004) 2417.

[44]   F. Hofmann and J. P. Toennies, Chemical Reviews 96 (1996) 1307.
[45]   K. Burke and W. Kohn, Physical Review B 43 (1991) 2477.

Chapter 4

Implementation of new TPD analysis techniques in the evaluation of second order desorption kinetics of cyanogen from Cu(001)

4.1.   Motivation:

In Chapter 3, various experimental techniques were employed to investigate structural characteristics of the CN/Cu(001) surface such as identity of the ordered superstructure, CN densities in these superstructures, as well as evidence for multiple CN binding configurations to the substrate. At the beginning of the study, which will be presented in this chapter, our purpose was to use one of the established Temperature Programmed Desorption (TPD) analysis techniques to examine the desorption spectra from the CN/Cu(001) surface and to determine the activation energy of desorption (E_d), which in the next step can be used to estimate binding energies of adsorbed CN species on the copper.

The desorption event of this investigation, i.e. that of the adsorbed cyanide species ($CN^{\delta-}_{(a)}$) undergoing recombinative desorption evolving molecular cyanogen (C_2N_2) however can not be analyzed correctly with the simplest of traditional analysis techniques. The most common of these techniques often work on the assumption that the value of E_d is independent of CN coverage. Since the adsorbed $CN^{\delta-}$ species are negatively charged, mutually repulsive dipolar interactions are expected to lead to a marked desorption energy reduction with increasing $CN^{\delta-}_{(a)}$ coverages.

The "Complete/Constant Coverage analysis" and "Habenschaden's and Küppers' Leading Edge Analysis" techniques were previously proposed for the surface systems with considerable adsorbate-adsorbate interactions in order to determine E_d $(= E_d^0 + f(\theta))$ values. The latter of these two powerful approaches however require superb signal-to-noise ratios in the data sets. The former requires precise knowledge of surface coverage at any point of the desorption event, repeatability of experimental settings for all experiments as well as superb signal-to-noise ratios. Unfortunately, the quality of our data was not adequate for the application of these two analysis techniques.

In this chapter, we will be reporting a new analysis approach to determine both E_d^0 and the functional form of $f(\theta)$, and which does not necessitate the same superb signal-to-noise ratios in the data. Results derived from the application of this new analysis technique on the desorption curves from CN/Cu(001) surfaces were utilized as initial inputs for a comprehensive curve fit analysis technique. Excellent fits for all experimental desorption curves from CN/Cu(001) surface were produced.

4.2.   Introduction

Cyanogen, C_2N_2, often undergoes dissociative adsorption on metallic faces. The electrophilic adsorbed cyanide radical (CN) readily picks up charge from the surface. The transfer of charge, from surface to isolated CN species, is believed to be up to the order of ~0.7e⁻ /CN on single crystal surfaces [1]. The resultant cyanide anion therefore can be strongly ionically chemisorbed. An advantage of cyanogen as the means of CN

deposition is that only the CN species is deposited. In contrast, for example with HCN exposures, the codeposition of H can potentially lead to other coadsorbed species. [2, 3]

In this study we focus on the high surface temperature desorption of neutral cyanogen from copper (001) to investigate not only CN$^-$/surface binding but also to characterize mutual $CN_{(a)}$-$CN_{(a)}$ interactions. Through a simple chemical consideration, a CN adsorbate on a conducting surface will pick up a net negative charge. However on the metallic face a marked screening of the ionically bound adsorbate, as is observed in DFT GGA calculations [4], also leads to a dipole localized at each adsorbate. The mutually repulsive interaction of surface dipoles is, of course, coverage dependent; i.e. the binding energy of any one ionically bound moiety should decrease with increasing coverage. While the activation energy of desorption increases with decreasing surface coverage, the exact dependence of activation energies on surface coverage is not easily predicted. Surface mobilities, the relative binding and interaction energies, as well as the extent of depolarization at higher coverages all play roles in determining the exact coverage dependence of thermal desorption energies. This adsorption system, however, is one in which one would predict a moderate to strong coverage dependence of thermal desorption energies which has been used to test the new Temperature Programmed Desorption (TPD) analysis techniques introduced here.

TPD is a commonly used technique in the evaluation of the kinetics of gas evolving surface reactions [5]. TPD spectra are taken during a thermal ramp of the surface

temperature. Results from TPD are then usually interpreted in terms of the Arrhenius equation which, in this application, is also known as the Polanyi-Wigner equation:

$$I(T) = -\frac{d\theta}{dT} = -\frac{1}{\beta}\frac{d\theta}{dt} = \frac{\nu\theta^n}{\beta}\exp\left[-E_d\Big/RT\right] \tag{4.1}$$

The desorption rate, I, can be defined in terms of the instantaneous surface temperature, T, and the fractional adsorbate coverage (normalized to that of saturation coverage), θ. ν is the pre-exponential factor of desorption, n the order of desorption, E_d the activation energy of desorption, β the temperature ramp rate (in Ks^{-1}), and R the gas constant. Given the use of the normalized coverage, θ, $0 < \theta \leq 1$, I is expressed in units of inverse temperature (K^{-1}), or strictly in fractional coverage per unit temperature, and ν in inverse time (s^{-1}). In this CN/Cu(001) surface adsorbate system the saturation coverage has been determined with XPS to be 0.41 ML (See Chapter 3 for the coverage calibration of the CN/Cu(001) surface). It is often assumed that ν, n, and E_d are close to coverage independent. Here we have taken $n \sim 2$, and ν and E_d are to be evaluated. From TPD curve shapes, for C_2N_2 from Cu(001), we show that E_d is *not* independent of coverage and that this dependence has implications regarding the applicability of various means for TPD spectra analysis.

After an experimental section the remainder of this chapter is divided into four parts. The first part (Section 4.4.1) reviews X-ray photo-emission data from surfaces prepared by cyanogen exposures of Cu(001) at differing surface temperatures. The thermal stabilities of $C_2N_{2(a)}$ and $CN_{(a)}$ are investigated. The second part (Section 4.4.2) briefly reviews results achieved with various conventional analysis methods for interpretation of TPD

data according to the Polanyi-Wigner equation. Comparative evaluations of major TPD analysis techniques can be found also for example in articles published by the groups of Niemantsverdriet [6, 7] and Yates [8]. In practice the large majority of comparative studies have focused on first order (unimolecular) desorption with far fewer looking at the kinetics of bimolecular processes leading to desorption[9]. This chapter focuses on a near second-order desorption process, for which we show that four existing analysis techniques (Redhead's Peak Maximum method [10], "Arrhenius" plots [6], Complete/Constant Coverage analysis [11], and Habenschaden's and Küppers' Leading Edge Analysis [6, 7, 12]) can suffer either from a neglect of the effects of mutual interactions between surface moieties or from possible poor signal to noise ratios of experimental data. In the third part (Section 4.4.3), we illustrate that desorption peak shapes for a second order desorption mechanism are clearly sensitive to the variation of E_d with instantaneous coverage. In a new approach we show how the increasing initial CN coverage dependence of TPD peak asymmetry indicates that the C_2N_2 desorption activation energies vary linearly with coverage. Independently we also show that T_m, θ_m, and I_m for desorption curves, with varying θ_0, alone allow not only qualitative but also moderately accurate quantitative determination of E_d^o and its coverage dependence. Finally, the fourth part (Section 4.4.4) uses the deduced functional form for $E_d(\theta)$ in application of a systematic curve fit analysis, in this case in the study of the coverage dependent second order desorption process of C_2N_2.

4.3.   Experimental

Temperature Program Desorption experiments were performed in a UHV system, located at Rutgers, with a UTI quadrupole mass spectrometer at a background pressure of $\sim 3 \times 10^{-10}$ mbar. Dosing was achieved by backfilling the chamber with the same "99%" cyanogen (C_2N_2) (Linde Gas) gas source as used for the NSLS experiments. The mass spectra exhibited no observable contaminant levels in the C_2N_2 feed with mass spectrometry. Surface coverages were estimated from integrated peak areas of subsequent TPD spectra, normalized to that evolved from a 0.41 ML C_2N_2 saturated surface. The instantaneous surface coverages were also estimated from remaining integrated peak areas in any particular TPD run. Unfortunately, the TPD runs shown in this chapter could not be allowed to run until desorption was complete, to avoid the possibility of approaching the substrate melting temperature. Runs did not exceed 890K. Even at 3 K s^{-1}, the desorption runs were incomplete. In practice the final TPD sections were estimated using best fitted TPD fit parameters, in order to determine most accurately the initial CN surface coverages. After the determination of each initial coverage, the generated segment of a TPD curve is thereafter disregarded. A circular use of coverage estimates, E_d evaluation, and repeated coverage estimation showed excellent consistency. Absolute coverage estimates are considered to be accurate to within less than ~ 0.02 ML. Lastly, the sample temperature ramps were not exactly linear at the extremes of the thermal ramp regions. Possible effects of non linearity in temperature ramps are discussed below.

Experimental setup and the settings employed for the XPS measurements have been already detailed in Section 3.3.

4.4. Results and Discussion

4.4.1 The thermal stability of adsorbed cyanide probed with XPS

XPS was first used to characterize adsorbed species after C_2N_2 exposures at 173 K and 263 K on the Cu(001) surface. The corresponding C 1*s* and N 1*s* XPS spectra are shown in Figs. 4.1(a) and 4.1(b) respectively, in black for an adsorption and measurement substrate temperatures of 263K and in red for temperatures of 173K.
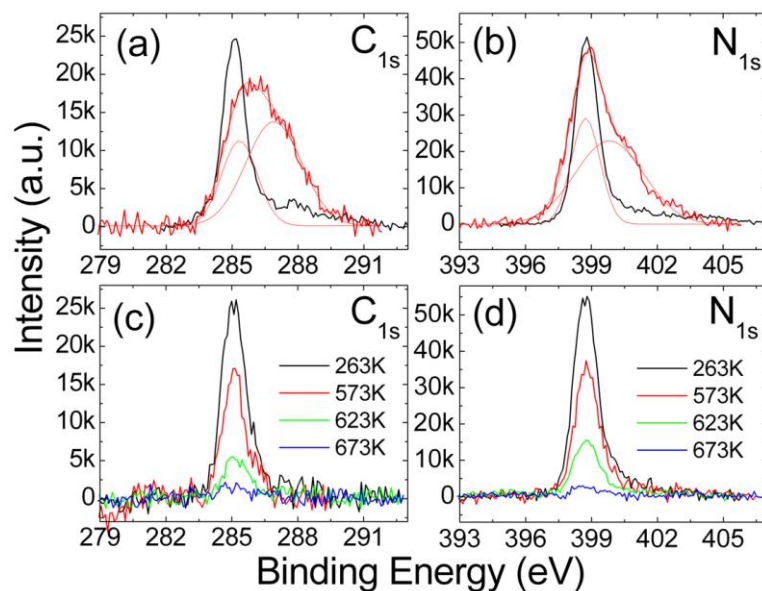
Figure 4.1.   XPS scans of saturation exposures of cyanogen for (a) C 1s and (b) N 1s spectral features. The red curves indicate the results of exposures and measurements made at 173K, whereas the black curves, indicating narrower peaks, are for exposures and measurements at 263K. (c) and (d) exhibit XPS scans at 263K of C 1s and N 1s respectively following 263K saturation and 5 minute anneals up to temperatures, 573K, 623K and 673K, each showing successively smaller surface concentrations.

For exposures at 173K, the N $1s$ region shows a multicomponent spectrum, which can be decomposed into two peaks centered at 398.7 eV and 399.8 eV. Likewise, the C 1s XPS spectrum for this temperature comprises at least two peaks centered at 285.3 eV and 286.9 eV. In contrast, cyanogen deposition at 263K leads to the appearance of the low binding energy peaks alone, both in the C $1s$ and N $1s$ regions. I.e. single C $1s$ (at 285.1 eV) and N $1s$ (at 398.8 eV) peaks are observed in Figs. 4.1(a) and 4.1(b) respectively. The results suggest that for cyanogen deposited at 173K more than one species are present on the surface. For the same exposure the 173K scans show a 55% increase in both total C and N levels, over that for the 263K exposures, in Figs. 4.1(a) and 4.1(b). A molecular cyanogen species, in multilayer adsorption is anticipated. At 263K deposition, the spectra are attributable to essentially only one adsorbed CN^- species. This dissociative behavior is analogous to that of halogens where a diatomic molecule cracks on the surface at room temperature to form only the anionic species [13, 14].

XPS was also used to investigate the surface after complete and partial desorption of C_2N_2. Between 263K and 473K no changes are observed in the C $1s$ or N $1s$ regions. Incomplete desorption is observed following 5 minute temperature anneals to 573K and 623K, as displayed in Figs. 4.1(c) and 4.1(d). In these annealing cycles the C and N losses are in proportion to the original (presumably 1:1) levels, consistent with solely C_2N_2 desorption. After annealing to 673K virtually complete desorption is indicated, and there is little sign of any other residual components such as might be anticipated with $C_{(a)}$ or $N_{(a)}$ species. The latter (spectrum not shown here) exhibits a 397.2 eV feature.

The cyanogen exposures, prior to all TPD experiments, were performed at room temperature. The XPS results above therefore imply that molecular cyanogen is not on the surface at the outset of temperature ramps. Complete dissociation on adsorption is fully supported. The observed molecular desorbing species is therefore formed at temperatures above RT. Our belief is that molecular association is rate determining in the TPD scans of Fig. 4.2 below. Molecular desorption is facile; it occurs readily between 163 and 263K. Fig. 4.2 also indicates that decreasing levels of initial CN coverage, θ_0, results in corresponding shifts to higher desorption temperatures.
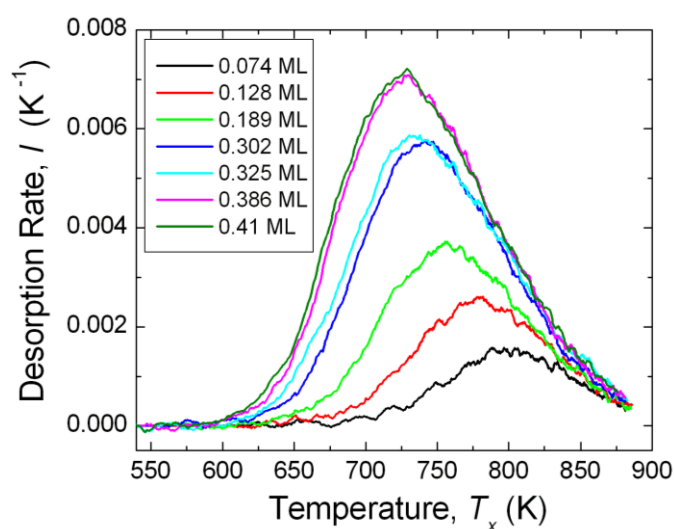
Figure 4.2.   Raw TPD experimental data for cyanogen desorption with varying initial cyanogen coverages. The $m/z = 52$ peak is monitored as representative of the desorbing molecular C_2N_2.

This behavior is anticipated for second order desorption kinetics in associative desorption. Hereafter the following analysis methods, employed to find of desorption energy and pre-exponential factor estimates, will assume that the desorption order n of

Eq. (4.1) equals 2. This comparatively simple associative desorption process is in contrast to what is seen after some halogen exposures. For example, a chlorine exposed Cu(001) surface will exhibit sublimation of bulk CuCl species at temperatures ~ 500K and 900K.[15] No such Cu containing species were seen to desorb with C_2N_2 exposures and the TPD runs.

4.4.2. Application of four established TPD analysis techniques:

The Redhead's Peak Maximum Method [10] derives from differentiation of the Wigner-Polanyi Equation, Eq. (4.1). The technique would also assume model second order behavior with a coverage independent desorption energy E_d. The fact that, at the temperature of maximum desorption, T_m, the derivative dI/dT is zero implies

$$\frac{E_d}{RT_m^2} = \frac{2.\nu.\theta_m}{\beta} \exp\left(-\frac{E_d}{RT_m}\right) = \frac{2I_m}{\theta_m} \qquad (4.2)$$

where θ_m is the instantaneous fractional coverage of the surface at T_m. A plot of $ln(2\theta_m T_m^2)$ vs. $1/T_m$ therefore should show a slope equal to E_d/R and an intercept, $ln(\beta E_d /\nu R)$. Fig. 4.3(a) shows this plot for the data of Fig. 4.2, and a fitted straight line. Using a best averaged value for $\beta = 3.0$ Ks^{-1}, values of $E_d = 102.7$ kJ/mol and a pre-exponential factor of 1.45 x 10^6 s^1 were deduced. Using these E_d and ν values, simulated TPD spectra are illustrated in Fig. 4.3(b). Note: in evaluating the simulated data sets the experimental temperature ramps were utilized. (Constant β values were not assumed.)
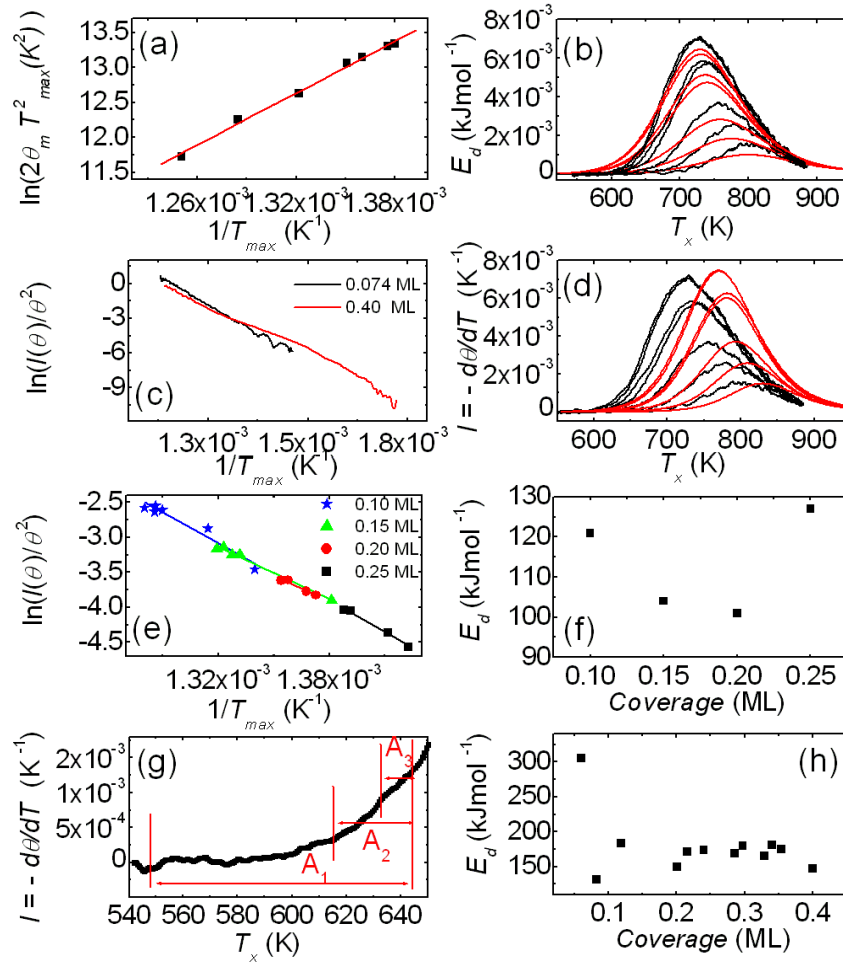
Figure 4.3. Key stages in application of four conventional TPD analysis methods: (a) A $\ln(2\,\theta_m\,T_m^2)$ *vs.* $1/T_m$ plot for seven individual TPD runs at varying initial coverages, derived with Redhead's Peak Maximum method. A best fit straight line is shown in red. (b) TPD spectra (black) and corresponding simulated spectra (red and noise free) derived from Fig. 4.3(a), using 102.7 kJ/mol and 1.45 x 10^6 s^{-1}. (c) Representative Arrhenius plots of $\ln(I/\theta^2)$ *vs.* $1/T$ for the highest and lowest initial CN coverages studied. (d) The TPD experimental data (black) along with the generated curve fits (red) utilizing desorption energy values $\overline{E_d(\theta_0)}$ derived from straight line fits to Arrhenius curves of seven TPD spectra. (e) Plots of $\ln(I/\theta^2)$ vs. $1/T$ at discrete 0.25 ML, 0.20 ML, 0.15 ML and 0.1 ML instantaneous coverages in constant coverage analyses. (f) E_d values deduced from Fig. 4.3(e) at the given four coverages. (g) Three intervals near the onset of an example TPD spectrum used in a modified Habenschaden's and Küppers' leading edge analysis. A_1, A_2 and A_3, are chosen such that the integrated areas under the TPD curve segment of interest, are equal to 0.020 θ_0, 0.015 θ_0 and 0.010 θ_0, respectively. θ_0 is the initial coverage of CN species. (h) Twelve E_d values found by employing the leading edge analysis performed within the A_3 segments, as illustrated in Fig. 4.3(g).

Although the simulated curves derived from the Redhead peak maximum method exhibit matching T_m positions for each desorption curve, they show poor reproduction of the experimental peak widths. Another prominent difference between the experimental data and the generated curves of Fig. 4.3(b) is seen in the asymmetry of the desorption peaks. The generated peaks are highly symmetrical about T_m's but the experimental data show distinctly asymmetric peak shapes. This asymmetry most likely results from the fact that realistically, for cyanogen, the desorption energy is not coverage independent. Indeed this deviation from model second order desorption leads to highly inaccurate results when using this analysis technique. The results reflect the fact that the Redhead model is not suitable for a nonideal second-order desorption process.

A second conventional method, employing Arrhenius Plots, used here also involves another strict treatment of the Polanyi-Wigner Equation, Eq. (4.1). For associative desorption we again take $n = 2$, and we might assume also that the pre-exponential (ν), temperature ramp (β) and desorption energies (E_d) are constants within a given TPD spectrum. We would then conclude that an Arrhenius plot of $ln(I(\theta)/\theta^2)$ vs. $1/T$, as shown in Fig. 4.3(c) below, would have a gradient $= -E_d/R$ and a slope$=ln(\nu/\beta)$. Fig. 4.3(c) shows the observed behavior in Arrhenius plots for the highest (0.41 ML) and the lowest (0.074 ML) initial CN coverages used in this study. In model second order desorption behavior, the Arrhenius Plots should consist of straight lines, just as is seen for the lower coverage, 0.074ML case. However with increasing initial coverage the curves become increasingly non-linear. At all but the lowest initial coverages, the Arrhenius plots at first indicate a coverage dependent $E_d(\theta)$. (See APPENDIX B: we discuss more fully the

parameters that give rise to curvature in these Arrhenius plots; the local slopes are not simply $E_d(\theta)$ alone.)

An averaged value of $\overline{E_d(\theta_0)}$ has however been determined from linear fits to the Arrhenius curves, for each desorption curves belonging to the surfaces with various initial coverages, θ_o. The so-derived activation energies show a consistent decrease with increasing initial coverages; 0.074 ML (171 kJmol^{-1}), 0.129 ML (161 kJmol^{-1}), 0.189 ML (151 kJmol^{-1}), 0.302 ML (149 kJmol^{-1}), 0.325 ML (144 kJmol^{-1}), 0.386 ML (140 kJmol^{-1}), 0.41 ML (135 kJmol^{-1}). Yet, given the nature of the linear fits of non linear curves, it is reasonable to expect that the $\overline{E_d(\theta_0)}$ estimates for desorption energies are still highly inaccurate at the higher coverages. This is certainly borne out by the still poor comparisons of simulated and experimental higher coverage curves of Fig. 4.3(d).

In contrast to the two techniques discussed above, the Complete/Constant Coverage Analysis was developed to determine not only the magnitude but also the coverage dependence of E_d. [11] Complete/Constant Coverage Analysis again uses a strict interpretation of the Polanyi-Wigner Equation, Eq. (4.1). In this case, $E_d(\theta)$ represents the desorption energy of the surface species at a specific fractional coverage. Taking the natural logarithm of Eq. (4.1):

$$\ln\left(\frac{I}{\theta^n}\right) = \ln\left(\frac{v(\theta)}{\beta}\right) - \frac{E_d(\theta)}{RT}$$

(4.3)

By plotting a set of $ln(I_j(\theta)/\theta^2)$ vs. $1/T$ at any one instantaneous fractional coverage θ, with I_j's taken from the jth of a number of TPD spectra, the resulting slope equals –

$E_d(\theta)/R$ and the intercept equals $ln\,\nu$ - $ln\beta$. Fig. 4.3(e) shows the results of this type of analysis for four accessible constant fractional coverages; namely for fractional coverages θ that are present in more than one of the raw TPD data scans. The instantaneous absolute coverages of 0.1, 0.15, 0.2 and 0.25ML were selected for this analysis. The resulting values of E_d (shown in Fig. 4.3(f)) and ν fluctuated depending on the coverage: 0.1ML (121 kJ/mol, 3.09×10^7 s^{-1}), 0.15ML (104 kJ/mol, 2.13×10^6 s^{-1}), 0.2ML (101 kJ/mol, 1.34×10^6 s^{-1}), and 0.25ML (127 kJ/mol, 9.71×10^7 s^{-1}). Apart from highly fluctuating preexponentials ν, we also found no systematic trend in the activation energy with increasing coverage (Fig. 4.3(f)). The constant coverage method clearly requires accurate estimates of coverage as well as superior signal to noise ratios than are seen in this C_2N_2 desorption data set.

In analogy to the Complete/Constant Coverage Analysis, the leading edge analysis method [12] addresses the coverage dependency of E_d. It is a basic and powerful technique to calculate the activation energy of desorption at given coverages by using the onset of desorption peaks. By differentiation of Eq. (4.3) the following Arrhenius equation is obtained:

$$\frac{\partial \ln\left(I/\theta^n\right)}{\partial\left(1/T\right)} = -\frac{E_d(\theta)}{R} + \left[\frac{1}{\nu(\theta)}\frac{\partial\nu(\theta)}{\partial\theta} - \frac{1}{RT}\frac{\partial E_d(\theta)}{\partial\theta}\right]\frac{\partial\theta}{\partial\left(1/T\right)} - \left(\frac{\partial\ln\left(\beta(T)\right)}{\partial\left(1/T\right)}\right) \quad (4.4)$$

The last term is comparatively small in magnitude, as compared to the other terms, as β is approximately constant. The central terms, in square brackets above, may be finite but their significance become negligible if

$$\frac{\partial \theta}{\partial \left(1/T\right)} = IT^2 \approx 0 \tag{4.5}$$

This holds true if the desorption rate is low, i.e. trivially when $\theta \sim 0$, or when I is small such as at the onset of the desorption peak, i.e. at the leading edge. Then

$$\frac{\partial \ln\left(I/\theta^n\right)}{\partial \left(1/T\right)} \approx -\frac{E_d(\theta)}{R} \tag{4.6}$$

The advantage of this technique is that it returns the value of E_d and it removes any error which can arise from assuming a coverage independent pre-exponential factor. However, being restricted to the onset of the desorption peak (where the desorption signal is weak) a superb signal to noise ratio is required. This is often not an easy criterion to meet and is obviously not met by our data. (Fig. 4.3(g))

Whilst it may seem logical to utilize a region of a spectrum with a naturally high signal to noise ratio (e.g. approaching the peak region), we cannot generally use any peak section reliably, as it is precisely in these regions that θ varies strongly. Namely the assumption $\frac{\partial \theta}{\partial \left(1/T\right)} \approx 0$ is poorest. In practice then a best compromise segment near the onset needs to be chosen, wherein IT^2 is still small and yet the signal to noise ratio is adequate for a reliable analysis. For selection of this segment, the leading edge analysis was repeated with the data points with three different interval lengths, shown in Fig. 4.3(g), where integrated areas under the selected segments are chosen to be $A_1 = 0.020\ \theta_0$, $A_2 = 0.015\ \theta_0$ and $A_3 = 0.010\ \theta_0$, where θ_0 is the initial fractional surface coverage of the CN species. Note, the chosen areas do not all run from the very beginning of the TPD scan.

This truncation of the leading edge region, at the very outset edge, is indeed unconventional. Previous work reported in literature [6, 7, 12] generally investigates the effects of cutting off the higher temperature side of the spectrum solely in order to enhance the accuracy of the $\frac{\partial \theta}{\partial \left(\frac{1}{T} \right)} \approx 0$ assumption. However, the conventional approach is of value only if the signal quality is exceptionally high. The high level of noise in our data at low intensities (as seen in the Fig. 4.3(g)) makes the conventional approach non-viable.

Leading edge analysis was performed on *twelve* desorption spectra, where initial absolute coverages range from 0.06 ML to 0.41 ML. The latter figure, 0.41 ML, with $\theta_o = 1$, corresponds to the saturation coverage of CN/Cu(001) surface. While analysis employing the segments A1 and A2 returned highly and randomly fluctuating results (spread throughout the range from 171 to 322 kJ/mol, not shown here), the analysis employing the segment A_3 relatively consisted E_d values from surfaces with initial coverages ranging from 0.22 ML to 0.35 ML, as shown in Fig. 4.3(h). Only the lowest initial coverage, 0.06ML shows a strong deviation. Otherwise E_d values, within a range of initial coverages from 0.22 ML to 0.35 ML, are at 173±8 kJ/mol. Despite this apparent self consistency within the given range, the derived parameters show too much noise, and simulated desorption curves still do not accurately reproduce the experimental data. Also the coverage dependence is not apparent within the random variation of E_d.

4.4.3. Predicting the functional dependence of the activation energy for desorption.

As summarized in section 4.4.2, for an adsorbate system such as CN/Cu(001), a marked coverage dependence in desorption energies makes determination of the activation energies for desorption virtually impossible using the Arrhenius curves or employing Redhead's Peak Maximum method [10, 16-18]. Although the constant coverage analysis method proposed by King [11] and the leading edge analysis method proposed by Habenschaden et al. [12] appear to be appropriate approaches to calculate $E_d(\theta)$, both techniques have a severe limitation, i.e. superb signal to noise is necessary for the utilization of either technique. With the available quality data set we shall apply another approach, outlined in section 4.4.4, but using additional information that we derive here. Namely we seek to determine the functional dependence of $E_d(\theta)$.

4.4.3.1. Qualitative prediction of the functional form of $E_d(\theta)$ from the FWHM and the asymmetry of the desorption peaks at varying initial coverages.

The nature of adsorbate-adsorbate interactions will be qualitatively characterized by observing the initial coverage dependency of the FWHM of a desorption peak. It is well known that the FWHM of "model" first order desorption peaks do not change with increasing initial coverages, θ_o, while for model second order desorption peaks relatively small yet detectable decreases in the FWHM with increasing initial coverages are apparent, as seen in Fig. 4.4(a). The addition of repulsive adsorbate-adsorbate interactions would reduce $E_d(\theta)$ with increasing coverage. Such interactions are thus

manifest in a tendency to increase the FWHM as a function of initial coverage, for either first or second order desorption peaks. For second order desorption kinetics, therefore, there can be competing effects on the FWHM variation with coverage. The experimental FWHM values from seven TPD spectra are shown in Fig. 4.4(b). It is apparent that the broadening effect of mutually repulsive adsorbate interactions dominates. I.e. although the FWHM is initially constant for low θ_o spectra, a steady-broadening of the desorption curves is manifest with θ_o ranging from 0.128 ML to saturation.
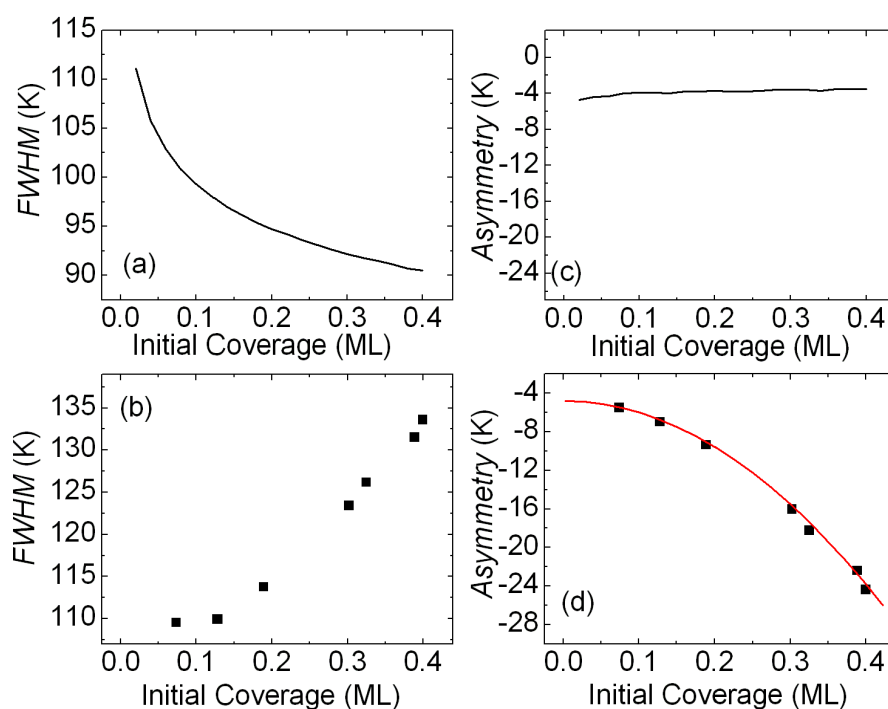
Figure 4.4.   TPD peak FWHM and asymmetry dependencies on initial coverage. (a) FWHM for model second order desorption, generated using $E_d \sim 170$ kJmol^{-1} and $\nu \sim 10^{11}$ sec^{-1}, and (b) experimentally observed FWHM for CN on Cu(001). The peak asymmetry is defined as {HWHM$_{lhs}$ - HWHM$_{rhs}$}. (c) The asymmetry for model second order desorption and (d) experimentally observed asymmetry values. Superposed here is a parabolic curve, $\alpha\ \theta_0^2$, suggesting that $f(\theta)$ varies linearly with coverage. The text discusses further how this deduction is made.

A second key experimental parameter observed is the desorption peak asymmetry, which we define here as {$HWHM_{lhs}$ - $HWHM_{rhs}$}. (HWHM: Half Width at Half Maximum, lhs: left hand side, rhs: right hand side) "Model" second order desorption peaks, where E_d is constant throughout the desorption event, are close to symmetric; the asymmetry of the peak while finite is necessarily only a small fraction of the FWHMs. Simulated spectra show the small asymmetry does not change significantly with θ_o (as illustrated in Fig. 4.4(c)). In contrast, when repulsive forces between adsorbate moieties are present, as in CN/Cu(001), we have observed that the low sample temperature side (lhs) of a TPD peak is considerably steeper than at the higher T_x side (rhs). The observation, that the asymmetry is strongly negative, results from an increasing instantaneous $E_d(\theta)$ as T_x increases and θ simultaneously decreases. Consequently also, a strong variation of asymmetry is also observed as a function of θ_o, as is shown in Fig. 4.4(d).

Let us take $E_d(\theta) = E_d^o$ - $f(\theta)$ where $E_d^o = E_d\left(\theta = 0\right)$ where $f(\theta)$ is as yet a unspecified function of the instantaneous coverage, θ.   Note: the pre-exponential factor, ν of Eq. (4.1), is assumed to be independent of coverage and temperature, which is in accordance with the suggestions of Soler et. al.[19]. The coverage independence of n is also assumed. The two previous paragraphs gave a brief summary of qualitative effects of repulsive adsorbate interactions on the FWHM and asymmetry of the desorption peaks. However, our aim will be to determine $E_d(\theta)$ and ν by applying a curve fitting routine to the experimental data seen in Fig. 4.2. Thus, for the realization of this aim, one key step to be taken first; what is the approximate functional form of $f(\theta)$?

To address this we have utilized a number of independent TPD simulations for a second order desorption process, employing various forms of $f(\theta)$ together with a set of predetermined E_d and ν values, to observe the relationship, if any, between $f(\theta)$ and FWHM(θ_0) as well as between $f(\theta)$ and the TPD peak asymmetry(θ_0). We have observed that, for any "reasonable" functional form of $f(\theta)$, the relationships (7) and (8) below hold well provided $f(\theta)$ and $df(\theta)/d\theta$ are small, i.e. if $f(\theta) \leq E_d^o/10$, and $df(\theta)/d\theta \leq E_d^o/10$. Namely,

$$[FWHM - FWHM_{Model\_2nd\_Order}] \quad \alpha \ \ f(\theta_0) \tag{4.7}$$

and

$$[Asymmetry - Asymmetry_{Model\_2nd\_Order}] \ \approx \ Asymmetry \quad \alpha \quad - [f(\theta_0)]^2 \tag{4.8}$$

where, as before, the TPD peak "$Asymmetry$" is defined as $\{HWHM_{lhs} - HWHM_{rhs}\}$.

The above observations, verified with simulations with predetermined E_d, ν and $f(\theta)$, suggest that the FWHM and the asymmetry of TPD spectra can be used to characterize the functional form of $f(\theta)$. In its current form we do not apply Eq. (4.7) directly as the magnitude of E_d^o is unknown, and hence we cannot immediately subtract the appropriate FWHM$_{Model\_2nd\_Order}$ for use with the experimental data sets.

On the other hand, since the variation in Asymmetry$_{Model\_2nd\_Order}$ is close to zero for the whole range of θ_0, then the magnitude of the variations in the experimentally observed asymmetry can be approximated to be proportional to the square of the $f(\theta)$. The observed "asymmetry" parameter as a function of initial coverage in Fig. 4.4(d) fits well

to a quadratic function of coverage, with zero gradient as θ_0 approaches 0, suggesting that E_d varies approximately linearly with coverage. I.e. for C_2N_2 desorption from the Cu(001) surface,

$$E_d = E_d^o - C\theta \tag{4.9}$$

where the proportionality constant C is yet to be determined.

4.4.3.2. Quantitative determination of $f(\theta)$ from experimentally determined parameters, T_m, θ_m, and I_m.

The second method for predicting the functional form of $f(\theta)$ involves the monitoring of T_m, θ_m, and I_m for TPD peaks associated with varying θ_0. Since $E_d(\theta) = E_d^o - f(\theta)$, the Polanyi-Wigner equation becomes

$$I(T) = \frac{\nu\theta^2}{\beta} \exp\left(-\frac{\left(E_d^0 - f(\theta)\right)}{RT}\right) \tag{4.10}$$

Differentiating both sides of the Eq. (4.10) with respect to T;

$$\frac{dI}{dT} = \frac{\nu\theta}{\beta} \exp\left(-\frac{E_d^0 - f(\theta)}{RT}\right)\left(-2I + \frac{\theta}{RT^2}\left\{\left(\frac{df(\theta)}{dT}\right)T - f(\theta) + E_d^0\right\}\right) \tag{4.11}$$

Using $\dfrac{df(\theta)}{dT} = \dfrac{df(\theta)}{d\theta}\dfrac{d\theta}{dT}$ and that at the desorption peak maximum, the differential in

Eq. (4.11) equates to zero, $\dfrac{dI}{dT} = 0$, at $T = T_m$, $I = I_m$ and $\theta = \theta_m$. This leads to:

$$E_d^0 - f(\theta_m) - \left.\frac{df(\theta)}{d\theta}\right|_{\theta_m} I_m T_m = \frac{2I_m RT_m^2}{\theta_m} \tag{4.12}$$

There are three obvious observations about Eq. (4.12). At first, the equation reduces to Eq. (4.2) in the absence of $f(\theta)$. Secondly, the right hand side of Eq. (4.12) is evaluable from values that can be extracted easily from desorption curves. Thirdly, the magnitudes of both the second and third terms of the left hand side of Eq. (4.12) approach zero in the limit of zero initial coverage, i.e.

$$E_d^0 = \left.\frac{2I_m R T_m^2}{\theta_m}\right|_{\theta_m \to 0} \tag{4.13}$$

Another important property of Eq. (4.12) is that the magnitude of the third term of the left hand side of the Eq. (4.12) is several times larger than that of the second term, i.e. for positive $f(\theta)$,

$$\left(\left.\frac{df(\theta)}{d\theta}\right|_{\theta_m}\right) I_m T_m \gg f\left(\theta_m\right) \tag{4.14}$$

This was borne out by a number of independent simulations with various predetermined E_d^o and $f(\theta)$ combinations and is perhaps not surprising if one looks at the approximately equivalent inequality

$$\left(\left.\frac{df(\theta)}{d\theta}\right|_{\theta_m}\right) \frac{\theta_0}{f\left(\theta_m\right)} \gg \frac{FWHM}{T_m} \tag{4.15}$$

which is derived from Eq. (4.14) by using only $FWHM\ I_m \sim \theta_0$. If $f(\theta)$ takes a form of $\sim \theta^p$ where the exponent $p > 0$, the lhs of Eq (15) $\approx p/2$. As we invariably see $T_m \gg FWHM$ for almost any peak derived from activated desorption, Eq. (4.15) holds true and hence also Eq. (4.14), provided that $\left.\dfrac{d\ln f(\theta)}{d\ln\theta}\right|_{\theta_m} \gtrsim 1$ i.e. unless $p \ll 1$. Thus, incorporating Eqs. (4.13) and (4.14) into Eq. (4.12);

$$-\left(\left.\frac{df\left(\theta\right)}{d\theta}\right|_{\theta_m}\right)I_mT_m \approx \left(\frac{2I_mRT_m^2}{\theta_m}\right)-\left(\left.\frac{2I_mRT_m^2}{\theta_m}\right|_{\theta_m \to 0}\right)=\Delta \qquad (4.16)$$

Note that the right hand side of the Eq. (4.16) can still be evaluated experimentally, however, determination of its second term, which equals E_d^o, is made via an extrapolation. Thus, accuracy of the result obtained depends on the number of TPD measurements with low initial coverages as well as the reliability of their T_m, θ_m, and I_m for each low θ_0 desorption curve.

Finally, rearranging Eq. (4.16);

$$\left(\left.\frac{df\left(\theta\right)}{d\theta}\right|_{\theta_m}\right) \approx -\frac{\Delta}{I_mT_m} \qquad (4.17)$$

Eq. (4.17) suggests that we can determine the approximate functional form of the differential of $f(\theta)$ with respect to θ by using the experimental desorption curves. The differential can then be used to determine the functional form and magnitudes of $f(\theta)$ for θ below or equal to the highest observed θ_m.
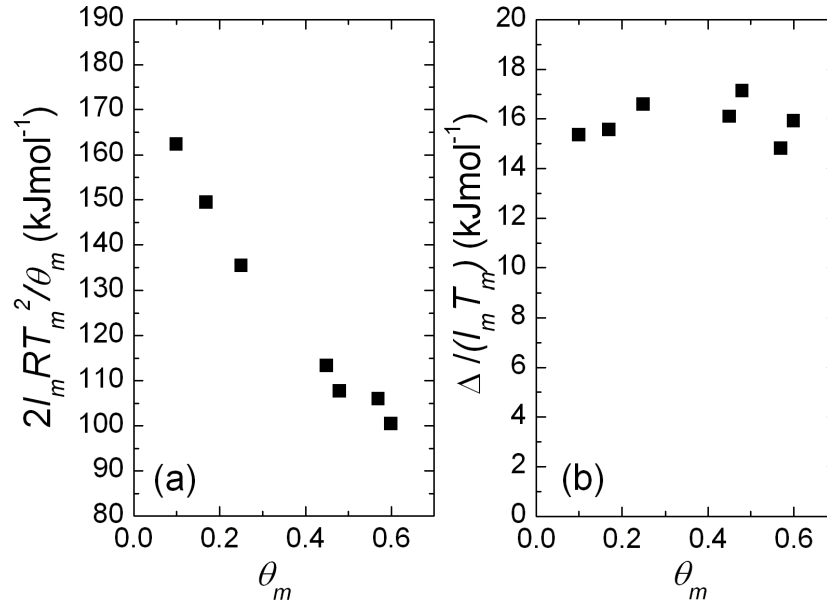
Figure 4.5. (a) Determined values for the right hand side of Eq. (4.12) from the seven TPD curves presented in Fig. 4.2. Extrapolation of these values to zero peak maximum coverage is predicted to yield E_d^o. (b) Values of ($E_d^o/I_mT_m - 2RT_m/\theta_m$) as indicated by Eq. (4.17) for the same TPD curves.

The results of applying this methodology to our TPD spectra are outlined in Fig. 4.5. Fig. 4.5(a) indicates experimentally extracted values of the right hand side of the Eq. (4.12). A simple visual extrapolation of the seven point curve in Fig. 4.5(a) to $\theta_m = 0$ suggests that E_d^o takes at value of approximately 180 kJmol^{-1}. Placing this value into Eq. (4.16) returns the values of Δ. We can thus evaluate the right hand side of Eq. (4.17). The results, shown in Fig. 4.5(b), for the seven desorption spectra, indicate that the differential of $f(\theta)$ with respect to coverage is essentially coverage-independent and floats in the 14-17 kJmol^{-1} range. This result clearly implies that $f(\theta)$ is linearly dependent with θ in the given coverage range. The proportionality constant C is ~15 kJmol^{-1}. This outcome was fully supported by the qualitative conclusion reached in section 4.4.3.1.

4.4.4. Curve fitting method

Utilizing the simple linear functional form for $f(\theta)$, it is now possible to fit most accurately each TPD curve with one kinetic model for desorption. In doing so, we use all data points in a given TPD curve. Explicitly we have run an optimization routine, implemented in Maple 11, for minimization of mean square differences between observed data and simulated desorption runs within the following model:

$$I(T) = \frac{\nu\theta^2}{\beta} \exp\left[-\left(E_d^o - C\theta \right) \middle/ RT \right] \qquad (4.18)$$

The actual temperature ramp rate β, monitored during data acquisition, is used both in displaying $-\dfrac{d\theta}{dT}$ shown in the experimental TPD spectra, and in simulating this data. The assumption of a constant β can lead to considerable inaccuracies in many cases.

In our fitting routine, ν, E_d^o and C are the only free parameters while others are experimentally determined. As is well known, these parameters can be closely coupled [8]. E.g. changes in either E_d or ν can be nearly compensated with variation of the other. A simple fitting procedure of a TPD run can therefore easily return an inaccurate combination of (ν, E_d^o, C). In practice we have found it just as easy to do a systematic search through all parameter space, rather than applying a method of steepest descent. Therefore, we first sample three dimensional (ν, E_d^o, C) space, in small sized steps, and compare the simulated data sets with the experimental TPD scan, taken at any of the six different initial coverage levels ranging from 0.128 ML to 0.41 ML. We chose not to

utilize the TPD curve with the lowest θ_0 only as the signal-to-noise ratio was considered poorer. Then, in a second step, we perform the curve fit searches in the proximity of a number of "good" (ν, E_d^o, C) combinations, which were found through our initial wider 3-D surveys. Thereby we are confident in having finally found the (ν, E_d^o, C) combinations corresponding to the global minima in square error sums. The best fit combinations of (ν, E_d^o, C) for individual TPD runs are listed in Table 4.1.

Initial Coverage	E_d^o (kJ/mol)	ν (s^{-1})	C (kJ/mol)
0.41 ML	177	1.02×10^{11}	14.4
0.386 ML	174	6.2×10^{10}	13.8
0.325 ML	178	9.4×10^{10}	15.2
0.302 ML	176	6.3×10^{10}	14.3
0.189 ML	171	4.7×10^{10}	15.2
0.129 ML	173	5.1×10^{10}	15.5

Table 4.1.   The best fit combinations of (ν, E_d^o, C) for individual TPD runs with indicated θ_0 values.

The results indicate an ~5% uncertainty in zero-coverage activation energy of desorption (E_d^0) for the six desorption curves utilized. The variation in ν just exceeds a factor of two. (An order of magnitude uncertainty in ν is equivalent to ~7.5% uncertainty in E_d. [23]) The extremal variation in C is ~1.4 kJ/mol. which is less than 1% of E_d only. A visual comparison all seven TPD spectra and the corresponding simulations, performed by employing only an average of the fitting results, i.e. E_d^o = 175 kJ/mol, $\nu = 7.0 \times 10^{10}$ s^{-1}

and C = 14.7 kJ/mol alone, is shown in Fig. 4.6. As the fits to the TPD spectra, using this single (v, E_d^o, C) set, are satisfactory for all initial coverages ranging from 0.074 ML to saturation 0.41 ML, the assumed linear relation between the activation energy of desorption and coverage is validated.
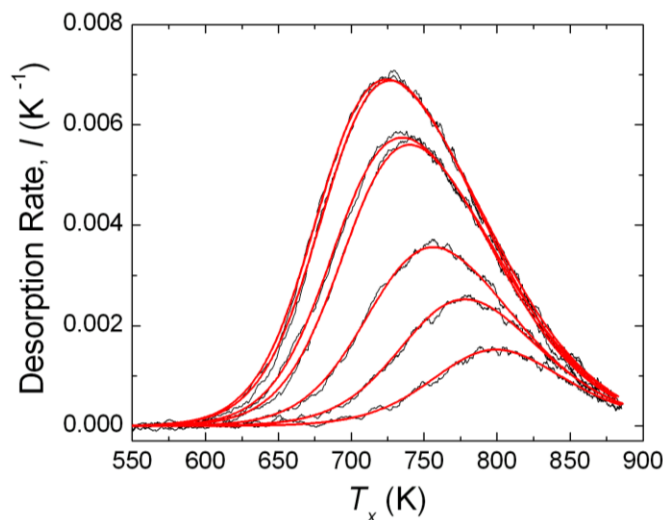
Figure 4.6.   Simulations (smooth red curves) and experimental TPD spectra (noisier black curves). The simulations employed one set of E_d^o = 175 kJ/mol, v = 7.0x10^{10} s^{-1} and C = 14.7 kJ/mol for all seven TPD data sets displayed. The initial coverages of simulated CN/Cu(001) surfaces are ranging from 0.074 ML to 0.41 ML.

4.5.   Conclusions

Part of the challenge of finding realistic values of desorption energy and pre-exponential values is in finding a reliable analysis technique. Four literature techniques (Redhead's Peak Maximum method, the Complete/Constant Coverage analysis, Habenschaden-Küppers/ Leading Edge analysis and "Arrhenius" plots) as well as a fifth technique based on curve fitting have been used to independently estimate the desorption energies and

pre-exponential factors for the recombinative desorption of cyanide to cyanogen on copper (001) surface. It was shown that, due to the anticipated deviation from model second order behavior, the Redhead's Peak Maximum method and "Arrhenius" plots were unsuitable in determining the aforementioned parameters. In the case of the Constant Coverage Analysis, the values obtained for desorption energy and pre-exponential were highly inaccurate and erratic due to this technique's high sensitivity to errors in coverage estimation and its requirement of superb signal to noise quality in the spectra. While a modified Habenschaden-Küppers/ Leading Edge approach analysis suggested a desorption energy in the range of 165 - 181 kJ/mol under the most reliable conditions the technique, however, could not provide systematic results for the coverage dependence of the desorption energy. Only the fifth technique, i.e. determination of functional form of the coverage dependence of E_d followed by the curve fit analysis, provided consistent values of desorption energy in the limit of zero coverage (171-178 kJ/mol) and a pre-exponential ($\sim 7 \times 10^{10}$ s^{-1}) for all the initial CN coverages studied, and this was only obtained when a linear mutual-repulsion factor ($C = \sim 14.7$ kJ/mol) was introduced into the Polanyi-Wigner Equation. In moving from the lowest to the highest CN coverages (0.41ML) the activation energy for desorption was shown to decrease by approximately 8%, namely from 175 to 160 kJmol^{-1}. This fractional variation in E_d we have found is sufficient that neither the Redhead, nor Arrhenius analysis methods could be reliably applied to this desorption system.

Application of the curve fit analysis was possible only after the determination of the functional form of the coverage dependency of E_d. Two different approaches were

introduced here to achieve this prerequisite, both suggesting that the CN coverage dependence of E_d was accurately described by a linear form. Firstly the peak asymmetry, whilst not exactly zero for ideal 2nd order desorption process, exhibits a variation that appears proportional to the square of the initial coverage. Secondly, a novel quantitative technique based upon monitoring T_m, θ_m, and I_m values of TPD spectra with changing θ_0 is in full agreement with the last result.

The latter technique is simple, quantitative, and powerful, but has limitations. Firstly, Eq. (4.17) is useful within a limited coverage range $0 < \theta \leq \theta_m^{sat}$. In other words, we are not able to see whether the functional form of $f(\theta)$ is differing for coverages higher than θ_m^{sat} with respect to that in the range of $0 < \theta \leq \theta_m^{sat}$. Secondly, although the technique returns the value of E_d^o directly, and $f(\theta)$ by integration of the right hand side of Eq. (4.17), the accuracy of the results, especially in determination of E_d^o , depends on the quality of the data, i.e. on the precision of the experimentally obtained parameters, T_m, θ_m, and I_m. Despite these limitations, the accuracy far exceeds that achieved with the 4 conventional methods using our data set without the best of TPD signal to noise ratios. Lastly, $f(\theta) = C\theta$ appears to hold also for $\theta > 0.5$, i.e. for coverages in excess of 0.2 ML up to ~ 0.41 ML, as the simulated curves of Fig. 4.6 fit the data well even for the leading edges of the highest initial coverage TPD curves.

Briefly, Redheads' analysis method has been widely applied, despite its limitations to systems that show only very weak coverage dependent activation energies, essentially

because the analysis requires only knowledge of θ_m, (or even just θ_0) and peak maxima temperatures, T_m, alone. The method is thus popular and very easy to implement even with data sets of comparatively poor signal to noise ratios. However when systems are expected to show coverage dependent desorption energies the method is typically either applied unwisely or not applied at all. We have now illustrated approaches, in sections 4.4.3.1 and 4.4.3.2, which use only one more readily attainable parameter from data sets, namely I_m. We have shown that the new means for estimating $E_d(\theta)$ are both rapid and accurate; the new approaches will be easily applicable in many other adsorption systems.

4.6. References

[1]   J. C. W. Bauschlicher, Surface Science 154 (1985) 70.
[2]   D. Jentz, P. Mills, H. Celio, and M. Trenary, Surface Science 368 (1996) 354.
[3]   H. Celio, P. Mills, D. Jentz, Y. I. Pae, and M. Trenary, Langmuir 1998 (1998) 1379.
[4]   T. Jacob, Unpublished Results
[5]   R. I. Masel, Principles of Adsorption and Reaction on Solid Surfaces, John Wiley and Sons. Inc, New York, 1996.
[6]   A. M. Jong and J. W. Niemantsverdriet, Surface Science 233 (1990) 355.
[7]   D. L. S. Nieskens, A. P. Van Bavel, and J. W. Niemantsverdriet, (2003)
[8]   J. B. Miller, H. R. Siddiqui, S. M. Gates, J. N. Russell, J. J. T. Yates, J.C. Tully, and M. J. Cardillo, Journal of Chemical Physics 87 (1987) 6725.
[9]   A. Fernandez-Ramos, J. A. Miller, S. J. Klippenstein, and D. G. Truhlar, Chemical Reviews 106 (2006) 4518.
[10] P. A. Redhead, Vacuum 12 (1962) 203.
[11] D. A. King, Surface Science 47 (1975) 384.
[12] E. HabenSchaden and J. Kuppers, Surface Science 138 (1984) L147.
[13] Z. T. Stott and H. P. Hughes, Surface Science 126 (1983) 455.
[14] Z. T. Stott and H. P. Hughes, Vacuum 31 (1981) 487.
[15] C. Y. Nakakura, V. M. Phanse, and E. I. Altman, Surface Science 370 (1997) L149.
[16] J. L. Falconer and J. A. Schwarz, Catalysis Reviews: Science and Engineering 25 (1983) 141.
[17] J. D. Edwards, Surface Science 54 (1976) 1.
[18] C. -M. Chan, R. Aris, and W. H. Weinberg, Applications of Surface Science 1 (1978) 360.
[19] J. M. Soler and N. Garcia, Surface Science 124 (1983) 563.

Chapter 5

Bimolecular decarboxylation of NCO species adsorbed on Cu(001)

5.1.   Motivation

NCO has long been recognized by catalysis community as a vital intermediate in reaction processes involving reduction of NO_x species. However, elucidation of the exact nature and chemistry of $NCO_{(a)}$ species adsorbed on real catalyst surfaces and their role played is problematic for a number of reasons. These reasons are generally associated with complications created by a large number of concurrent reactions occurring on real catalysts, complexity of the surfaces and experimental limitations of the probing these real catalyst surfaces. However, performing modeled and carefully choreographed NCO studies on single crystal surfaces rather than real catalysts does not remove all of the complications as a result of NCO's high reactivity towards many other surface species. The most vivid example might be the dissociative adsorption of HNCO on platinum surface followed by brief anneals. This process generates NH, NH_2, NH_3, HCN, H_2O, OH, NO and CO species.

In contrast to the HNCO adsorption on Pt studies, in our studies we prepare an impurity free NCO-only surface by the dissociative adsorption of HNCO on Cu(001) at room temperature, at which $H_{(a)}$ species readily desorb from the surface as H_2 molecules. Having NCO/Cu(001) surface in the absence of other reactants or impurities makes a study of thermally initiated NCO-NCO chemical interactions possible.

5.2.   Introduction

Supported metallic particulates are widely used commercially in reduction of NO_x species in waste streams, and in catalytic converters of incomplete combustion mixtures. Early papers had suggested [1] and confirmed [2, 3] the fact that $NCO_{(a)}$ species, once synthesized on metal surfaces, rapidly spill over to more stable sites on the support. However the comparatively recent discovery of selective catalytic reduction (SCR) of NO_x by hydrocarbons in the presence of excess oxygen on ZSM-5 supported copper surfaces,[4-6] and the subsequent observation of adsorbed $NCO_{(a)}$ species on Cu-Cs/Al_2O_3 during SCR,[7] has since renewed strong interests in $NCO_{(a)}$ and its role as an intermediate in catalytic processes. A positive correlation has been observed between the $NCO_{(a)}$ concentrations on metallic crystallites of SCR catalysts[8], and their efficiency for NO_x reduction to N_2. Since then, an extensive field of research has suggested a wide variety of possible roles for the $NCO_{(a)}$ species during SCR, dependent on the catalyst material, on the hydrocarbons used, and on the presence/absence of water.[9-12]

In parallel, to aid in the development of a better understanding of the $NCO_{(a)}$ species' properties, many studies have since been undertaken on metallic films or single crystal substrates. E.g. NO+CO coadsorption on Pt thin films,[13] on Ru(001),[14, 15] as well as on Pd(111) [16-18] have been investigated. In contrast to other metallic substrates, on copper, $NCO_{(a)}$ formation has not been observed directly with CO+NO coadsorption. Whether $NCO_{(a)}$ is simply not present on copper after CO+NO exposures, or is observable only under high pressure conditions (as in the case of CO+NO adsorption on

Pd(111), [17]) remains an open question. Possible routes for deposition of isocyanates on copper were studied in depth by Solymosi et. al. HCN [19], HNCO [20] and C_2N_2 [21] adsorption on Cu(111), and in the presence of oxygen adatoms and the subsequent thermally initiated reactions, were investigated. These studies established not only the presence of cyanate (-OCN) or isocyanate species (-NCO), but also concluded that at least one of these species is instrumental in formation of $CO_{2(g)}$ and $N_{2(g)}$ at elevated temperatures. XPS studies of $C_2N_2+O_2$, on copper films on graphite, and on copper foil, reached the same conclusions.[22] The cyanate/isocyanate ambiguity was later resolved in favor of an isocyanate species both experimentally [23] and computationally [24, 25] for the Cu(001) substrate.

The motivation of our investigation was to study possible thermally-induced mutual NCO-NCO interactions and to question whether NCO species through bimolecular chemical interactions can lead to a precursor for products desired by both TWC and SCR processes. Employing metal surfaces accommodating NCO species alone is paramount for this investigation in order to avoid competing interactions between NCO species and other moieties. In this context, both the method of NCO generation on the surface and the substrate must be chosen properly. For example, upon C_2N_2 exposures of O/Cu(001) both X-ray photoemission spectroscopy (XPS) and reflection absorption infrared spectroscopy (RAIRS) [22] [23, 26] studies have demonstrated always incomplete $CN_{(a)}$ oxidation to $NCO_{(a)}$; the resulting surfaces must contain $CN_{(a)}$, $NCO_{(a)}$ and $O_{(a)}$ species. Similarly, as indicated in the previous paragraph, the CO and NO interact on other metals and is believed to yield isocyanate and oxygen co-adsorbates. These observations imply

that methods of NCO generation on surfaces through coadsorption are not appropriate to achieve an only-NCO containing surface. A recent study of HNCO dissociative adsorption on Pt(111), resulting in an $H_{(a)}$ and $NCO_{(a)}$ adsorbed surface, and subsequent thermal treatments, probed by TPD and RAIRS,[27] have identified NH, NH_2, NH_3, HCN, H_2O, OH, NO and CO adsorbates. These products explicitly suggest that there can be a number of reactive interactions between $H_{(a)}$ and $NCO_{(a)}$.

A sole NCO adsorbate species can be achieved on Cu through dissociative HNCO adsorption. At RT, spontaneous H_2 desorption leaves a hydrogen free NCO/Cu(001) surface[23] which appears to be a model substrate for studies of possible thermally-induced dissociation of isolated NCO species and/or of mutual NCO-NCO interactions. In this chapter we show XPS, and RAIRS data, which are supportive of a bimolecular decarboxylation reaction of NCO species, yielding $CO_{2(g)}$, and leaving a surface bound carbodiimide (NCN). Previously, a pyrolysis reaction of gas phase HNCO was proposed to produce HNCNH, only at ~1000K and under high pressure conditions[28, 29] This chapter reports on a similar associative reaction, but one that is surface catalyzed, and occurs at temperatures below 573K, and yields a thermally stable adsorbed NCN species.

5.3.   Experimental

Synchrotron X-ray Photoelectron Spectroscopy (XPS) was performed at the Brookhaven National Laboratory NSLS facility on beamline U12A. Details of the experimental settings were already given in the experimental section of Chapter 3. Raw XPS signals are first normalized with respect to the instantaneous photon fluxes. Shirley background subtractions were then performed on the spectra. Resultant spectra were then normalized with respect to the integrated Cu 3p peak intensity. For this purpose, in-situ measurement of Cu 3p peak intensities followed every sequence of C 1s, N 1s and/or O 1s peak measurements. The second normalization, with respect to Cu 3p peak intensities, gives integrated C 1s, N 1s, and O 1s feature signals that are proportional to surface C, N, and O atomic densities. The final coverage calibration is achieved with comparison to reference surfaces, i.e. atomic concentration levels are all relative to ~0.5ML phases [30, 31] formed either by N^+ implantation, or through prolonged O_2 exposures, and anneals, or with respect to a CN c(6x10) phase formed by C_2N_2 exposures alone, which was presented in chapter 3. In cases with overlapping XPS peaks, the spectral features were deconvolved into constituent peaks by using 75% Gaussian + 25% Lorentzian functional forms.

FT-RAIR measurements were taken in the Laboratory of Surface Modification at Rutgers. KBr windows enable a total scattering angle of $>170^o$. A LN_2 cooled HgCdTe detector enables full 980-4000 cm^{-1} band measurements in ~ 30-60 minutes.

In both of the two UHV systems, (base pressures $< 10^{-10}$ mbar) the Cu(001) surface was prepared with cycles of 1keV (>10 µA) Ar^+ or Ne^+ sputtering for 15 minutes, and annealing to 673K for 10 minutes. The initial cleanliness of the sample surfaces was probed either by XPS or raw RAIRS. In XPS, contamination levels fell below the detection limit, i.e. below 1% of a monolayer.

Isocyanic acid (HNCO) was produced by thermal decomposition [32, 33] of cyanuric acid ($(HNCO)_3$, a cyclic trimer of isocyanic acid, Sigma-Aldrich- 99%). Rapid ramping to ~1100K was performed in an pre-evacuated quartz cell, and a mixture of product species was collected in a Pyrex container at liquid nitrogen temperatures. The intermediate mixture predominantly comprises HNCO. CO_2, CO, N_2, H_2 impurities were removed with evacuation at dry ice/acetone bath temperatures for 2-3 minutes. The purified HNCO product was thereafter stored at liquid nitrogen temperatures to avoid any polymerization of HNCO monomers. Detail of HNCO generation process we have set up is extensively described in the APPENDIX C.

The Cu(001) surface was exposed to a HNCO flux from a directional doser present in the XPS chamber. Absolute exposure levels are unknown, although relative exposures were accurately monitored. For the RAIRS experiments, NCO was introduced to the surface through backfilling the chamber with HNCO. In the RAIRS chamber, exposures are reported here in terms of time-integrated non-calibrated ion gauge readings.

5.4. Results and Discussion

The first section here (5.4.1) reports on the identification of pre- annealed $NCO_{(a)}$ vibrational frequencies to be used for reference to RAIR spectra of post- annealed NCO/Cu(001) surfaces. The thermally initiated reactions of NCO species on Cu(001) were deduced, and the post-anneal adsorbed moieties were identified, through soft XPS and RAIRS measurements elaborated upon in the two following sections, (5.4.2 and 5.4.3)

5.4.1. Characterization of the RAIRS bands associated with adsorbed NCO species

The v_a(NCO) IR absorption bands on Cu(001), and their variation as a function of HNCO exposure levels, were investigated with FT-RAIRS. Results are presented in Fig. 5.1. At the lowest level of HNCO exposure, 0.3L, the emergence of two bands at 2158 and ~2190 cm^{-1} is observed, (Fig. 5.1(a).) The absorbances of these two bands grow with increasing HNCO exposures until 6L while their frequencies remain essentially constant, (Figs. 5.1(b)-(d).) At 10L (see Fig. 5.1(e)) a new high-frequency-shoulder of the 2158 cm^{-1} band emerges at ~ 2165 cm^{-1}. Subsequent exposures result in the continual growth of this new feature's intensity as well as the blueshifting of its peak position from 2165 cm^{-1} (Fig. 5.1(e)) to 2225 cm^{-1} (Fig. 5.1(j)). This trend is accompanied by a gradual intensity decrease of the 2158 cm^{-1} band, (Figs. 5.1(e)-(h)) and its eventual disappearance. The band which appeared at low exposure levels at 2190cm^{-1} looks to be gaining intensity up to Fig. 5.1(e) and is eventually overshadowed.
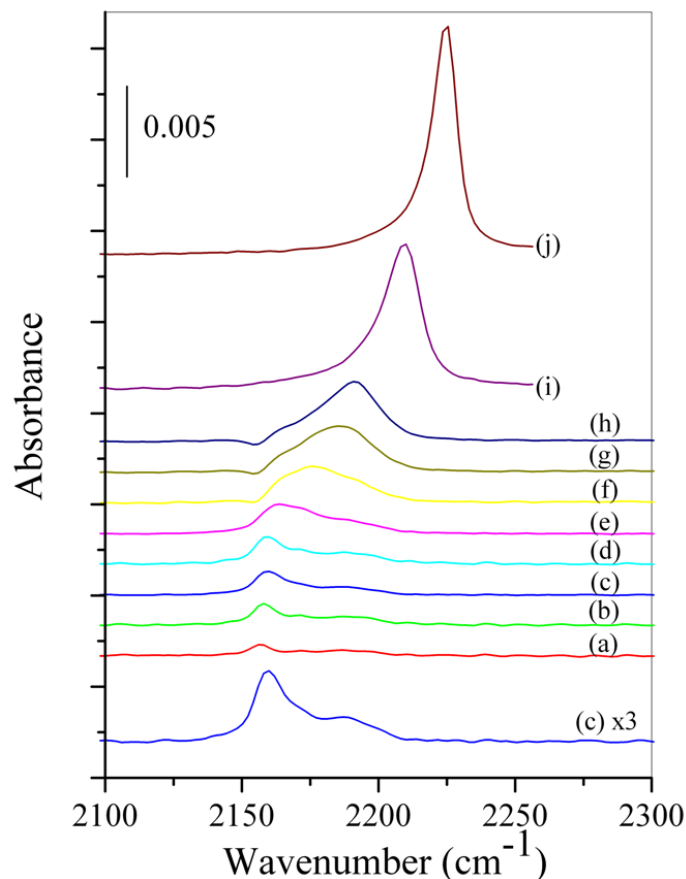
Figure 5.1.   Cu(001) surface RAIR spectra as a function of RT HNCO exposures at (a) 0.3L, (b) 0.6L, (c) 3L, (d) 6L, (e) 10L, (f) 16L, (g) 30L, (h) 66L, (i)150L, and (j) 300L.

It has been demonstrated [23] that $2\delta(NCO)$ and $v_s(NCO)+v_a(NCO)$ bands on the same substrate, have intensities typically below 0.3% of the $v_a(NCO)$ mode intensity. With 30-60 minutes-long measurements, we were able to observe *only* the comparatively intense ~2100-2245 cm^{-1} asymmetric stretch features as shown above.

A preliminary band assignment to the spectra presented in Fig. 5.1 could attribute the bands at 2158 and 2190 cm^{-1}, which exhibit little or no peak shift, to NCO species adsorbed at two different defect site types. The growing, and blue-shifting, band in the 2170-2225 cm^{-1} range would be attributed to the NCO species adsorbed on Cu(001)

terraces. At comparatively small step kink site proportions, anticipated for Cu(001), one could assign the two minority lines to an uphill and a down hill adsorption site with respect to a step edge. In contrast, in previous studies of CO adsorption on Cu(001),[34, 35] only one type of defect site was evident in RAIRS measurements. However, the number of defect adsorption sites may differ for the two adsorbates as CO prefers the "on –top" terrace adsorption site, in contrast to NCO species.

An alternative assignment exists for the lowest frequency band. The frequency of the v_a(NCO)=2158 cm^{-1} band is numerically very close to the v_a(NCO)=2170 cm^{-1} associated with the terrace bound isocyanate species in the low limit of exposure (10L.) We could assign the 2158 cm^{-1} band to isolated NCO species adsorbed on (001) terraces. The shoulder appearing in Fig. 5.1(e) at 2170 cm^{-1} could in turn be due to the first aggregation of small isocyanate clusters. A short range interaction (not necessarily dipolar) can intensify blue-shifted lines with increasing NCO coverage. The large magnitude of the shift, from 2170 cm^{-1} to 2225 cm^{-1} will be attributed to coverage dependent dipole-dipole interactions between NCO species.[36-38] The apparent decrease of the 2158 cm^{-1} band intensity can be in part due to an intensity transfer phenomenon, or to the reducing statistical probability of isolated NCO species at high coverages.

As for the v_a(NCO) mode at ~2190 cm^{-1}, we believe the step edges are the first sites to be filled with NCO species at very low exposure levels. Thus, the observed increase of the 2190 cm^{-1} band intensity up to 16L exposure level (just before it is overshadowed by the

v_a(NCO) associated with NCO species on terraces) can be dominated by the intensity transfer phenomenon [36] alone.

5.4.2. XPS investigation of bimolecular decarboxylation of NCO species at 573K

As previously suggested [39], HNCO adsorbs dissociatively on Cu(001) at RT followed by spontaneous desorption of H_2 at the same temperature. $NCO_{(a)}$ species are seen in XPS with three features, with binding energies at 532.9, 287.7 and 398.9 eV, namely associated with O 1s, C 1s and N 1s features, respectively. Saturation coverage of the NCO/Cu(001) was previously determined to be 0.5 ML [26]. A specific NCO/Cu(001) surface, which would be detailed in this section, was prepared with 900L HNCO exposure at RT. The NCO coverage of the resulting surface found to be 0.384±0.010 ML. Annealing such an NCO/Cu(001) surface to higher temperatures, up to 473K, does not result in any changes in the XPS spectra. (Only with coadsorbed oxygen, a lower temperature NCO oxidation process can be seen at temperatures as low as 373K. [22, 26]) Figs. 5.2(a),(b) and (c) show the 473 K annealed XPS features associated with the molecular NCO/Cu(001). NCO species adsorbed on the copper surface are therefore more stable than isocyanate species adsorbed on more catalytically active metal surfaces, e.g. NCO dissociates to $N_{(a)}$ and $CO_{(a)}$ at 250K on Pt(111) [40], and at 300K on Rh(111) [41] and on Pd(111).[42]

Subsequent annealing of the NCO/Cu(001) surface at 573K however *does* change the XPS spectra tremendously (Figs. 5.2(d),(e) and (f)); (i) the O 1s feature associated with NCO species at 532.9 eV is completely removed from the spectrum 5.2(f). (ii) The C 1s

feature in 5.2(d) is lowered in intensity and is now peaked at 286.4 eV, and (iii) the N 1s

feature preserves its intensity in 5.2(e) while shifting to 398.4 eV. The complete removal

of the 532.9 oxygen feature indicates that the NCO species are eliminated from the

surface during the 573K anneal.
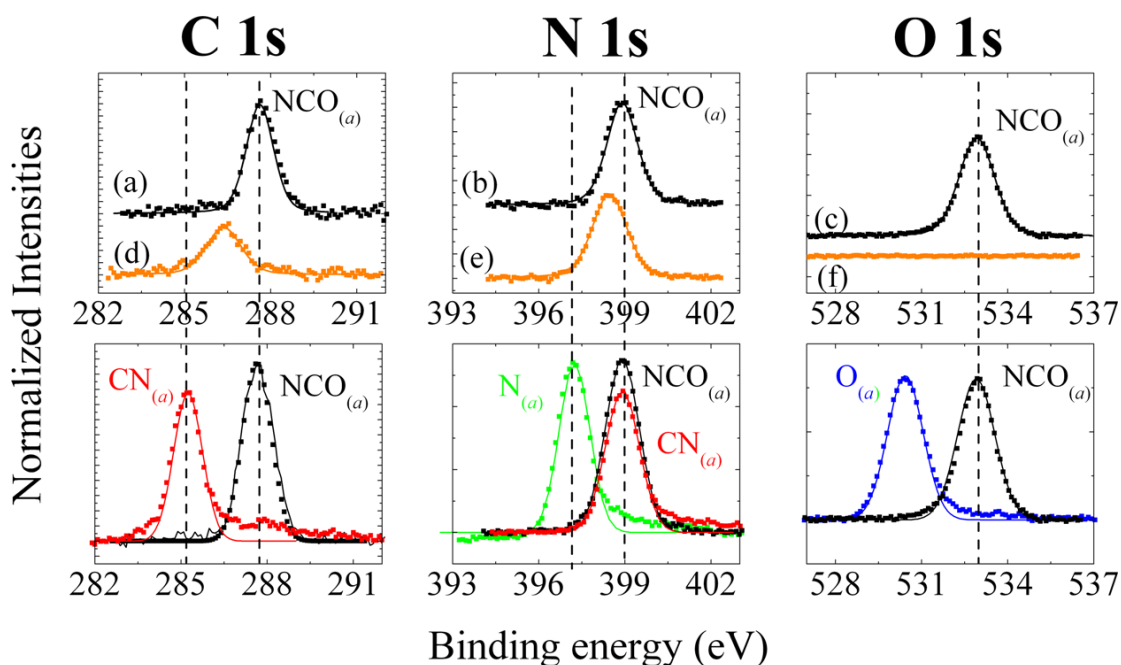
Figure 5.2.   (a) C1s, (b) N1s and (c) O1s XPS features upon RT adsorption of 900L HNCO on Cu(001) followed by a 5min anneal at 473K. No spectral difference is observed between pre- and post- 473K anneal surfaces The same spectral ranges were probed after a subsequent 5 minute anneal at 573K. The results are displayed in (d), (e) and (f). The second row of the plots depicts the XPS spectra from standard reference surfaces for the purpose of both qualitative and quantitative comparisons to Figs. 5.2(a)-(f). These saturated standard surfaces are: 0.5ML O/Cu(001) in blue; 0.5ML N/Cu(001) in green; 0.5ML, NCO/Cu(001) in black; and 0.41ML CN/Cu(001) in red.

BE(eV)	532.9	287.7	398.9	286.4	398.4
Line	O 1s	C 1s	N 1s	C 1s	N 1s
Species	NCO	NCO	NCO	X	X
473K	0.373	0.386	0.385	0	0
573K	0.017	0	0	0.185	0.361
Coverage change (ML)	-0.356	-0.386	-0.385	+0.185	0.361

Table 5.1.   Surface coverages and changes as determined from intensity integration of all XPS features shown in Fig. 5.2. The lowest row of the table indicates the surface coverage variations of chemically discernable moieties observed at RT, after annealing the NCO/Cu(001) surface at 573K

A quantitative analysis of the data presented in Fig. 5.2 is available in Table 5.1. The total population of the nitrogen atoms on the surface is preserved. The new N 1s feature at 398.4 is slightly broader than the N 1s feature of NCO species at 398.9 eV. One half of the initial carbon atom population (0.39 +/-0.01 ML) is removed from the surface. As one half of the carbon atoms are removed from the surface, presumable each carbon atom, leaves in the form of $CO_{2 (g)}$. The remaining carbon "half" is converted to a new C 1s feature at 286.4 eV and this peak position is inconsistent with graphitic carbon, $C_{(a)}$. Likewise the new N 1s feature is 1.2 eV away from an adsorbed atomic $N_{(a)}$ feature otherwise located at 397.2 eV.[26] Also, neither of the new XPS features are aligned with our observations of a $CN_{(a)}$ species at 285.1 and 398.8 eV.[43] These comparisons are also depicted in the second-row plots of Fig. 5.2. The quantitative analysis of the data above implies a reaction of the following stoichiometry;

$$NCO_{(a)} + NCO_{(a)} \xrightarrow{473K<T<573K} CO_{2(g)} + "CN_{2(a)}"$$
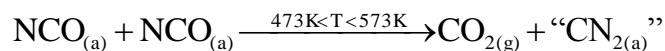
A "bimolecular decarboxylation" of the NCO species, at elevated temperatures and in an oxygen adatom free environment, leaves an implied carbon-nitrogen containing adsorbed species with an empirical formula of CN_2.

5.4.3. RAIRS investigation of the NCO decarboxylation at 573K.

The XPS results of the previous section reveal neither the nature nor the molecular structure of the $(CN_2)_n$ species. The RAIRS experiments, however, give supplementary information on the internal bonding within $(CN_2)_n$ moieties as well as this species' spatial orientation with respect to the Cu(001) surface.
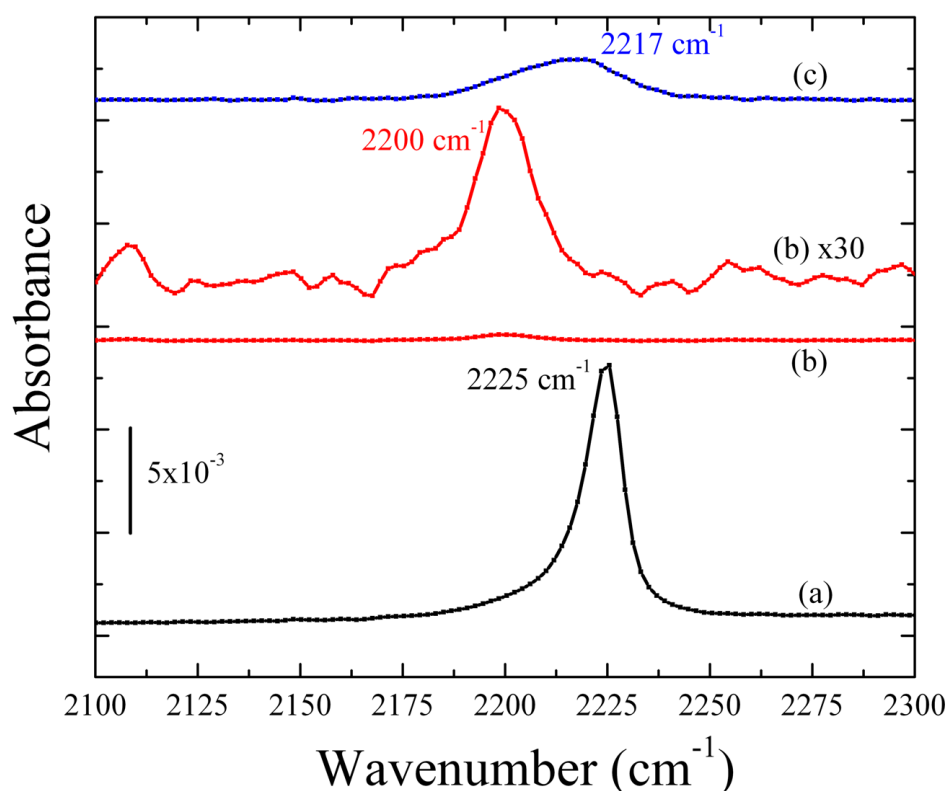
Figure 5.3.   RT FT-RAIR spectra; (a) of a saturated NCO/Cu(001) and (b) after a subsequent 5 min. 573K anneal. The post anneal spectrum is also magnified by a factor of thirty for better visualization of the spectral features. Eventually, 240L O_2 is introduced to the annealed surface, and the resultant unmagnified spectrum is shown in (c.)

Fig. 5.3(a) shows an IR spectrum of the surface immediately after dissociative adsorption of 300L HNCO on Cu(001) at RT. The NCO moieties exhibit the v_a(NCO) mode located at 2225 cm^{-1}. This v_a(NCO) magnitude indicates that the surface coverage of NCO

species should be close to saturation, (0.5 ML). The subsequent annealing at 573K changes this spectral region considerably (Fig. 5.3(b)), leaving a single and weak intensity IR feature located at ~2200 cm^{-1}. This band position and absorbance level is inconsistent with a pure NCO feature alone, as indicated in Fig. 5.1.

When ~240L of O_2 was introduced to the stoichiometrically "CN$_2$" post-anneal surface (Fig. 5.3(c)), it leads to the appearance of a feature at 2217 cm^{-1}, which is considerably more intense than the feature at 2200 cm^{-1} observed in Fig. 5.3(b). We attribute this new feature to the regeneration of NCO species upon oxygen adsorption on the post-annealed surface. Its frequency is higher than expected for a pure NCO peak, yet ν_a(NCO) frequencies are known to increase considerably in the presence of an O coadsorbate. [23]

With which chemical moiety is the 2200 cm^{-1} IR feature associated? Returning back to XPS results outlined in Fig. 5.2, within the detection limits of XPS (~0.01ML), the post-anneal surface does not contain any NCO$_{(a)}$ or CN$_{(a)}$. However, the detection sensitivity of the IR spectroscopy is considerably better than XPS. Therefore, it is hypothetically possible to have very small quantities of NCO$_{(a)}$ or CN$_{(a)}$ on a surface; while they are invisible to XPS they can be visible in the IR spectroscopy. We can quickly dismiss the possibility of an association between the band at 2200 cm^{-1} and isolated CN species in the midst of an "CN$_2$" sea. CN stretching frequencies for both gas phase HCN and HCN adsorbed on Cu(001) are in the narrow range of 2089-2092 cm^{-1} [44]. This frequency range is ~110 cm^{-1} below the 2200 cm^{-1}. A shift in this magnitude cannot be explained by chemical effects imposed by stoichiometrically "CN$_2$" species on any CN species. In

addition, the CN moiety is anticipated to have a very weak IR signature, i.e. a moderate

CN coverage would be required in order to observe a weak v(CN) mode. Lack of XPS

features associated with CN species indicates this is not the case. For the second

hypothetical situation, i.e. isolated $NCO_{(a)}$ species in the midst of a "CN_2" sea, the

frequency gap is ~40 cm^{-1}. To test the hypothesis, we performed an experiment in which

small aliquots of HNCO were introduced to a subsaturated level stoichiometrically "CN_2"

surface. NCO related band frequencies emerging as a result of the introduction of these

small aliquots were very close to those presented in Fig.1 and the band at ~2202 cm^{-1}

remained intact after the HNCO additions
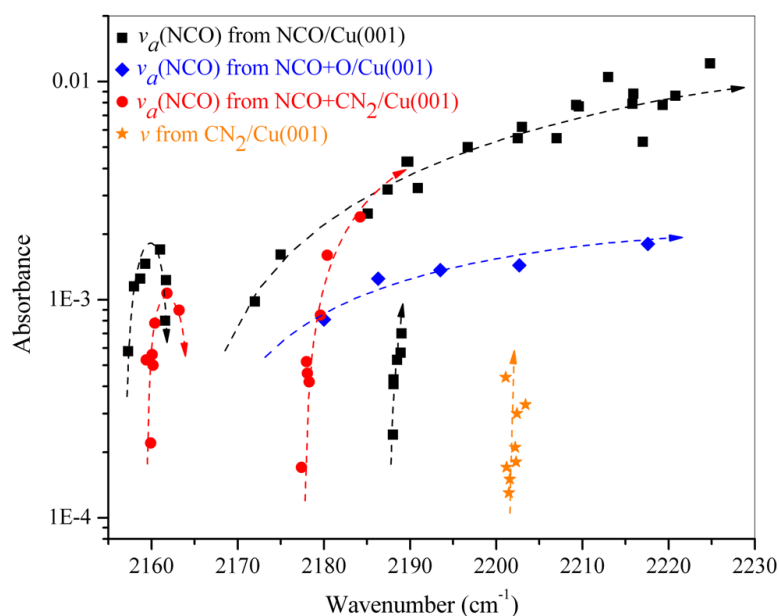
Figure 5.4.   Frequency dependence of observed v_a(NCO) mode absorbance. Accessible v_a(NCO) features are shown for NCO/Cu(001) (black squares), NCO+CN_2/Cu(001) (red dots) and NCO+O/Cu(001) (blue diamond). Absorbance vs frequency data associated with the only detected vibrational mode from CN_2/Cu(001) is shown with orange starred data points. The arrow symbol on each dashed line is indicating the direction that surface coverage of NCO or "CN_2" are increasing.

Absorbance vs. frequency information of all vibrational modes observed from various

NCO/Cu(001), CN_2+NCO/Cu(001), O+NCO/Cu(001) and CN_2/Cu(001) surfaces   are

outlined in Fig. 5.4. Trends of absorbance vs. frequency data points with increasing NCO

or "CN$_2$" coverages are indicated with the dashed lines with arrow. This figure clearly displays ~2202 cm^{-1} peaks (orange star points in Fig. 5.4) associated with the stoichiometrically "CN$_2$" surface moieties adsorbed on Cu(001) cannot be attributed to any type of NCO species we have probed via RAIRS.

Therefore, we conclude that the sole 2200 cm^{-1} band, seen in the spectrum from the post-anneal surface (Fig. 5.3(b)), must therefore be related to the stoichiometrically "CN$_2$" product. Such a small absorbance for a surface concentration as high as 0.25ML from XPS suggests that the "CN$_{2(a)}$" species evidently shows a much lower dynamic dipole moment perpendicular to the surface plane than NCO. In addition, the CN$_{2(a)}$ species on Cu(001) is thermally stable, certainly at 673K, under UHV conditions. Such stability is not to be expected for any CNN species [45]. A literature search of the vibrational modes of N-C-N moieties [46] suggest that only an sp hybridized carbon atom leads to asymmetric stretching modes located somewhere within the 2000-2250 cm^{-1} region. Examples include: *N,N′*-diisopropyl carbodiimide [v_a(NCN)=2215 cm^{-1}], *N*-cyclohexyl-*N′*-(2-morpholinoethyl) carbodiimide , cyanamide [v_a(NCN)= 2230 cm^{-1}]. "sp^2" hybridized candidates, with their stretching frequencies lying far below our observed ~2200 cm^{-1} level, therefore should be dismissed. Finally, the extremely low intensity of the mode located at 2200 cm^{-1}, in spite of the high coverages (~0.25ML) of NCN species, indicates that the dynamic dipole is small in this vibrational mode. Therefore, we attribute this band to the asymmetric stretching of an NCN species (a carbodiimide), which has an ~sp hybridized central carbon atom and with the moiety lying close to parallel to the substrate surface. We envisage a species that is surface bound at both ends.

The chemical environment of two nitrogen atoms of a single NCN moiety can be "slightly" different since (i) the v_a(NCN) mode, though very weak in intensity, is observable with RAIRS and (ii) there is a visible broadening of the N 1s feature observed in Fig. 5.2(b) in comparison to that of Fig. 5.2(a). Another theoretically-visible IR mode associated with this configuration is the bending mode, δ(NCN). Although we cannot independently determine the frequency of such a mode in copper bound species, an IR study of the gas phase HNCNH species shows that the δ(NCN) mode energy is below 500 cm^{-1} [47], which is well below the low frequency limit of our instrument, 980 cm^{-1}.

Gas phase studies have indicated that the HNCNH intermediate is instrumental in HNCO conversion to NH$_3$, HCN, CO and CO$_2$.[28, 29] More recently, the chemistry of cyanamide (H$_2$NCN) (a tautomer of HNCNH) as well as its daughter ions (HNCN$^-$, NCN^{2-}) trapped in a zeolite matrix was also discussed in the context of their role in NO$_x$ reduction.[48]

The structural properties of a polycrystalline copper carbodiimide (Cu^{2+} NCN^{2-}) has been studied comparatively recently [49] as this Cu^{2+} containing salt exhibits unusual magnetic characteristics associated with an unpaired Cu d electron. In this superstructure each N is coordinated most closely to one C (necessarily), and to two most adjacent Cu atoms. In addition, a third interplanar interaction is seen with Cu again. The carbodiimide is believed to be linear, despite a reduced symmetry just as is believed to occur here in the surface phase. On this basis one could argue that the NCN species on Cu(001) sits with N atoms displaced from bridge sites. This supposition however remains to be tested.

5.5. Conclusion

An XPS investigation of the thermal treatment of oxygen free NCO/Cu(001) surfaces, at 573K, shows the appearance of a new C 1s feature at 286.4 eV as well as a new N 1s feature at 398.4 eV binding energies. Quantitative analysis of the XPS data suggests a bimolecular process; two NCO moieties leading to formation of $CO_{2(g)}$ and $CN_{2(a)}$. RAIRS studies suggest that the "CN_2" is a carbodiimide species, i.e. NCN, with a linear "sp" hybridized central carbon atom. The comparative weakness of the v_a(NCN) band, as well as the absence of a v_s(NCN) band, suggest that the surface hosts high concentrations of NCN moieties that lie predominately parallel to the surface plane.

As indicated in section 5.2, the carbodiimide gas, HNCNH, was reported to be produced from $HNCO_{(g)}$ pyrolysis at ~1,000K.[28, 29] On Cu(001) we have shown the production of a surface bound carbodiimide at a much lower temperature. The proposed electron-rich $NCN_{(a)}$ species, with a high thermal stability, which is obtainable at high surface concentrations, could be utilized as an active precursor in chemical modification of copper surfaces. Studies concerning the possible involvement of an NCN species in NCO oxidation mechanisms are also planned.

5.6. References

[1]   R. A. Dalla Betta and M. Shelef, Journal of Molecular Catalysis 1 (1976) 431.
[2]   F. Solymosi and T. Bansagi, The Journal of Physical Chemistry 83 (1979) 552.
[3]   F. Solymosi, L. Völgyesi, and J. Sárkány, Journal of Catalysis 54 (1978) 336.
[4]   W. Held, A. Konig, T. Riher, and L. Ruppe, SAE Paper 900496 (1990)

[5]   M. Iwamoto, Proceedings of the Meeting of Catalytic Technology for Removal of Nitrogen Monoxide, Tokyo (January 1990) pg. 17.

[6]   M. Iwamoto, H. Yahiro, S. Shundo, Y. Yuu, and N. Mizuno, Shokubai (Catalyst) 32 (1990) 430.

[7]   Y. Ukisu, S. Sato, G. Muramatsu, and K. Yoshida, Catalysis Letters 11 (1991) 177.

[8]   Y. Ukisu, S. Sato, A. Abe, and K. Yoshida, Applied Catalysis B: Environmental 2 (1993) 147.

[9]   H. He, J. Wang, Q. Feng, Y. Yu, and K. Yoshida, Applied Catalysis B: Environmental 46 (2003) 365.

[10]   F. Lónyi, J. Valyon, L. Gutierrez, M. A. Ulla, and E. A. Lombardo, Applied Catalysis B: Environmental 73 (2007) 1.

[11]   A. Shichi, T. Hattori, and A. Satsuma, Applied Catalysis B: Environmental 77 (2007) 92.

[12]   F. Zhang, S. Zhang, N. Guan, E. Schreier, M. Richter, R. Eckelt, and R. Fricke, Applied Catalysis B: Environmental 73 (2007) 209.

[13]   J. Raskó and F. Solymosi, Journal of Catalysis 71 (1981) 219.

[14]   K. L. Kostov, P. Jakob, H. Rauscher, and D. Menzel, The Journal of Physical Chemistry 95 (1991) 7785.

[15]   K. L. Kostov, H. Rauscher, and D. Menzel, Surface Science 287-288 (1993) 283.

[16]   C. Hess, E. Ozensoy, and D. W. Goodman, The Journal of Physical Chemistry B 108 (2004) 14181.

[17]   E. Ozensoy, C. Hess, and D. W. Goodman, Journal of the American Chemical Society 124 (2002) 8524.

[18]   F. Solymosi and T. Bánsági, Journal of Catalysis 202 (2001) 205.

[19]   F. Solymosi and A. Berko, Surface Science 122 (1982) 275.

[20]   F. Solymosi and J. Kiss, Surface Science 104 (1981) 181.

[21]   F. Solymosi and J. Kiss, Surface Science 108 (1981) 368.

[22]   A. F. Carley, M. Chinn, and C. R. Parkinson, Surface Science 537 (2003) 64.

[23]   H. Celio, K. Mudalige, P. Mills, and M. Trenary, Surface Science 394 (1997) L168.

[24]   G. R. Garda, R. M. Ferullo, and N. J. Castellani, Surface Science 598 (2005) 57.

[25]   Y. Li, J. M. Hu, Y. F. Zhang, and J. Q. Li, Applied Surface Science 252 (2006) 5636.

[26]   Erkan Z. Ciftlikli, James Lallo, Everett Y.M. Lee, Sylvie Rangan, Sanjaya D. Senanayake, and B. J. Hinch., Journal of Catalysis, in press.

[27]   J. E. Jones and M. Trenary, The Journal of Physical Chemistry C 112 (2008) 20443.

[28]   R. A. Back and J. Childs, Canadian Journal of Chemistry 46 (1968) 1023.

[29]   Y. He, X. Liu, M. C. Lin, and C. F. Melius, International Journal of Chemical Kinetics 23 (1991) 1129.

[30]   F. M. Leibsle, Surface Science 514 (2002) 33.

[31]   M. Wuttig, R. Franchy, and H. Ibach, Surface Science 213 (1989) 103.

[32]   G. Herzberg and C. Reid, Discussions of the Faraday Society 9 (1950) 92.

[33]   M. Linhard, Zeitschrift fuer Anorganische und Allgemeine Chemie 236 (1938) 200.

[34]   K. Horn and J. Pritchard, Surface Science 55 (1976) 701.

[35]   J. Pritchard, T. Catterick, and R. K. Gupta, Surface Science 53 (1975) 1.

[36]   Y. J. Chabal, Surface Science Reports 8 (1988) 211.

[37]   P. Hollins, Surface Science Reports 16 (1992) 51.

[38]   R. Ryberg, Surface Science 114 (1982) 627.

[39]   H. M. Celio, K.; Mills, P.; Trenary, M., Surface Science 394 (1997) L168.

[40]   R. J. Gorte, L. D. Schmidt, and B. A. Sexton, Journal of Catalysis 67 (1981) 387.

[41]   J. Kiss and F. Solymosi, Journal of Catalysis 179 (1998) 277.

[42]   R. Németh, J. Kiss, and F. Solymosi, The Journal of Physical Chemistry C 111 (2007) 1424.

[43]   E. Z. Ciftlikli, E. Y. M. Lee, J. Lallo, S. Rangan, S. D. Senanayake, and B. J. Hinch, Langmuir 26 (2010) 18742.

[44]   H. Celio and M. Trenary, Physical Review Letters 84 (2000) 4902.

[45]   D. E. Milligan and M. E. Jacox, The Journal of Chemical Physics 44 (1966) 2850.

[46]   D. C. Lin-Vien, N.B; Fateley, W.G; Grasselli, J.G. , The Handbook of Infrared and Raman Characteristic Frequencies of Organic Molecules Academic Press, Boston, 1991.

[47]   M. Birk and M. Winnewisser, Chemical Physics Letters 123 (1986) 386.

[48]   Y. H. Yeom, B. Wen, W. M. H. Sachtler, and E. Weitz, The Journal of Physical Chemistry B 108 (2004) 5386.

[49]   X. Liu, R. Dronskowski, R. K. Kremer, M. Ahrens, C. Lee, and M.-H. Whangbo, The Journal of Physical Chemistry C 112 (2008) 11013.

CHAPTER 6

Competing pathways for isocyanate loss from Cu(001)

with co-adsorbed oxygen.

6.1. Motivation

Although NCO has long been recognized as a vital intermediate in reaction processes involving reduction of NO_x species in both three-way catalytic conversion (TWC) and selective catalytic reduction (SCR) mechanisms, its role, properties, and reactions in which it is involved have not been clearly elucidated. Three fundamental reasons for the lack of conclusions are: (i) the complex nature of the heterogeneous catalysts surfaces, (ii) the limitation of the available experimental techniques to study metals deposited on high surface area support materials in powder form, as well as (iii) the complexity of NCO being short-lived, in small quantity and a highly reactive intermediate in the background of many concurrent reactions of a diverse set of chemical moieties happening on the catalyst surface. These limitations and complexities dictate the use of simpler and planar surfaces, with a strict control of reactants, to develop better a understanding of reaction mechanisms and eventually to accomplish the atomic level understanding of the mechanisms.

Among the many plausible reactions proposed for NCO in the literature, two, namely the NCO+NO and NCO+O reactions, are emphasized being reactions steps generating CO_2 and N_2, which are the desired products of both TWC and SCR processes. In this chapter,

we will focus on the NCO+O reaction. There are a large number of studies on NO_x reduction catalyst surfaces in the literature, reporting cyanide ($CN_{(a)}$) species together with $NCO_{(a)}$. We will try to elucidate the role of $CN_{(a)}$ species, if any, in thermally initiated reaction of $NCO_{(a)}$ with $O_{(a)}$. For this purpose, two surfaces, namely NCO+O/Cu(001) and CN+NCO+O/Cu(001) will be prepared and thermally initiated reactions at 473 K on these surfaces will be monitored by using XPS and TPRD techniques.

6.2. Introduction

Adsorbed isocyanate (-NCO) species have been observed following CO+NO exposures of alumina- or silica- supported Pt, Pd, Rh, and Ir metals [1-7] as well as on Ru/SiO_2 [8] and Ni/SiO_2.[9] In these studies, the formation of $NCO_{(a)}$ species was explained via dissociation of $NO_{(a)}$ on crystalline metal particulate surfaces at elevated temperatures followed by the reaction between $CO_{(a)}$ and $N_{(a)}$. The support surface, not the crystalline metal, was first suggested[10] to be eventual binding location of the $NCO_{(a)}$ species Later studies[11, 12] established that the support surface indeed hosts the majority of the $NCO_{(a)}$ species; i.e. $NCO_{(a)}$ species, once synthesized on crystalline metal surfaces, quickly spillover to the binding sites on the support where they are stabilized and immobilized. Unland [6] observed small quantities of $NCO_{(a)}$ species on Ru/Al_2O_3 compared to the other above referenced surfaces. On the basis of this lack of $NCO_{(a)}$ species on the ruthenium catalyst together with the knowledge of a relatively high $NO_{x(a)}$ conversion efficiency to N_2 on Ru/Al_2O_3, it was argued that $NCO_{(a)}$ is an "undesired"

intermediate, which can even lead to counter-productive NH_3 yields in the presence of water. In addition it was argued that, because of, the spillover of $NCO_{(a)}$ from metal surfaces to the support and the eventual occupation of the areas adjacent to the metal particulates, the electronic properties and the catalytic activity of the metal was significantly perturbed by $NCO_{(a)}$ levels.[2] However, it has not been established whether transitory $NCO_{(a)}$ species on metal particulates do or do not play an active role in NO_x reduction mechanisms.[13]

The discovery of selective catalytic reduction (SCR) of NO_x by hydrocarbons in the presence of excess oxygen on ZSM-5 supported copper surfaces,[14-16] and subsequent observation of $NCO_{(a)}$ species on Cu-Cs/Al_2O_3 during the SCR,[17] eventually lead to the intensification of interest in the role played by $NCO_{(a)}$ as an intermediate. Ukisi et al. [18] observed a positive correlation between the formation of $NCO_{(a)}$ species on the catalysts and the efficiency of NO_x reduction to N_2, and concluded that the $NCO_{(a)}$ species produced upon the coadsorption of $NO+O_2+$alkane, (i.e. α-NCO) is different from that formed upon CO+NO coadsorption (i.e. β-NCO) It was postulated that α-NCO is on metallic particulate surfaces (not on the support) and is stabilized by the presence of co-adsorbed oxygen adatoms on the same surfaces. Ukisu [17], and later Takeda [19], suggested that the production of $N_{2(g)}$ and $CO_{2(g)}$ takes place by the reaction of $NO_{(a)}$ with the $NCO_{(a)}$ intermediate. In the last two decades, literally thousands of articles have been published on SCR of NO_x by hydrocarbons with excess oxygen presence on various catalyst surfaces. A wide variety of roles for the $NCO_{(a)}$ species during SCR have been

proposed depending on the catalyst material, hydrocarbons used, and the presence or absence of water. [20-23]

In SCR, the simultaneous oxidation of CO and alkanes and the reduction of NO_x, happens on complex catalysts and through a large number of reactions, which have not yet been fully identified. To aid in developing a better understanding of the nature of $NCO_{(a)}$ species, many studies have been undertaken on films or single crystal substrates, e.g. NO+CO coadsorption on Pt thin films [24], on Ru(001) [25, 26] as well as Pd(111) [27-29] were studied. Kostov et al.[26] established that $NCO_{(a)}$ formation on Ru(001) was "catalyzed" by the presence of co-adsorbed atomic oxygen. Later work established that $NCO_{(a)}$ species are stabilized by co-adsorbed O on Rh(111)[30] and Pd(100).[31] Specifically for copper substrates, $NCO_{(a)}$ formation has not been observed directly for CO+NO coadsorption. $NCO_{(a)}$ was only indirectly implied for an intermediate in the reaction pathway for nitrogen desorption from a NO+CO coadsorption on Cu(111).[32] A more recent study[33] on CO+NO reactions on Cu(001) however does not propose an active $NCO_{(a)}$ species. Whether $NCO_{(a)}$ is simply not present on copper, or its observable only under high pressure conditions (as in the case of CO+NO adsorption on Pd(111) [28]) remains an open question.

HCN [34], HNCO [35] and C_2N_2 [36] adsorption on Cu(111) in the presence of oxygen adatoms and the subsequent thermally initiated reactions were studied in depth by Solymosi et al by using AES, EELS and TPD techniques. These studies clearly establish not only the presence of cyanate (-OCN) or isocyanate species (-NCO) as an

intermediate, but also conclude that these species are instrumental in the formation of $CO_{2(g)}$ and $N_{2(g)}$ at elevated temperatures. XPS studies of $C_2N_2+O_2$, on copper films on graphite, and on copper foil, reached the same conclusions [37]. The cyanate/isocyanate ambiguity was later resolved in favor of an isocyanate species both experimentally [38] and computationally [39, 40] for the Cu(001) substrate. Both XPS [37] and RAIRS [38] studies demonstrates that the $CN_{(a)}$ oxidation to $NCO_{(a)}$ upon C_2N_2 adsorption on O/Cu(001) is only partial. The same conclusion is to be drawn from our experiments with various RT C_2N_2 and O_2 exposure combinations on Cu(001); the resulting surface contains always $CN_{(a)}$, $NCO_{(a)}$ and $O_{(a)}$ species.

In contrast to other metallic substrates, copper supports a thermally stable $NCO_{(a)}$ species. Pure $NCO_{(a)}$ adsorbates on Cu(001) are stable up to at least 473K [41], while they dissociate into $N_{(a)}$ and $CO_{(a)}$ at 250K on Pt(111) [42], and at 300K on Rh(111) [30] and Pd(111) [31]. Although the coadsorbed oxygen increases the stability of $NCO_{(a)}$ species on platinum and rhodium by 60-80K,[30, 31] it does not necessarily hinder the dissociation of $NCO_{(a)}$ at 360-380K. Thus, the copper surface is a suitable substrate for the study $NCO_{(a)}$ oxidation, without a competing dissociation reaction. Also, co-adsorbed hydrogen (upon dissociative adsorption of HNCO on catalytically active metal surfaces) can alter the surface chemistry of $NCO_{(a)}$ species drastically, e.g. TPD and RAIRS [43] studies of HNCO adsorption on Pt(111) identify reaction products of NH, NH_2, NH_3, HCN, H_2O, OH, NO and CO. In contrast, dissociative HNCO adsorption on Cu(001) at RT is followed by H_2 desorption, leaving a hydrogen free NCO/Cu(001)

surface.[38] The absence of atomic hydrogen prevents possible competing interactions of hydrogen with $O_{(a)}$ and/or $NCO_{(a)}$ at elevated temperatures.

In this chapter, we discuss the thermally initiated reactions of NCO+O/Cu(001). If the isocyanate species is prepared by RT HNCO exposure, a following O_2 exposure generates the coadsorbed O + NCO species. In contrast, if the isocyanate species is prepared by RT C_2N_2 and O_2 exposures, then residual $CN_{(a)}$ will always coexist with the O + NCO species on Cu(001). These samples, have been studied with the combination of high resolution soft X-ray photoelectron spectroscopy (E = 650 eV, $\Delta E \sim 1eV$) and temperature programmed reactive desorption (TPRD). This study reports on two competing mechanisms of $NCO_{(a)}$ removal from Cu(001) in the presence of $CN_{(a)}$ and $O_{(a)}$ species.

6.3   Experimental

Temperature Programmed Reactive Desorption (TPRD) experiments were performed in a second UHV system. An apparatus designed primarily for helium atom scattering apparatus, with a base pressure of $1x10^{-10}$ Torr, can employ a monochromatic ($E_i = 31.3$ meV, $\Delta E/E \leq 2\%$) supersonic helium beam.[44] The sample chamber partial pressures are measured with a UTI 100C quadrupole mass spectrometer which is used also for the TPRD studies. The surface temperature was ramped at ~ 3 Ksec^{-1}.

Synchrotron X-ray Photoelectron Spectroscopy (XPS) was performed at the Brookhaven National Laboratory NSLS facility on beamline U12A. Details of the experimental settings were already given in Section 3.3. Details of the XPS data processing and normalizations were described in Section 5.3.

In both of the two UHV systems, (base pressures $< 10^{-10}$mbar) the Cu(001) surface was prepared with cycles of 1keV ($>$10 μA) Ar^+ or Ne^+ sputtering for 15 minutes, and annealing to 673K for 10 minutes. The initial cleanliness of the sample surfaces was probed either by XPS or with He atom reflectivity. In XPS, contamination levels fell below the detection limit, i.e. $\leq$ 1% of a monolayer. The paucity of surface defects was confirmed in He scattering by observation of a room temperature He reflectivity in excess of 20%, which is believed to imply a point defect density of $\leq$ 0.3% of a monolayer.

Isocyanic acid (HNCO) was produced by thermal decomposition [45, 46] of cyanuric acid ($(HNCO)_3$, a cyclic trimer of isocyanic acid, Sigma-Aldrich- 99%). Rapid ramping to ~1100K was performed in an evacuated quartz cell, and a mixture of product species was collected in a Pyrex container at liquid nitrogen temperatures. The intermediate mixture predominantly comprises HNCO. CO_2, CO, N_2, H_2 impurities were removed with evacuation at dry ice/acetone bath temperatures for 2-3 minutes. The purified HNCO product was thereafter stored at liquid nitrogen temperatures to avoid any polymerization of HNCO monomers. Further insight to the process as well as the experimental setup, where the decomposition, purification and storage procedures are performed, is detailed in APPENDIX-C.

Cyanogen (C_2N_2, 99% purity) was supplied by Linde gas. Oxygen (O_2, 99.998% purity) was supplied by Matheson TriGas.

In both UHV systems the Cu(001) surface was exposed to C_2N_2 or to a HNCO flux from directional dosers. Absolute exposure levels are unknown, although relative exposures were accurately monitored within each chamber. O_2 exposures were performed by backfilling the chambers. All exposures are reported here in terms of time integrated ion gauge readings with the UHV chambers.

6.4. Results and Discussion

The chemical composition and surface densities of surface bound moieties were primarily investigated with quantitative XPS measurements. Evidence of surface moieties were sought both preceding and after thermal treatments of surfaces prepared with the coadsorption of HNCO+O_2 and coadsorption of C_2N_2 +O_2. Independently, the desorbing products of the thermally initiated reaction both samples were monitored using RTPD.

6.4.1. Coverage calibrations of NCO/Cu(001) surfaces

Fig. 6.1 shows a selection of XPS spectra following different adsorption processes designed specifically for surface coverage calibration references. The N/Cu(001) surface, prepared by N^+ sputtering (E_i = 1keV, >5000μC) followed by a brief annealing at 600K,

C 1s   **N 1s**   **O 1s**

Normalized Intensities (a.u)

(a) 397.2 N$_{(a)}$

396 399 402 405

(b) 530.6 O$_{(a)}$

528 531 534 537

(c) 287.8 NCO$_{(a)}$

282 285 288 291

(d) 398.8 NCO$_{(a)}$

396 399 402 405

(e) 532.8 NCO$_{(a)}$
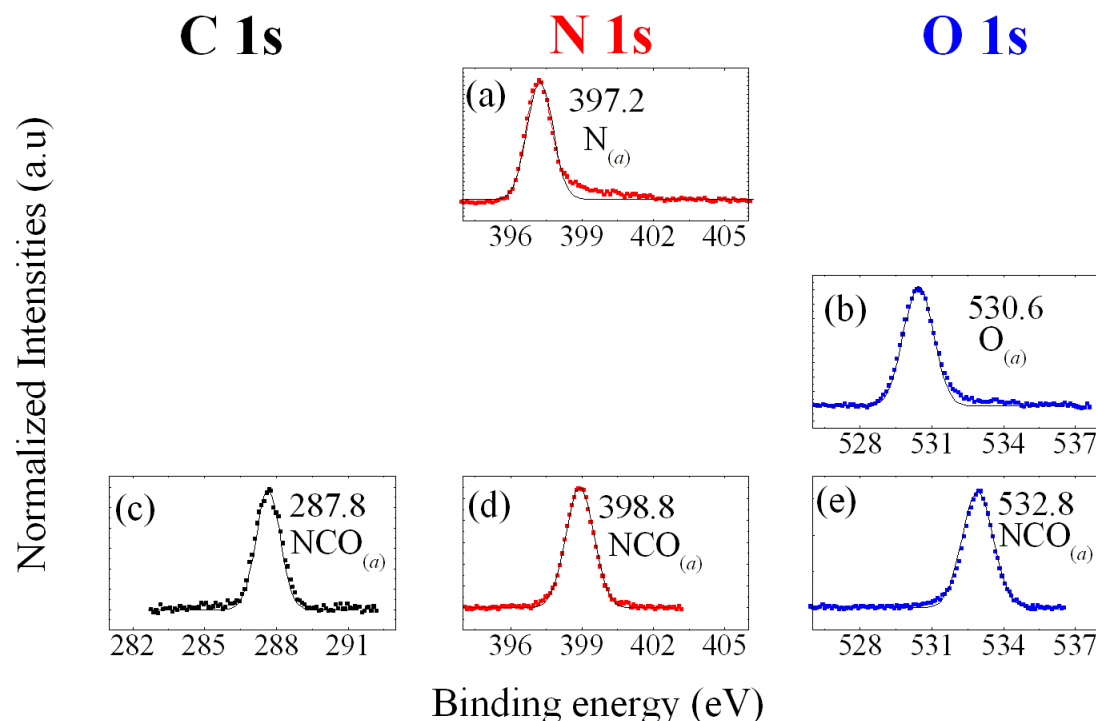
528 531 534 537

Binding energy (eV)

Figure 6.1. Room temperature XPS spectra from (a) N/Cu(001); (b) O/Cu(001). (c, d, e) are taken from the HNCO exposed surface, NCO/Cu(001). Photon beam energy = 650eV. Pass energy = 10eV. The binding energy of each peak was referenced to corresponding bulk Cu3p peaks at 75.2 and 78.0 eV. All spectra are shown after Shirley background subtractions.

shows a single XPS line at 397.2 eV (Fig. 6.1(a)). STM and Rutherford backscattering studies [47-49] have confirmed that this procedure produces an N saturated surface with a c(2x2) superstructure extending fully across the surface with an absolute coverage of 0.5ML. The second coverage calibration standard, O_2 saturated O/Cu(001), was prepared by dissociative O_2 adsorption at RT from a backfilling exposure of ~6000L. Helium atom scattering has confirmed the completion of an ordered phase at these exposure levels [50]. Helium diffraction then indicates a ($\sqrt{2}$ x $2\sqrt{2}$)R45^o superstructure [51], which is also seen with Low Energy Electron Diffraction (LEED) [50]. Independent Auger Electron Spectroscopy (AES) and Surface Extended X-ray Absorption Fine

Structure (SEXAFS) studies have also determined the absolute O coverage of this surface as 0.5 ML. [52] The resultant surface yields a single O 1s feature at 530.6 eV (Fig. 6.1(b)), which is attributed to the 0.5ML of atomic oxygen adatoms.

Dissociative adsorption of isocyanic acid (HNCO) at RT yields an $NCO_{(a)}$ covered Cu(001) surface, via

$$HNCO \xrightarrow{\;RT\;} NCO_{(a)} + H_{(a)} \xrightarrow{\;RT\;} NCO_{(a)} + \frac{1}{2} H_{2(g)} \quad , \tag{6.1}$$
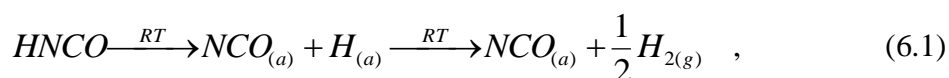
and which shows three XPS features with binding energies at 287.8, 398.8 and 532.8 eV, (Figs. 6.1(c), (d), (e)). At this point, it is worth underlining that the C 1s binding energy associated with $NCO_{(a)}$ species is ~2.6 eV higher than has been seen for $CN_{(a)}$, adsorbed on the same substrate[53], and is ~3.4 eV higher than is reported for an adsorbed graphitic carbon at 284.4 eV.[54] In contrast, the N 1s binding energies of $NCO_{(a)}$ and $CN_{(a)}$ are not expected to be resolved.

Absolute coverages of NCO/Cu(001) surfaces, including that of the HNCO saturated surface, were determined by comparing the integrated N 1s and O 1s peak intensities with the corresponding peak intensities measured from the calibration N/Cu(001) and O/Cu(001) surfaces. The coverage calibrations with respect to the saturated N/Cu(001) surface suggest that the saturation coverage of NCO/Cu(001) is 0.52±0.02 ML. The double check, with respect to the O/Cu(001) surface, suggests that the saturation coverage of NCO/Cu(001) is 0.51±0.2 ML. Angle resolved helium diffraction indicates a c(2x2) ordered superstructure on the saturated NCO/Cu(001) surface, which is again

supportive of the NCO/Cu(001) calibration.[30]   Finally, the relative N and C sensitivities are also fully consistent with those for C_2N_2 exposed surfaces. [53]

6.4.2. Oxidation of NCO$_{(a)}$ species on Cu(001)

Dissociative adsorption of 400L HNCO on Cu(001) at RT, at which hydrogen readily desorbs from surface [38], also leaves only NCO$_{(a)}$ species on the surface. Subsequent dissociative adsorption of O_2 on the subsaturated NCO/Cu(001), leads to four apparent XPS features at 532.8, 398.8, 287.8 and 530.6 eV, (Figs. 6.2 (a), (b), (c).) While the former three figures are the binding energies associated with NCO$_{(a)}$ species, the peak at 530.6 eV is attributed to co- adsorbed oxygen adatoms, (by comparison with 6.1(b)). Oxygen co-adsorption on NCO/Cu(001) surface changes essentially neither the intensities nor the binding energies of XPS features associated with NCO$_{(a)}$ species. (Compare line positions with those of Figs. 6.1(c), 6.1(d), and 6.1(e).) At RT, only a very limited degree of chemical interaction between NCO$_{(a)}$ and O$_{(a)}$ species is apparent in the weak shoulder at 397.2 eV of Fig. 6.2(b). A small extent of an oxidative reaction could be implied, possibly on defect sites. The oxidation reaction, we show here, approaches completion at higher temperatures.
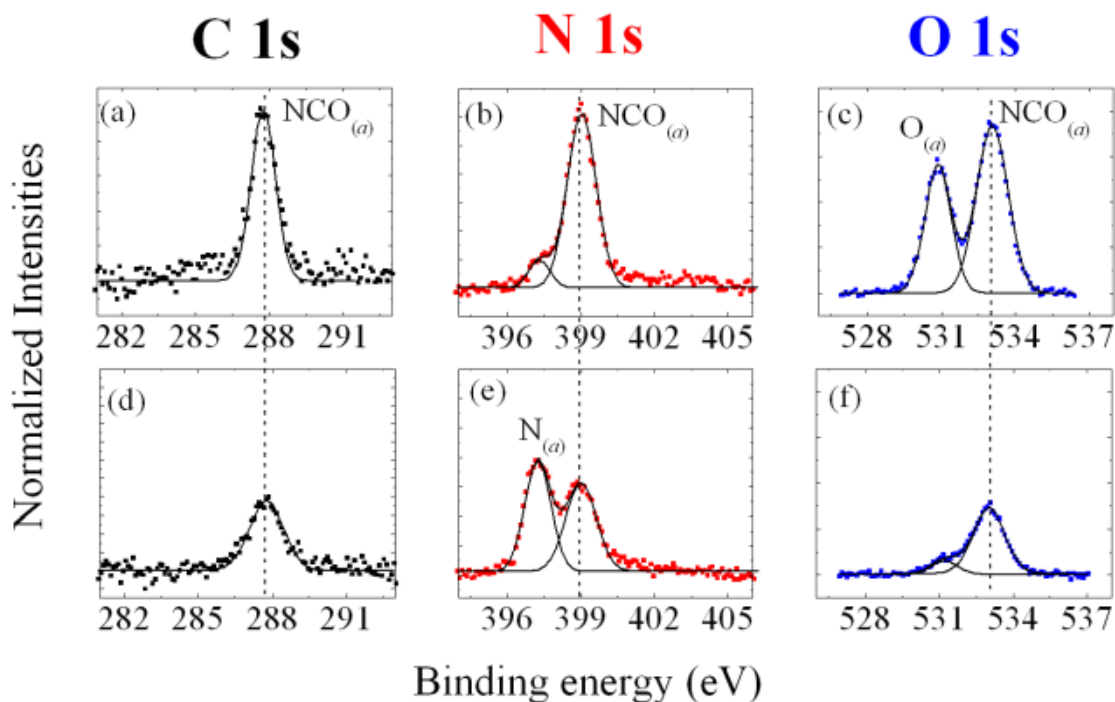
Figure 6.2.   RT XPS spectra (a,b,c) associated with dissociative adsorption of 400L HNCO on Cu(001) at RT followed by excess exposures of O_2. (d,e,and f) show the spectra from the surface after 5 min. annealing at 473K.

The O+NCO/Cu(001) prepared sample was annealed at 473K for 5 minutes. The surface was then probed again with XPS at RT, (see Figs. 6.2(d), 6.3(e), and 6.3(f)). The anneal treatment removed the large majority of the initial $O_{(a)}$ species, and the $NCO_{(a)}$ density is significantly reduced. The weak feature at 397.2 eV in Fig. 6.2(b) grows to dominate the N 1s spectral region shown in Fig. 6.2(e). Oxygen (O_2) does not desorb from an O/Cu(001) surface at 473K or below. [51]. Our independent thermal stability tests of $NCO_{(a)}$ species on Cu(001) also indicate that $NCO_{(a)}$ alone is stable up to at least 473K [41]. The annealed O+NCO/Cu(001) surface has thus undergone a chemical change; $NCO_{(a)}$ reacting with O species on the surface.

XPS feature	O_{1s} 530.6eV	O_{1s} 532.8eV	C_{1s} 287.8eV	N_{1s} 397.2eV	N_{1s} 398.8eV
Associated species	$O_{(a)}$	$NCO_{(a)}$	$NCO_{(a)}$	$N_{(a)}$	$NCO_{(a)}$
Initial RT levels (ML)	0.156	0.244	0.265	0.018	0.255
Levels post 473 K anneal (ML)	0.019	0.106	0.136	0.143	0.122
Coverage change = Final – Initial (ML)	-0.137	-0.138	-0.129	+0.125	-0.132

Table 6.1.   Surface coverages and changes as determined by integrated intensities of all XPS features shown in Fig. 6.2. The lowest row of the table reports indicated surface coverage variations resulting from a 5 minute anneal at 473K of the RT exposed NCO+O/Cu(001) surface.

A quantitative analysis of the spectral changes before and after annealing, shown in Fig. 6.2, is summarized in Table 6.1. To monitor the consistency of our quantitative analysis, as described in Section 6.4.1, three independent coverage calibrations were used. (The saturated CN/Cu(001) is used as the reference for the coverage calibration of carbon atoms.) Thus, $NCO_{(a)}$ surface populations determined by corresponding O 1s, C 1s and N 1s features can vary slightly within each row in Table 6.1. It is apparent however that, to within less than 0.013ML, the surface population of nitrogen is preserved, whilst there is a conversion of ~0.133ML conversion from $NCO_{(a)}$ to $N_{(a)}$. I.e. the generated $N_{(a)}$ essentially equals the loss of $NCO_{(a)}$ moieties. The extent of $O_{(a)}$ and $NCO_{(a)}$ losses are also virtually identical. This implies immediately that two oxygen atoms per carbon atom are simultaneously lost/removed from the surface, most probably in the form of $CO_{2(g)}$.

$$NCO_{(a)} + O_{(a)} \rightarrow CO_{2(g)} + N_{(a)} \qquad (6.2)$$
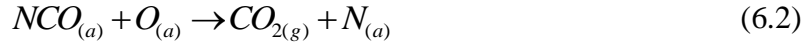
The same experiment with differing initial NCO/O proportions, yielded the same result: $CO_{2(g)}$ and $N_{(a)}$ are the only reaction products. Reaction (6.2) is thermally activated at a temperature between 373-473K and it can run until near depletion of one of the reactants, i.e. $NCO_{(a)}$ or $O_{(a)}$.

6.4.3. RT oxidation of $CN_{(a)}$ species and subsequent thermally activated processes

A surface prepared by dissociative coadsorption successively of $C_2N_2 + O_2$ at RT produces five XPS features with binding energies at 285.2, 287.8, 398.8, 530.6 and 532.8 eV (Figs. 6.3(a), (b), and (c)). The observed binding energies except 285.2 eV are essentially identical to those seen in the calibration measurements presented in Figs. 6.1(a)-(e). In Chapters 3 and 4, we have demonstrated that CN/Cu(001) surface manifests itself with 285.2 and 398.8 eV features in XPS. Thus, we can conclude that $C_2N_2 + O_2$ co-adsorption generates a surface simultaneously containing $O_{(a)}$, $CN_{(a)}$ and $NCO_{(a)}$ species, as had been suggested by Carley et al.[37] An incomplete oxidation of $CN_{(a)}$ with $O_{(a)}$ to $NCO_{(a)}$ is implied,

$$CN_{(a)} + O_{(a)} \xrightarrow{T_x = RT} NCO_{(a)} \qquad (6.3)$$

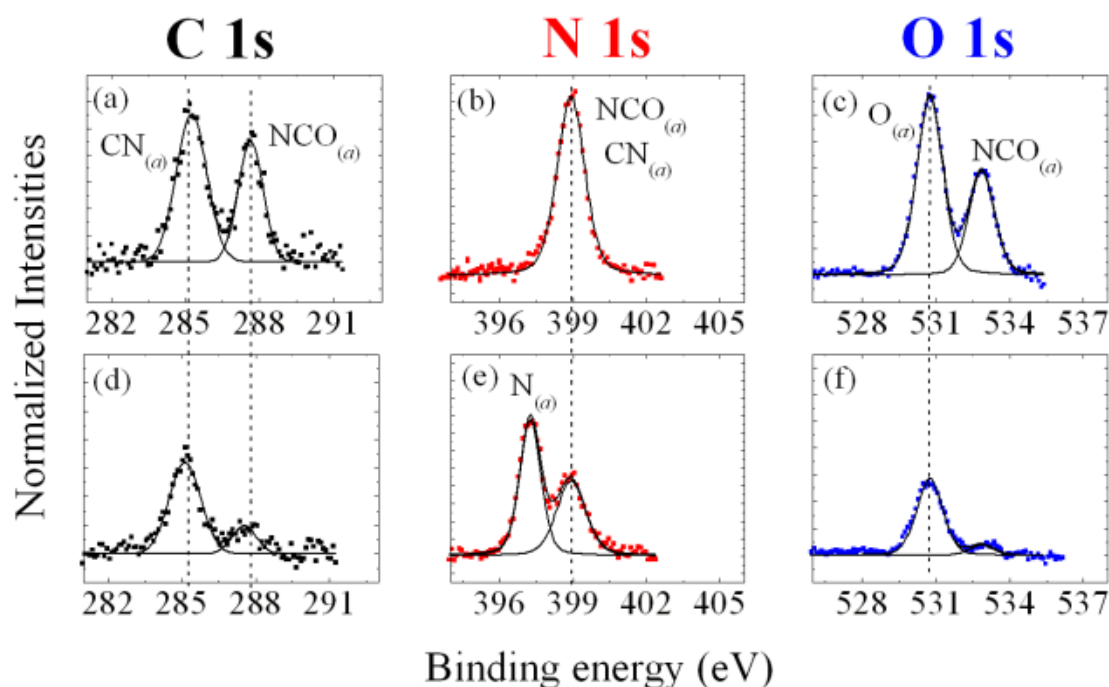despite an excess of co-adsorbed oxygen.

Figure 6.3.   (a) C1s, (b) N1s and (c) O1s XPS features upon RT co-adsorption of 200L O_2 and excess C_2N_2 on Cu(001).   (d), (e) and (f) show respectively the same binding energy regions of RT XPS spectra taken after 5min. annealing of the surface at 473K.

Various C_2N_2 and O_2 exposure combinations were also tried to achieve complete $CN_{(a)}$ oxidation at RT, yet it was not possible to find a combination which yielded $NCO_{(a)}$ species, exclusively. Excess $CN_{(a)}$ was observed at low O_2 exposures, excess $O_{(a)}$ was observed at low C_2N_2 exposures, and both $CN_{(a)}$ and $O_{(a)}$ coexisted at intermediate relative exposures. The Reaction (6.3) is not at thermodynamic equilibrium, as $NCO_{(a)}$ shows no sign of spontaneous decomposition (Figs. 6.1(c) and 6.1(e)) at RT. Reaction (6.3) is not reversible at RT. The observation of coexisting $NCO_{(a)}$, $CN_{(a)}$ and $O_{(a)}$ species thus implies a kinetic limitation to the reaction between $CN_{(a)}$ and $O_{(a)}$ species. We first propose that $NCO_{(a)}$ forms at the boundary of surface segregated patches with differing $CN_{(a)}$ densities. In contrast to O/Cu(001), $CN_{(a)}$ alone is known to phase separate at intermediate coverages on Cu(001) into lower and higher density phases.[30]

Secondly, the CN+O reaction can then be slowed if the migration of $CN_{(a)}$ to $O_{(a)}$, or visa versa, were limited by a strongly-bound NCO-containing diffusion barrier.

XPS feature	O_{1s} 530.6eV	O_{1s} 532.8eV	C_{1s} 285.2eV	C_{1s} 287.8eV	N_{1s} 397.2eV	N_{1s} 398.8eV
Associated species	$O_{(a)}$	$NCO_{(a)}$	$CN_{(a)}$	$NCO_{(a)}$	$N_{(a)}$	$CN_{(a)}+NCO_{(a)}$
Initial RT levels (ML)	0.205	0.126	0.195	0.126	0	0.321
Levels post 473 K anneal (ML)	0.089	0.009	0.115	0.027	0.188	0.134
Coverage change (ML)	-0.116	-0.117	-0.080	-0.108	+0.188	-0.187

Table 6.2.   Surface coverages and changes as determined from RT integrated intensities of all XPS features shown in Fig. 6.3. The lowest row of the table reports indicated surface coverage variations resulting from a 5 minute anneal at 473K of the RT O+CN+NCO/Cu(001) surface.

In order to investigate the $NCO_{(a)}$ oxidation reaction further the surface, illustrated in Figs. 6.3(a)-(c), was also annealed to 473K.   The subsequent XPS spectra (Figs. 6.3(d)-(f)), show a reduction of $CN_{(a)}$, $NCO_{(a)}$ and $O_{(a)}$ population and the appearance of a new feature at 397.2 eV, which was previously ascribed to nitrogen adatoms (compare with Fig. 5.1(a)).   Qualitatively speaking, the $NCO_{(a)}$ loss and simultaneous $N_{(a)}$ generation appears similar to the results reported in Section 6.4.2, i.e. for oxidation of $NCO_{(a)}$ in the absence of $CN_{(a)}$ species.

Quantitative analyses of post and pre-annealed surfaces, however, suggest that Reaction (6.2) is not the only active process. Indeed the analysis results, outlined in Table 6.2, suggest that while the nitrogen population on the surface is again preserved, the surface concentrations of both $CN_{(a)}$ and $NCO_{(a)}$ species decrease. Significant C_2N_2 desorption from CN/Cu(001) occurs only at temperatures in excess of 575K [53]. Here, with co-adsorbed $CN_{(a)}$, $O_{(a)}$, and $NCO_{(a)}$, the preserved nitrogen level also clearly excludes C_2N_2 desorption below 473K. $CN_{(a)}$ dissociation is also not supported as graphitic carbon, anticipated at 284.4 eV [54], is not seen on this surface. The combined information suggests that a further fraction of the $CN_{(a)}$ species can be converted to $NCO_{(a)}$ in the annealing step,

$$CN_{(a)} + O_{(a)} \xrightarrow{RT < T_x \leq 473} NCO_{(a)} \tag{6.4}$$
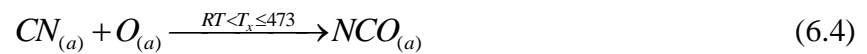
The observed $O_{(a)}$ loss (0.116ML in Table 6.2) was insufficient to explain both the $CN_{(a)}$ consumption by thermally activated oxidation (4) and the complete oxidation of all $NCO_{(a)}$ species through Reaction (6.2). Reactions (6.4) and (6.2) alone would have required a more than doubled $O_{(a)}$ loss , i.e. ~ 0.27 ML.

An approximate overall stoichiometry for the reaction processes during annealing, suggested by Table 6.2, is given by,

$$NCO_{(a)} + O_{(a)} + 0.69\,CN_{(a)} \rightarrow \underline{C_{1.69}O_{2(g)}} + 1.69\,N_{(a)} \tag{6.5}$$
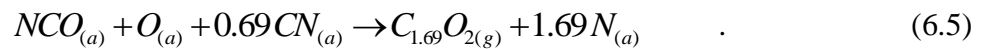
Given the conservation of the surface nitrogen level throughout the reactions, the most realistic gas phase products are CO_2 and CO. The following is implied,

$$NCO_{(a)} + O_{(a)} + 0.69\,CN_{(a)} \rightarrow 1.38\,CO_{(g)} + 0.31\,CO_{2(g)} + 1.69\,N_{(a)} \tag{6.6}$$
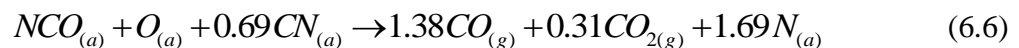
which suggests a new competing reaction, namely a thermally induced dissociation of the $NCO_{(a)}$ species,

$$NCO_{(a)} \rightarrow CO_{(g)} + N_{(a)} \tag{6.7}$$

Both Reactions (6.2) and (6.7) run at intermediate temperatures, $RT \leq T_x \leq 473K$. $N_{(a)}$ is a common product, though the volatile products are respectively $CO_{2(g)}$ and $CO_{(g)}$. Reaction (6.7) proved to be the dominant mechanism for $NCO_{(a)}$ removal; (6.7)/(6.2) reaction yields appeared in a ratio of 1.38/0.31. In other words, the dissociation reaction, Reaction (6.7), is the primary mechanism for the removal of $NCO_{(a)}$ species from the CN+O+NCO/Cu(001) surface. The overall reaction for removal of one $NCO_{(a)}$ species in Reaction (6.6), with this set of particular initial concentration ratios, can be described as x (6.2) + y (6.4) + z (6.7) with x = 0.31, y = 0.69 and z = 1.38. Incidentally the x, y and z coefficients, and their ratios, are strongly dependent on the O_2 and C_2N_2 exposures, i.e. on the initial $O_{(a)}$, $CN_{(a)}$ and $NCO_{(a)}$ coverages. For example, somewhat intuitively, proportionately less $CO_{2(g)}$ production (Reaction (6.2)) and less $CN_{(a)}$ oxidation (Reaction(6.4)) are seen with lower initial $O_{(a)}$ levels.

In the absence of $CN_{(a)}$ on an NCO+O/Cu(001) surface, $CO_{2(g)}$ is the only gaseous product seen upon annealing to 473K (Section 6.4.2) as per Reaction (6.2). $CO_{(g)}$ evolution, resulting from the competing dissociation Reaction (6.7), is observed however only in the presence of co-adsorbed $CN_{(a)}$. We propose then that the dissociation Reaction (6.7) is catalyzed by the presence/proximity of co-adsorbed cyanide species, $CN_{(a)}$. The scheme for the competing $NCO_{(a)}$ elimination reactions are summarized in Fig. 6.4 below.
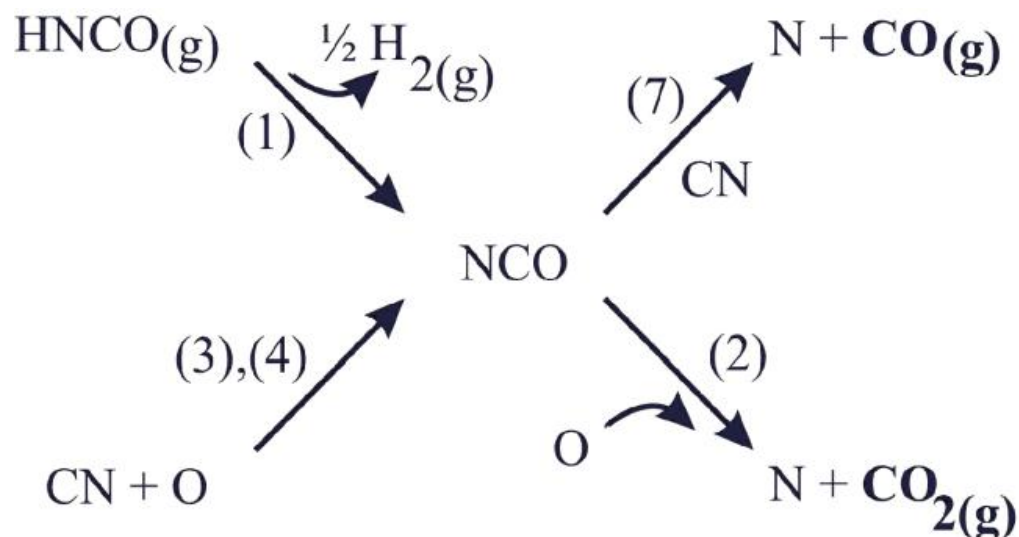
$$HNCO_{(g)} \quad \tfrac{1}{2}H_{2(g)} \qquad\qquad N + CO_{(g)}$$

(1) (7)

CN

NCO

(3),(4) (2)

O

CN + O

$$N + CO_{2(g)}$$

Figure 6.4.   Schematic of the reaction mechanisms for $NCO_{(a)}$ formation on, and $NCO_{(a)}$ removal from, the Cu(001) surface.

A post adsorption sequence of Reaction (6.7) alone would be insufficient to explain the total $CO_{(g)}$ yield. Likewise the dissociation through Reaction (6.7) of all $NCO_{(a)}$ formed through Reaction (6.4) during the annealing process alone produces insufficient $CO_{(g)}$ yield. In other words both existing and newly formed $NCO_{(a)}$ are necessary to give adequate CO desorption from Reaction (6.7).

Upon RT C_2N_2 and O_2 exposures, Reaction (6.3) self limits. Earlier in this section we had proposed that an $NCO_{(a)}$ barrier, to diffusion of both $CN_{(a)}$ or $O_{(a)}$ species, limits the mutual approach of these species. On heating to 473K, Reactions (6.7) and/or (6.2), can degrade the barriers' affectivity by replacing $NCO_{(a)}$ species with presumably immobile $N_{(a)}$ and thereby re-enabling Reaction (6.4). With production of more $NCO_{(a)}$, from remaining $CN_{(a)}$ and $O_{(a)}$ moieties on the surface, the width of the NCO- and N-containing physical barrier will increase further. Eventually, the $CN_{(a)} + O_{(a)}$ reaction is

again kinetically limited. The final surface, observed at RT but after the anneal process contains $CN_{(a)} + O_{(a)} + N_{(a)}$. All $NCO_{(a)}$ is depleted but the $N_{(a)}$ is now sufficient to prevent completion of Reaction (6.4).

6.4.4. TPRD measurements from NCO+O/Cu(001) and CN+O+NCO/Cu(001) surfaces:

The gas phase products of the thermally activated reactions from NCO+O/Cu(001) and NCO+CN+O/Cu(001) surfaces were monitored with temperature programmed reactive desorption (TPRD). Ion yields at m/z = 14, 28, 30, 43, 44 and 52 were monitored. As predicted by the XPS results, only m/z = 28 and m/z = 44 amu/e$^+$ features exhibited discernable yields.

NCO+O/Cu(001) and NCO+CN+O/Cu(001) surfaces were prepared with the same nominal routines as described in Sections 6.4.2 and 6.4.3. However, as the experiments were performed in different chambers, precise surface compositions could not be reproduced. TPRD results are shown in Fig. 6.5.
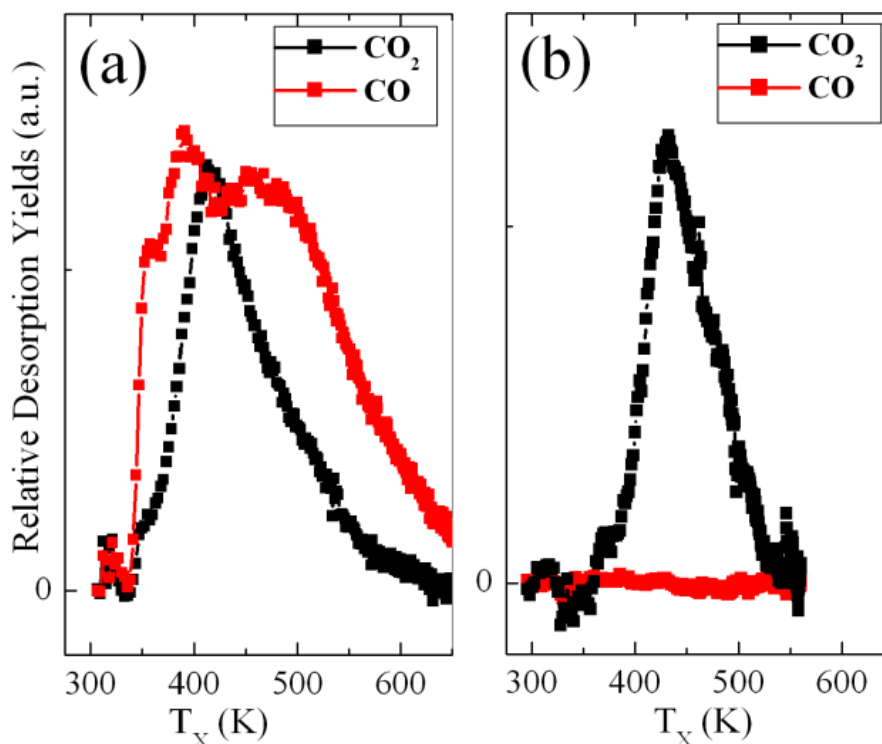
Figure 6.5. TPRD curves from the samples prepared by (a) the co-adsorption of 200 L O_2 followed by excess exposure of C_2N_2 , (b) co-adsorption of 400L HNCO followed by excess exposures of O_2. Intensities of desorption peaks were normalized.

The normalized $CO_{(g)}$ and $CO_{2(g)}$ curves shown represent our best estimates of instantaneous relative $CO_{(g)}$ and $CO_{2(g)}$ yields, as derived from processed mass 44 and 28 scan data. To achieve this the cracking patterns and absolute signal levels for pure $CO_{(g)}$ and pure $CO_{2(g)}$ backfills were individually measured, both at ~10^{-9} mbar, after correction with the vendor tabulated ion gauge sensitivities. The instantaneous $CO_{2(g)}$ component at mass = 28 was subtracted from the total instantaneous mass 28 signal. The remainder is then attributed to $CO_{(g)}$ desorption. Fig. 6.5(a) indicates comparable maximum $CO_{2(g)}$ and $CO_{(g)}$ desorption yields. In contrast Fig. 6.5(b) does not indicate any $CO_{(g)}$ desorption.

Qualitatively speaking, the clear difference between the results of Figs. 6.6(a) and 6.6(b) is that CO desorption occurs only from the NCO+CN+O/Cu(001) surface. This observation is in full agreement with the XPS analysis results reported in Sections 6.4.2 and 6.4.3, and the dissociation reaction of $NCO_{(a)}$ species (Reaction (6.7)) is catalyzed by the presence/proximity of $CN_{(a)}$ moieties.

Quantitatively: the ratio of the integrated curve area in Fig. 6.5, I_{CO}/I_{CO2}, is ~7/3 = $2.\dot{3}$ which differs significantly from that found in Section 6.4.3, i.e. 1.38/0.31 = 4.4. We believe that the ratio difference is related to the non-reproducibility of exposures in the two experimental chambers. A second possible cause of the disparity could arise from inaccuracies in the vendor-quoted ionization efficiency values used for the TPRD curve normalization. (It is well known that variations between ion gauges are to be found that can vary also with time and operational history.) Yet, regardless of the evident CO/CO_2 yield difference, this TPRD study confirms the desorption of both CO and CO_2 from a thermally treated CN+O+NCO/Cu(001) surface while CO_2 is the only desorbing gas from O+NCO/Cu(001) surface. The TPRD analysis also indicates that more $CO_{(g)}$ is produced than $CO_{2(g)}$ in Fig. 6.5(a), i.e. for $CN_{(a)}$ containing surfaces the dissociation reaction can be the dominant mechanism for $NCO_{(a)}$ removal from Cu(001)

6.5.   Conclusion

Oxidation and decomposition reactions of $NCO_{(a)}$ species adsorbed on Cu(001) were studied with soft XPS and TPRD measurements.   A thermal anneal of the NCO+O/Cu(001) surface to 473K leads to a single oxidation reaction which generates adsorbed nitrogen and gas phase CO_2 as products.   When the NCO+CN+O/Cu(001) surface was annealed in the same manner, we observe the generation of both CO_2 and CO in the gas phase along with remaining adsorbed nitrogen.   Quantitative analysis of the XPS peak intensities implies that a new reaction, dissociation of an $NCO_{(a)}$ species which is catalyzed only in the presence of proximal $CN_{(a)}$, is responsible for the CO production. The CO_2/CO production ratio varies on the relative populations of $CN_{(a)}$, $NCO_{(a)}$ and $O_{(a)}$ on the surface prepared by C_2N_2 and O_2 co-adsorption at RT.   Nevertheless, it is clear that the decomposition reaction, yielding CO, can be the dominant mechanism, for $NCO_{(a)}$ elimination; for high $CN_{(a)}$ levels it is more significant than the oxidation reaction that yields CO_2.   Electric fields have been shown to induce perturbations in adsorbed NO on platinum[55] and in adsorbed CO on ruthenium[56]. Similar oxygen-induced electric fields have been cited as a possible explanation for the increased $NCO_{(a)}$ stabilities in the proximity of $O^{\delta-}_{(a)}$ moieties.   In our case of the $CN^{\delta-}_{(a)}$ moiety, its influence on $NCO_{(a)}$ species appears to be in the opposite sense; $NCO_{(a)}$ is destabilized by $CN_{(a)}$.

Although these reactions occurred under idealized UHV conditions on single crystal Cu(001) surfaces, far from the complexity of events that can happen in real catalytic systems, our observations imply an important phenomenon; if $NCO_{(a)}$ is a key

intermediate for the reduction of NO_x species, the presence of the $CN_{(a)}$ species may significantly alter the catalytic role envisioned for $NCO_{(a)}$. $CN_{(a)}$ species are known to be present on many real catalytic processing surfaces. [21, 22, 47, 57-61]

6.5.　References

[1]　W. C. Hecker and A. T. Bell, Journal of Catalysis 84 (1983) 200.
[2]　D. A. Lorimer and A. T. Bell, Journal of Catalysis 59 (1979) 223.
[3]　É. Novák and F. Solymosi, Journal of Catalysis 125 (1990) 112.
[4]　F. Solymosi and J. Raskó, Journal of Catalysis 63 (1980) 217.
[5]　F. Solymosi, J. Sárkány, and A. Schauer, Journal of Catalysis 46 (1977) 297.
[6]　M. L. Unland, Journal of Catalysis 31 (1973) 459.
[7]　M. L. Unland, Science 179 (1973) 567.
[8]　M. F. Brown and R. D. Gonzalez, Journal of Catalysis 44 (1976) 477.
[9]　B. A. Morrow, W. N. Sont, and A. S. Onge, Journal of Catalysis 62 (1980) 304.
[10]　R. A. Dalla Betta and M. Shelef, Journal of Molecular Catalysis 1 (1976) 431.
[11]　F. Solymosi and T. Bansagi, The Journal of Physical Chemistry 83 (1979) 552.
[12]　F. Solymosi, L. Völgyesi, and J. Sárkány, Journal of Catalysis 54 (1978) 336.
[13]　F. Solymosi and T. Bansagi, Journal of Catalysis 156 (1995) 75.
[14]　W. Held, A. Konig, T. Riher, and L. Ruppe, SAE Paper 900496 (1990)
[15]　M. Iwamoto, Proceedings of the Meeting of Catalytic Technology for Removal of Nitrogen Monoxide, Tokyo (January 1990) pg. 17.
[16]　M. Iwamoto, H. Yahiro, S. Shundo, Y. Yuu, and N. Mizuno, Shokubai (Catalyst) 32 (1990) 430.
[17]　Y. Ukisu, S. Sato, G. Muramatsu, and K. Yoshida, Catalysis Letters 11 (1991) 177.
[18]　Y. Ukisu, S. Sato, A. Abe, and K. Yoshida, Applied Catalysis B: Environmental 2 (1993) 147.
[19]　H. Takeda and M. Iwamoto, Catalysis Letters 38 (1996) 21.
[20]　H. He, J. Wang, Q. Feng, Y. Yu, and K. Yoshida, Applied Catalysis B: Environmental 46 (2003) 365.
[21]　F. Lónyi, J. Valyon, L. Gutierrez, M. A. Ulla, and E. A. Lombardo, Applied Catalysis B: Environmental 73 (2007) 1.
[22]　A. Shichi, T. Hattori, and A. Satsuma, Applied Catalysis B: Environmental 77 (2007) 92.
[23]　F. Zhang, S. Zhang, N. Guan, E. Schreier, M. Richter, R. Eckelt, and R. Fricke, Applied Catalysis B: Environmental 73 (2007) 209.
[24]　J. Raskó and F. Solymosi, Journal of Catalysis 71 (1981) 219.
[25]　K. L. Kostov, P. Jakob, H. Rauscher, and D. Menzel, The Journal of Physical Chemistry 95 (1991) 7785.

[26]   K. L. Kostov, H. Rauscher, and D. Menzel, Surface Science 287-288 (1993) 283.
[27]   C. Hess, E. Ozensoy, and D. W. Goodman, The Journal of Physical Chemistry B 108 (2004) 14181.
[28]   E. Ozensoy, C. Hess, and D. W. Goodman, Journal of the American Chemical Society 124 (2002) 8524.
[29]   F. Solymosi and T. Bánsági, Journal of Catalysis 202 (2001) 205.
[30]   J. Kiss and F. Solymosi, Journal of Catalysis 179 (1998) 277.
[31]   R. Németh, J. Kiss, and F. Solymosi, The Journal of Physical Chemistry C 111 (2007) 1424.
[32]   A. R. Balkenende, O. L. J. Gijzeman, and J. W. Geus, Applied Surface Science 37 (1989) 189.
[33]   P. J. Godowski, J. Onsgaard, A. Ga¸gor, M. Kondys, and Z. S. Li, Chemical Physics Letters 406 (2005) 441.
[34]   F. Solymosi and A. Berko, Surface Science 122 (1982) 275.
[35]   F. Solymosi and J. Kiss, Surface Science 104 (1981) 181.
[36]   F. Solymosi and J. Kiss, Surface Science 108 (1981) 368.
[37]   A. F. Carley, M. Chinn, and C. R. Parkinson, Surface Science 537 (2003) 64.
[38]   H. Celio, K. Mudalige, P. Mills, and M. Trenary, Surface Science 394 (1997) L168.
[39]   G. R. Garda, R. M. Ferullo, and N. J. Castellani, Surface Science 598 (2005) 57.
[40]   Y. Li, J. M. Hu, Y. F. Zhang, and J. Q. Li, Applied Surface Science 252 (2006) 5636.
[41]   E. Z. Ciftlikli, E. Y. M. Lee, J. Lallo, S. Rangan, L. Tskipuri, R. A. Bartynski, and B. J. Hinch, In preparation.
[42]   R. J. Gorte, L. D. Schmidt, and B. A. Sexton, Journal of Catalysis 67 (1981) 387.
[43]   J. E. Jones and M. Trenary, The Journal of Physical Chemistry C 112 (2008) 20443.
[44]   L. V. Goncharova, J. Braun, A. V. Ermakov, G. Bishop, D.-M. Smilgies, and B. J. Hinch, Journal of Chemical Physics Vol. 115 No 16 (2001) 7713.
[45]   G. Herzberg and C. Reid, Discussions of the Faraday Society 9 (1950) 92.
[46]   M. Linhard, Zeitschrift fuer Anorganische und Allgemeine Chemie 236 (1938) 200.
[47]   X. Chen, X. Yang, A. Zhu, C. T. Au, and C. Shi, Journal of Molecular Catalysis A: Chemical 312 (2009) 31.
[48]   S. M. Driver and D. P. Woodruff, Surface Science 492 (2001) 11.
[49]   F. M. Leibsle, S. S. Dhesi, S. D. Barrett, and A. W. Robinson, Surface Science 317 (1994) 309.
[50]   A. V. Ermakov, E. Z. Ciftlikli, S. E. Syssoev, I. G. Shuttleworth, and B. J. Hinch, Review of Scientific Instruments 81 (2010) 105109.
[51]   E. Z. Ciftlikli, S. Sysoev, A. V. Ermakov, and B. J. Hinch, Unpublished Results
[52]   M. Wuttig, R. Franchy, and H. Ibach, Surface Science 213 (1989) 103.
[53]   E. Z. Ciftlikli, E. Y. M. Lee, J. Lallo, S. Rangan, S. D. Senanayake, and B. J. Hinch, Langmuir 26 (2010) 18742.
[54]   T. L. Barr and S. Seal, Journal of Vacuum Science & Technology A: Vacuum, Surfaces, and Films 13 (1995) 1239.
[55]   H. J. Kreuzer and L. C. Wang, Vol. 93, AIP, 1990, p. 6065.

[56]   H. J. Kreuzer, Surface Physics and Chemistry in High Electric Fields, Springer-Verlag, 1990.
[57]   N. Bion, J. Saussey, M. Haneda, and M. Daturi, Journal of Catalysis 217 (2003) 47.
[58]   F. Poignant, J. L. Freysz, M. Daturi, and J. Saussey, Catalysis Today 70 (2001) 197.
[59]   S. Tamm, H. H. Ingelsten, and A. E. C. Palmqvist, Journal of Catalysis 255 (2008) 304.
[60]   T. Venkov, M. Dimitrov, and K. Hadjiivanov, Journal of Molecular Catalysis A: Chemical 243 (2006) 8.
[61]   V. Matsouka, M. Konsolakis, R. M. Lambert, and I. V. Yentekakis, Applied Catalysis B: Environmental 84 (2008) 715.

CHAPTER 7

CONCLUSION

C_2N_2 exposures on Cu(001) surface at 263K lead to a CN-only surface yielding a ordered superstructure of c(10x6) which was observable only with angle resolved HAS. Coverage calibrations performed with XPS for CN/Cu(001) suggests that the CN coverage at saturation is about 0.41 ML, implying 12-13 CN species accommodated within each 30-copper-atom large unit cell. NEXAFS probing of the same surface returns a complicated N 1s-π^* spectrum, implying CN moieties with a number of different binding sites and/or bonding orientations coexisting on the Cu(001) surface. The breakdown of the π^* spectral feature indicates there should be at least three different types of CN moieties on the saturated CN/Cu(001) surface.

I also aimed to augment the structural information listed above with an estimation of binding energy of CN species on Cu(001). For this purpose, desorption spectra from the CN/Cu(001) surface were utilized to determine the activation energy of desorption (E_d), which in the next step can be used to estimate binding energies of adsorbed CN species on the copper. However, the traditional analysis techniques, which work on the assumption that the value of E_d is independent of CN coverage, cannot be applied properly to our system since mutually repulsive dipolar interactions among $CN^{\delta-}$ are expected to lead to a marked desorption energy reduction with increasing CN coverages. In order to overcome this problem, we have developed a new analysis approach specifically targeting the estimation of coverage dependent component of E_d in the range

of $0 < \theta \leq \theta_m^{sat}$. In contrast to the Habenschaden-Küppers/ Leading Edge analysis, the new technique works very well without superb signal-to-noise ratios in the desorption spectra. E_d value for the C_2N_2 desorption from CN/Cu(001) surface is determined to be in the 160-163 kJ/mol range.

TOF-HAS measurements from CN/Cu(001) at ΔK positions away from specular and diffraction peaks are dominated by a large multiphonon distribution together with a small diffuse elastic component. Excellent agreement between the multiphonon distribution in our data and the classical discrete model of multiphonon scattering implies that some of the CN species in an ordered superstructure have high vibrational amplitudes. The diffuse inelastic intensity is dominated by the most dynamic component of the surface. That fact that sharp superstructure diffraction peaks are observed simultaneously (which would have been unanticipated) implies that long range order is maintained despite the highly dynamic component. The component that exhibits elastic diffraction moves with comparatively low vibrational amplitudes. The elastically scattered intensity is dominated by the less dynamic CN species of the surface. This proposal relies on an inhomogeneous set of CN adsorbates, which is implicitly is implied by the fractional saturation coverage in a large unit cell structure and suggested by NEXAFS results indicating the existence of multiple CN species types. A set of rigidly placed CN species are expected to build the long range network. That network serves to induce the observed coherent diffraction peaks. The coexisting rigid and dynamic components of an ordered superstructure had thus far not been seen. The extreme

differences in CN binding configurations (within one unit cell) has enabled the first observation of this kind of distinction of dynamic behaviors.

An XPS investigation of the thermal treatment of pure NCO/Cu(001) surfaces, at 573K, shows the appearance of a new C 1s feature at 286.4 eV as well as a new N 1s feature at 398.4 eV binding energies. Quantitative analysis of the XPS data suggests a bimolecular process; two NCO moieties leading to formation of $CO_{2(g)}$ and leaving a stoichiometrically "CN_2" moiety adsorbed on the surface. RAIRS studies suggest that the "CN_2" is a carbodiimide species, i.e. NCN, with a linear "sp" hybridized central carbon atom. The comparative weakness of the v_a(NCN) band, as well as the absence of a v_s(NCN) band, suggest that the surface hosts high concentrations of NCN moieties that lie predominately parallel to the surface plane. The proposed electron-rich $NCN_{(a)}$ species, with a high thermal stability, which is obtainable at high surface concentrations, could be utilized as an active precursor in chemical modification of copper surfaces.

Oxidation and decomposition reactions of $NCO_{(a)}$ species adsorbed on Cu(001) were also studied with soft XPS and TPRD measurements. The effect of coadsorbed CN on NCO oxidation investigated by the comparison of the thermally induced reactions from NCO+O/Cu(001) surfaces with those of NCO+CN+O/Cu(001) surfaces at 473. K Quantitative analysis of the XPS peak intensities implies that while CO_2 is the only gaseous product from NCO+O/Cu(001), both CO and CO_2 is evolving from the NCO+CN+O/Cu(001) surface. TPRD measurements qualitatively confirm the outcomes of the XPS analysis. A new reaction, dissociation of an $NCO_{(a)}$ species which is

catalyzed only in the presence of proximal $CN_{(a)}$, is responsible for the CO production. The CO_2/CO yield ratio depends on the relative populations of $CN_{(a)}$, $NCO_{(a)}$ and $O_{(a)}$ on the surface prepared by C_2N_2 and O_2 co-adsorption at RT. Nevertheless, it is clear that the decomposition reaction, yielding CO, can be the dominant mechanism, for $NCO_{(a)}$ elimination; for high $CN_{(a)}$ levels. It becomes more significant than the oxidation reaction that yields CO_2. Although these reactions occurred under idealized UHV conditions on single crystal Cu(001) surfaces, far from the complexity of events that can happen in real catalytic systems, our observations imply an important phenomenon; if $NCO_{(a)}$ is a key intermediate for the reduction of NO_x species, the presence of the $CN_{(a)}$ species, whose presence has been reported on several occasions on many real catalytic processing surfaces, may significantly alter the catalytic role envisioned for $NCO_{(a)}$.

APPENDIX A

Processing and Normalization of Raw NEXAFS Results:

At the beginning, it must be emphasized that there is an inherent offset components to the raw signal intensities in all NEXAFS measurements and the magnitude of signal background is not insignificant in comparison to X-Ray absorption related features. For the proper application of the following normalization routines, this offset must be first subtracted from the raw signal. The simplest way of determining the magnitude of the offset is to close the gate valve between the sample and Synchrotron light source in the earliest moments of any data acquisition.

Normalization mechanics, which will be detailed below, is based on the "comprehensive" normalization method described by Watts, et al.[1] and it also takes the variation of % of the beam striking the sample surface into account. In order to perform this modified "comprehensive" normalization for a given raw NEXAFS data set, $I_s(E,t1)$ taken during a time period, $t1$, we need the mesh signal, $I_m(E,t1)$, collected simultaneously as well as another NEXAFS measurement performed during a different time period, $t2$, from a clean substrate, $I_s^{standard}(E,t2)$, and the corresponding mesh signal, $I_m^{standard}(E,t2)$. We then define a ratio of intensity ratios, $\Psi(E)$;

$$\frac{I_s(E,t1)/I_m(E,t1)}{I_s^{standard}(E,t2)/I_m^{standard}(E,t2)} = \Psi(E) = \frac{Z_1.\alpha_1.A_s(E).I(t1).\chi(E)/A_m(E).I(t1).\chi(E)}{Z_0.\alpha_0.A_s^{standard}(E).I(t2).\chi(E)/A_m^{standard}(E).I(t2).\chi(E)}$$

$$\Psi(E) = \frac{Z_1.\alpha_1.A_s(E) \Big/ A_m(E)}{Z_0.\alpha_0.A_s^{standard}(E) \Big/ A_m^{standard}(E)} \tag{A.1}$$

where;

I_s , I_m : Recorded signal intensities of sample and mesh signals

Z : % of the beam, striking the sample surface.

α : Polar angle dependence on illuminated surface area

$A(E)$: Photo-absorption spectra of sample or mesh.

$I(t1), I(t2)$: Time dependent variation of synchrotron beam intensity

$\chi(E)$: Energy dependent variation of synchrotron beam intensity

and the "standard" superscript is used to identify the measurements associated with a clean substrate.

We can assume the chemical state of the mesh stays stable from one measurement to another; $A_m(E) = A_m^{standard}(E)$. When they cancel each other in (A.1), we get rid of the ambiguity arising due to the TEY mode detection of the mesh signal.

$$\Psi(E) = \frac{Z_1.\alpha_1.A_s(E)}{Z_0.\alpha_0.A_s^{standard}(E)} \tag{A.2}$$

The $A_s(E)$, photo-absorption spectra of the sample, is composed of two components. One component is the intensity coming from an adsorbed overlayer, $N(E)$. (This is the signal

intensity we are trying to obtain at the end of the analysis.) The other component is the signal intensity from the substrate material under the adsorbed overlayer, $f.A_s^{standard}(E)$.

f is the fractional constant parameterizing the reduction of $A_s^{standard}(E)$ as a result of the shielding effect of the adsorbed overlayer. Therefore,

$$\Psi(E) = \frac{Z_1.\alpha_1.N(E) + Z_1.\alpha_1.f.A_s^{standard}(E)}{Z_0.\alpha_0.A_s^{standard}(E)} \tag{A.3}$$

Now, for a moment, let us consider the clean substrate measurement alone:

$$\frac{I_s^{standard}}{I_m^{standard}} = \frac{Z_0.\alpha_0.A_s^{standard}(E).I(t).\chi(E)}{A_m^{Au}(E).I(t).\chi(E)} = \frac{Z_0.\alpha_0.A_s^{standard}(E)}{A_m^{Au}(E)} = \frac{Z_0.\alpha_0.A_s^{standard}(E)}{C.\mu^{Au}(E)} \tag{A.4}$$

where $A_m^{Au}(E)$ is taken to be eqiavalent to $\mu^{Au}(E)$, the linear photo-absorption coefficient of the gold mesh, multiplied by a constant, C. Rearranging (A.4) then yields to:

$$A_s^{standard}(E) = \frac{C}{Z_0.\alpha_0}\left(\frac{I_s^{standard}}{I_m^{standard}}\right).\mu^{Au}(E) = \frac{C}{Z_0.\alpha_0}.A_s^{'standard}(E) \tag{A.5}$$

Where $A_s^{'standard}(E)$ is the derived photo-absorption spectrum of the clean substrate.

Plugging (A.5) into (A.3);

$$\Psi(E) = \frac{Z_1.\alpha_1.N(E) + Z_1.\alpha_1.f.\dfrac{C}{Z_0.\alpha_0}.A_s^{'standard}(E)}{Z_0.\alpha_0.\dfrac{C}{Z_0.\alpha_0}.A_s^{'standard}(E)} \tag{A.6}$$

Rearranging (A.6) in order to leave $N(E)$ alone on one side of the equation yields:

$$N(E) = \left[\left(\frac{C}{Z_1.\alpha_1} \right).\Psi(E) - \left(\frac{f.C}{Z_0.\alpha_0} \right) \right].A_s^{'\,standard}(E) \tag{A.7}$$

Since $N(E)\big|_{pre-edge} = 0$, then $\Psi(E)\big|_{pre-edge} = \dfrac{Z_1.\alpha_1}{Z_0.\alpha_0}.f$ is constant, then (A.7) becomes:

$$N(E) = \left(\frac{C}{Z_1.\alpha_1} \right).\left[\Psi(E) - \Psi(E)\big|_{pre-edge} \right].A_s^{'\,standard}(E) \tag{A.8}$$

As it was expressed earlier, $N(E)$ is the NEXAFS intensity associated with the adsorbed overlayer. The last step of the normalization is to set the step height to unity by choosing an appropriate $\left(\dfrac{C}{Z_1.\alpha_1} \right)$ value.

Reference:

[1]   B, Watts, L. Thomsen, P.C. Dastoor, Journal of Electron Spectroscopy and Related Phenomena 151 (2006) 105.

APPENDIX B

The effects of a coverage dependent component of E_d on the topology of Arrhenius plots:

It is interesting to note that the Arrhenius plots for low initial coverages give desorption energies which are in good agreement with the values obtained from the curve fitting method. This makes sense since the $-C\theta$ correction to E_d from the curve fitting is minimal at the lowest initial coverages. But at significantly higher initial coverages curvature is seen in the Arrhenius plots, as per the red curve of Fig. 4.3(c). In this light, we first revisit the Arrhenius plot data when a general correction factor to E_d, $f(\theta)$, is introduced. We show that the local slopes are not simply $-E_d(\theta)/R$ alone. For the case $f(\theta) = C\theta$, we evaluate the explicit shape of a so called Arrhenius curve.

As stated previously, the Arrhenius Plots used above involved a strict treatment of the Polanyi-Wigner equation, Eq. (4.1). Only if E_d and ν are independent of coverage, can E_d be determined by using

$$\frac{\partial \left[\ln \left(I / \theta^n \right) \right]}{\partial \left(1 / T \right)} = -\frac{E_d}{R} \quad . \tag{B-1}$$

However, if E_d depends on the coverage, $E_d(\theta) = E_d^o - f(\theta)$, then the Polanyi-Wigner equation becomes

$$I(\theta,T) = -\frac{d\theta}{dT} = -\frac{1}{\beta}\frac{d\theta}{dt} = \frac{v(\theta)\theta^n}{\beta}\exp\left[-\left(E_d^o - f(\theta)\right)\Big/RT\right] \tag{B-2}$$

as shown in Eq. (4.10). Eqs. (4.4) and (4.5) from chapter 4 then yield:

$$\frac{\partial \ln\left(I\big/\theta^n\right)}{\partial\left(1\big/T\right)} = -\frac{E_d(\theta)}{R} + \left[\frac{\partial \ln v(\theta)}{\partial\theta} + \frac{1}{RT}\frac{\partial f(\theta)}{\partial\theta}\right]T^2 I - \left(\frac{\partial \ln\beta}{\partial\left(1\big/T\right)}\right) \tag{B-3}$$

There are potentially three terms that lead to non linearity in Arrhenius plots, and that lead to the errors in taking the local gradient to equal $-E_d(\theta)/R$ alone.

In the case of associative desorption from CN/Cu(001), given the quality of our fits, we have justifiably taken $n = 2$, and v to be coverage independent. I.e. the first term in square brackets in equation (B-3) above is zero. Although the temperature ramp (β) is not absolutely constant its variation is small and we can take $\left(\dfrac{\partial \ln\beta}{\partial\left(1\big/T\right)}\right) << \left(\dfrac{1}{RT}\dfrac{\partial f(\theta)}{\partial\theta}\right)T^2 I$.

When implementing also $f(\theta) = C\theta$, we deduce;

$$\frac{\partial\left[\ln\left(I\big/\theta^2\right)\right]}{\partial\left(1\big/T\right)} = -\frac{E_d^o}{R} + \frac{C\theta}{R} + \frac{CT}{R}I = -\frac{E_d(\theta)}{R} + \frac{CT}{R}I \tag{B-4}$$

A comparison of an Arrhenius plot and one calculated with simulated data is given in Fig. B.1.

One of the main features of the Arrhenius plots was that for ideal second order ($C = 0$) the plots should yield straight lines. In the case of the cyanogen data, this was not true although the plots for low coverages were much 'straighter' than those for higher coverages. However once the $-C\theta$ correctional factor is introduced, a near perfect fit results and it becomes evident that the Arrhenius plot is no longer straight. What's more, the simulated and real data show curves that are not simply curves with a decreasing gradient with increasing instantaneous coverage. The local gradient does not equal $-E_d(\theta)/R$ alone, but the final $\dfrac{CT}{R}I$ term also plays a significant role. In any TPD run the rate of desorption, I, is peaked at a specific inverse temperature, $1/T_m$. The peaking of the last term is manifest in the simulated curve, giving a point of inflection in that curve. Overall the simulated and real data curves in Fig. B.1 are in excellent agreement, hence supporting the form of equations (B-3) and (B-4).
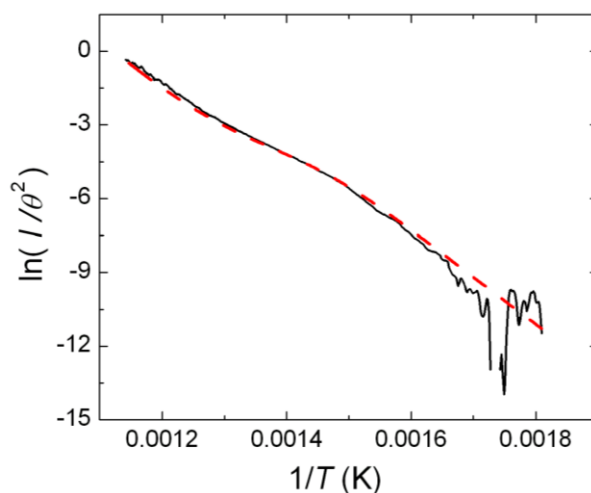

Figure B.1. Comparison of the Arrhenius plot for an experimental TPD curve taken from a C_2N_2 saturated surface (black) with a simulated (smooth red dashed) curve using the best fit $E_d^o = 175$ kJ/mol, $v = 7.0\text{x}10^{10}$ s^{-1} and $C = 14.7$ kJ/mol parameters and the functional form given in equation (B-4).

APPENDIX C

Experimental details of HNCO synthesis through decomposition of cyanuric acid, purification & storage of HNCO:
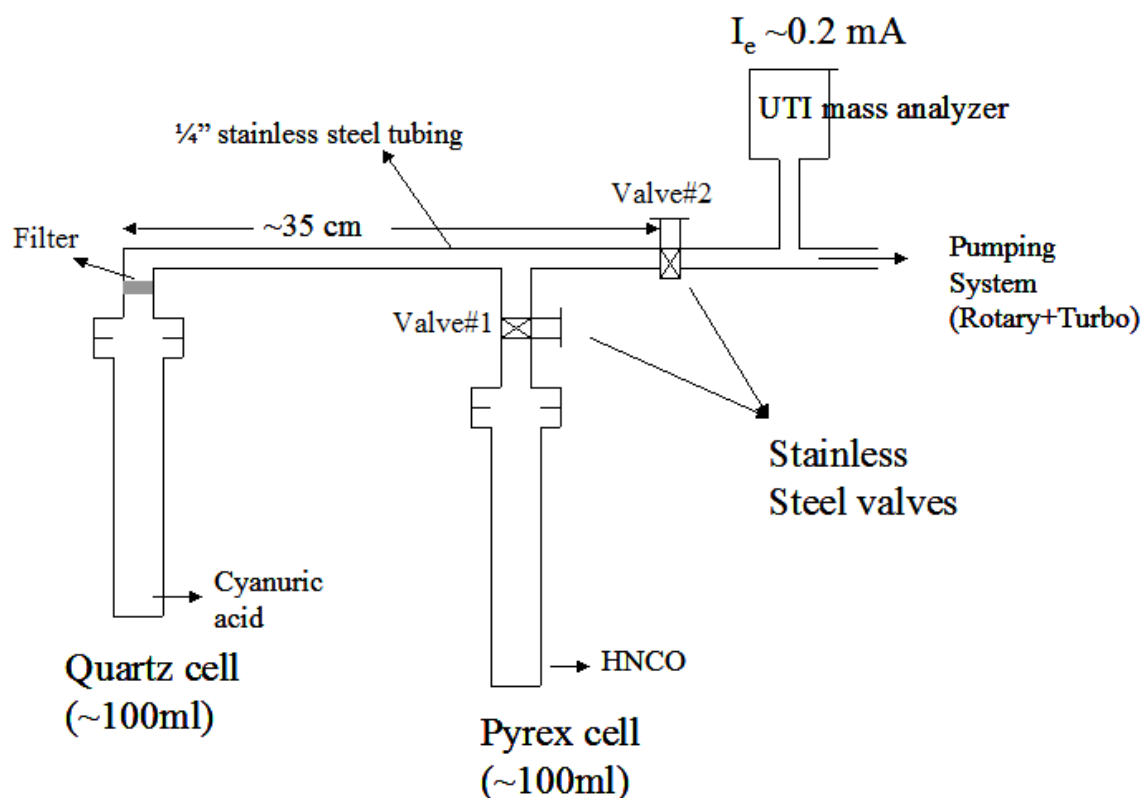
Isocyanic acid (HNCO) synthesis by the thermal decomposition of cyanuric acid has been a well known reaction since the late 1930s [1, 2]. In this appendix, a description of our custom setup built for decomposition, purification and the storage processes will be given. Some key observations and details will be listed, some of which were not reported in the literature but which we have found are necessary for the success of the processes.

This starts with placing ~0.5 g cyanuric acid ($H_3N_3C_3O_3$) into a 100 ml quartz cylinder and subsequently connecting the quartz cylinder to a pumping system. The whole system

is baked at 373K overnight while being pumped by a turbo pump. Then, the cyanuric acid in the quartz cell is heated under vacuum at 473K for ~6 hours to remove the water content. The water content in gas phase (as monitored with a UTI mass spec) decreases three orders of magnitude during this process.

Once the water is essentially removed, the Pyrex cell, where the produced HNCO will be accumulated, is immersed into liquid nitrogen. Valve#2 is closed and valve#1 is opened. The bottom of the quartz cell is heated to 800-850 ^{o}C as quickly as possible and kept at that temperature for a couple of minutes. After that, the heating is turned off and the valve#1 is shortly thereafter closed.

At the end of this process a white thin-film is observed at the top parts of the quartz cell. Presumably, the inner walls of the stainless tubes are also covered with the same film. However, no indication of any white-colored residue is observed in the Pyrex cylinder. The white-colored residue in the quartz tube appears as a result of: (i) the condensation of gas phase cyanuric acid, which is produced through sublimation of cyanuric acid starting at 330 ^{o}C and (ii) partial repolymerization of HNCO.

At this time, HNCO is also collected at the bottom of the Pyrex cell, which is immersed in a liquid nitrogen dewar. In order to have a visual proof, carefully remove the cell out of the lN$_2$ dewar while valve#1 is still closed. Blowing some cold air to the bottom of Pyrex cell helps to remove the collecting frost outside (which hinders the visual inspection). At some point solid HNCO turns to liquid as the temperature increases. One

cannot let HNCO stand out of the lN_2 dewar for too long as its polymerization half-life might be quicker than had been thought, i.e. put the Pyrex cylinder back into the lN_2 dewar as soon as you have the visual proof.

The liquid, as just observed, is a mixture which is predominantly HNCO. The major impurity is CO_2. At this stage, freeze-pump-thaw cycles are used to obtain pure HNCO. We suggest placing the Pyrex cell into a dry-ice/acetone temperature bath. Beware that bath temperature is not uniform throughout the bath volume. Push the bottom of the Pyrex cell till it touches dry ice pellets at the bottom of the batch liquid. At that level, the temperature must be approximately -70/-75 ^{o}C. When the mixture is kept at this temperature, it is safe to pump the content of the Pyrex cell by using the turbo pump directly. As a matter of fact, the mass analyzer can be used at low emission current levels (0.2 mA) during the pumping to observe the evolution of the gas phase content during pumping. If you do the latter and continuously scan the 40-50 amu region, the CO_2 peak at 44 will gradually lose intensity and later it will stop overshadowing the peak at 43 amu, which belongs to HNCO. Eventually, no more than a couple of minutes later, most of the CO_2 will be removed from the mass spectrum. After this is done and the absence of N_2 and H_2 are confirmed, place the Pyrex cell back into a lN_2 dewar for storage. The half life of HNCO polymerization into cyanuric acid in a dry ice/acetone bath is believed to be barely ½ day. A dry ice/acetone bath can be used for short periods only such as during the intended transfer of HNCO into a gas handling line for sample exposures.

The physical in-vacuum-distance between the bottom of the quartz cell, where the reactant is placed and the bottom of the Pyrex cell, where the product is collected should be neither too close nor to far away, i.e. it must be long enough for the condensation of gas phase cyanuric acid on stainless steel walls before reaching the Pyrex cell and it must be short enough to not lose too much "hot" HNCO via repolymerization before it reaches the lN2 cooled bottom of the Pyrex cell.

An extra VCR connection is needed right above the quartz cell where you can put a special VCR gasket. The hole in the gasket is filled with a porous material with 20-micrometer pores. (This gasket is a Swagelok product). That gasket is necessary to prevent blowing the cyanuric acid powder into your pumping system at the initial stages of evacuation.

It is worth reminding that the same experiment was also tried by using stainless steel cylinders instead of quartz and Pyrex ones. We failed to obtain any HNCO product when using stainless steel cells.

References

[1]   G. Herzberg and C. Reid, Discussions of the Faraday Society 9 (1950) 92.
[2]   M. Linhard, Zeitschrift fuer Anorganische und Allgemeine Chemie 236 (1938) 200.